



저작자표시-비영리-변경금지 2.0 대한민국

이용자는 아래의 조건을 따르는 경우에 한하여 자유롭게

- 이 저작물을 복제, 배포, 전송, 전시, 공연 및 방송할 수 있습니다.

다음과 같은 조건을 따라야 합니다:



저작자표시. 귀하는 원저작자를 표시하여야 합니다.



비영리. 귀하는 이 저작물을 영리 목적으로 이용할 수 없습니다.



변경금지. 귀하는 이 저작물을 개작, 변형 또는 가공할 수 없습니다.

- 귀하는, 이 저작물의 재이용이나 배포의 경우, 이 저작물에 적용된 이용허락조건을 명확하게 나타내어야 합니다.
- 저작권자로부터 별도의 허가를 받으면 이러한 조건들은 적용되지 않습니다.

저작권법에 따른 이용자의 권리는 위의 내용에 의하여 영향을 받지 않습니다.

이것은 [이용허락규약\(Legal Code\)](#)을 이해하기 쉽게 요약한 것입니다.

[Disclaimer](#)

치의과학 박사학위논문

타액선 발생과정에서 히알루론산의 역할과
조직공학에서의 생체모방적 응용

Biomimetic Approaches for Tissue Engineering
Based on the Roles of Hyaluronic Acid in
Salivary Gland Development

2021 년 2 월

서울대학교 대학원

치의과학과 신경생물학 전공

이 상 우

타액선 발생과정에서 히알루론산의
역할과 조직공학에서의
생체모방적 응용


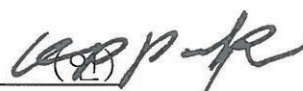


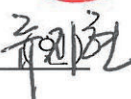
Biomimetic Approaches for Tissue
Engineering Based on the Roles of Hyaluronic
Acid in Salivary Gland Development

지도교수 박 경 표

이 논문을 치의과학박사학위논문으로 제출함
2021년 1월

서울대학교 대학원
치의과학과 신경생물학 전공
이 상 우

이상우의 박사학위논문을 인준함
2021년 1월

위원장 최 세 영 
부위원장 박 경 표 
위원 고 용 선 
위원 최 영 남 
위원 류 지 현 

Abstract

Biomimetic Approaches for Tissue Engineering Based on the Roles of Hyaluronic Acid in Salivary Gland Development

Lee, Sangwoo

Program in Neuroscience

Department of Dental Science

Seoul National University

Dry mouth, or xerostomia, caused by salivary gland dysfunction significantly impacts oral/systemic health and quality of life. Recently, there has been a growing interest in replacing severely damaged salivary glands with artificial salivary gland functional units created *in vitro* by tissue engineering approaches. Although various materials have been used as scaffolds for salivary gland tissue engineering, none of them is effective enough to closely recapitulate the branched structural complexity and heterogeneous cell population of native salivary glands. Therefore, understanding and recapitulating the roles of biomacromolecules in salivary gland organogenesis is needed to solve these problems. Hyaluronic acid (HA) is a macromolecule abundant during salivary gland organogenesis, but its role remains unknown.

In chapter I, the roles of HA during salivary gland organogenesis and artificial organ germ formation in solubilized and substrate-immobilized forms have been elucidated by using *ex-vivo* organotypic culture model of developing salivary glands. Dense HA layers encapsulating proliferative c-Kit⁺ progenitor cells expressing CD44, an HA receptor, were found. The blockage of HA synthesis, or degradation of HA, impaired eSMG growth by ablating the c-Kit⁺ progenitor cell population. It has been also found that high-molecular-weight (HMW) HA has a significant role in eSMG growth. Based on these findings, it is discovered that HA is also crucial for *in vitro* formation of salivary gland organ germs, one of the most promising candidates for salivary gland tissue regeneration. Supplementation of HMW HA in solution significantly enhanced salivary gland organ germ formation, and this effect was further increased when the HMW HA was immobilized on the substrate by polydopamine/HA co-immobilization. These results suggest that the current use of HA in salivary gland tissue engineering can be further optimized.

In chapter II, based on the findings in chapter I, I designed hyaluronic acid-catechol (HACA) conjugates to establish a versatile hyaluronic acid coating platform named “NiCHE (Nature-inspired catechol-conjugated hyaluronic acid environment)” for boosting the salivary gland tissue engineering efficacy of previously reported biomaterials. By mimicking hyaluronic acid-rich niche in mesenchyme of embryonic submandibular glands (eSMGs) with NiCHE coating on substrates including polycarbonate membrane, stiff agarose hydrogel, and polycaprolactone scaffold, cell adhesion, vascular endothelial and progenitor cell proliferation, and branching of *in vitro*-cultured eSMGs were significantly enhanced. High mechanical stiffness of substrate is known to inhibit eSMG growth, but NiCHE coating significantly reduced

such stiffness-induced negative effects, leading to successful differentiation of progenitor cells to functional acinar and myoepithelial cells. These enhancement effects of NiCHE coating were due to the increased proliferation of vascular endothelial cells via interaction between CD44 and surface-immobilized HAs. As such, NiCHE coating platform renders any kind of material highly effective for salivary gland tissue culture by mimicking *in vivo* embryonic mesenchymal HA. Based on the results, it is expected that NiCHE coating will expand the range of biomaterial candidates for salivary glands and other branching epithelial organs.

Keywords: hyaluronic acid, salivary gland, regeneration, organogenesis, polydopamine, branching morphogenesis, catechol, tissue engineering

Student Number: 2011-22467

Contents

Abstract	1
Contents	4
List of Figures	6
List of Tables	9
Abbreviations	10
General Introduction	11
1. Salivary gland dysfunction.....	11
2. Development of tissue-engineered artificial salivary glands.....	11
3. Branching morphogenesis of embryonic salivary gland.....	12
4. Limitations of salivary gland tissue engineering biomaterials.....	14
5. Hyaluronic acid in development of epithelial organs	14
Chapter I	
Developmental Roles of Hyaluronic Acid During Organogenesis of Salivary Glands and Its Application in Salivary Gland Organ Germ Formation	17
1. Introduction	18

2. Materials and Methods	22
3. Results	31
4. Discussion	65
 Chapter II	
Development of NiCHE Platform: Nature-inspired Catechol-conjugated Hyaluronic Acid Environment Platform for Salivary Gland Tissue Engineering	
72	
1. Introduction	73
2. Materials and Methods	81
3. Results and Discussion.....	89
Conclusion	115
References	120
Abstract in Korean	128

List of Figures

Chapter I

Figure 1. Spatiotemporal distribution of HA and CD44 in eSMG	33
Figure 2. Spatiotemporal expression of CD44 in eSMG and eSLG.....	35
Figure 3. Schematic illustration of distribution of HA, c-Kit ⁺ proliferative cells, and CD44 expression within an eSMG.....	36
Figure 4. Schematic diagram of <i>ex-vivo</i> organotypic culture model for eSMG and time-lapse images of <i>ex-vivo</i> -cultured eSMGs.....	39
Figure 5. Effect of 4-MU on developing eSMGs.....	40
Figure 6. Effect of HAD on developing eSMGs.....	41
Figure 7. Effect of aCD44 on developing eSMGs.....	42
Figure 8. Effect of exogenous HA of various molecular weight on developing eSMGs.....	44
Figure 9. Rescue effects of exogenous HA of various molecular weight on HA-depleted eSMGs.....	45
Figure 10. Rescue effects of exogenous HA of various molecular weight on HA-degraded eSMGs.....	46
Figure 11. Schematic diagram of embryonic organ germ formation.....	50
Figure 12. Effect of 4-MU on embryonic organ germ formation.....	51
Figure 13. Effect of HAD on embryonic organ germ formation.....	53
Figure 14. Effect of aCD44 on embryonic organ germ formation.....	54
Figure 15. Molecular weight-dependent enhancement effect of HA on embryonic organ germ formation.....	57
Figure 16. Schematic diagram of polydopamine (PD)/HA co-immobilization on the PC membrane.....	60

Figure 17. Physicochemical characterization of bare, HA, PD, and PD/HA – coated PC membrane surfaces.....	61
Figure 18. Effect of HA’s presentation forms on embryonic organ germ formation.....	62
Figure 19. Confirmation of salivary gland-specific markers in embryonic salivary gland organ germs.....	64

Chapter II

Figure 20. Schematic illustrations of salivary gland anatomy and function.....	77
Figure 21. Presence of HA in mesenchyme of developing eSMG within e14.5 mandible.....	79
Figure 22. Distribution of CD44+ vascular endothelial structure in developing eSMGs.....	80
Figure 23. Synthesis of HACA.....	92
Figure 24. Schematic illustrations of adhesive HACA coating on the various substrates.....	93
Figure 25. UV-Vis spectrum of HACA after 12 hr incubations.....	94
Figure 26. Alcian blue staining results from bare, HA, and HACA-coated materials.....	96
Figure 27. Water contact angle results from bare, HA, and HACA-coated materials.....	98
Figure 28. Thickness and surface topology of HACA-coated surfaces....	99
Figure 29. Interaction between eSMG cells and HACA-coated surfaces.....	101
Figure 30. BM of eSMGs on alginate hydrogels of different stiffness...	107

Figure 31. NiCHE coating platform enhances growth of eSMG on various substrates.....	108
Figure 32. Local enhancement of vascular endothelial (VE) cell proliferation by NiCHE coating platform.....	113
Figure 33. Schematic summary of chapter I	117
Figure 34. Schematic summary of chapter II.....	118

List of Tables

Chapter II

Table 1. Properties and biocompatibility of Biomaterials tested in this study for <i>in vitro</i> eSMG culture	95
Table 2. Atomic compositions of material surfaces	97

Abbreviations

HA	Hyaluronic acid
eSMG	Embryonic submandibular gland
BM	Branching morphogenesis
eSLG	Embryonic sublingual gland
PC	Polycarbonate
HAD	Hyaluronidase
4-MU	4-Methylumbelliferone
SGFU	Salivary gland functional unit
HABP	Hyaluronic acid binding protein
AQP5	Aquaporin 5
HACA	Hyaluronic acid-catechol conjugate
PD	Polydopamine
PCL	Polycaprolactone
VE	Vascular endothelial
EGF	Epidermal Growth Factor
FGF	Fibroblast Growth Factor
ZM	ZM323881 (VEGFR inhibitor)
Has	Hyaluronic acid synthase
aCD44	Anti-CD44 monoclonal antibody
EDC	1-ethyl-3-(3-dimethylaminopropyl)-carbodiimide hydrochloride
pERK	Phosphorylated extracellular signal-regulated kinase

General Introduction

1. Salivary gland dysfunction

Hyposalivation or Xerostomia is one of the major consequences of salivary gland dysfunction, which may cause various oral or systemic deteriorations (Guggenheimer and Moore 2003). Radiation damage on salivary glands during radiotherapy of head and neck cancer and autoimmune disease such as Sjögren's syndrome are the two major causes for salivary gland dysfunction (Jemal et al. 2009). Since saliva possesses multiple functions including anti-fungal and anti-bacterial activity, mechanical lubrication for oral mucosa and swallowing, regeneration of oral tissues, buffering activity, digestion of food, and sensation of taste, Xerostomia is concurrent with a significant decline in quality of life, prognosis of cancer patients, oral, and systemic health (Chambers et al. 2004; Humphrey and Williamson 2001). Therefore, it is highly desirable to prevent and cure salivary gland dysfunction.

2. Development of tissue-engineered artificial salivary glands

Despite many efforts, there is no satisfactory cure for Xerostomia. Use of muscarinic agonists such as Pilocarpine temporarily increase salivary flow but this approach is insufficient when the number of functional acinar cells is already too low due to the massive surgical resection or radiation damage (Burlage et al. 2009). These limitations of current therapeutic approaches can be circumvented through development of tissue-engineered artificial salivary glands or activating regenerative process of damaged salivary glands (Lombaert et al. 2017). A previous study has shown that the ParC10, an immortalized rat parotid cell line, cultured in growth

factor-reduced Matrigel self-aggregates to generate 30 to 60 μm acini-like spheroidal structures (Baker et al. 2010). These lumen-forming spheroids express tight junction proteins including zonula occludens-1, occluding, and claudin-3 at the apical sides (Baker et al. 2010). However, since these immortalized cell lines cannot be transplanted to human, *in vitro* expansion technique of human-derived primary salivary gland cells is required for clinical applications. Maimets et al. have found that EpCAM (Epithelial cell adhesion molecule)-expressing cells isolated from human salivary glands possess stem cell-like properties (Maimets et al. 2016). When they are cultured in Matrigel with epidermal growth factor (EGF), fibroblast growth factor 2 (FGF2), insulin, Y-27632, Wnt3a, and R-spondin-1, they form sphere and branched out to generate more complex glandular structure by reproducing “branching morphogenesis” (BM) observed in salivary gland development (Maimets et al. 2016).

3. Branching morphogenesis of embryonic salivary gland

Many epithelial organs such as lung, pancreas, kidney, mammary glands, and salivary glands undergo unique developmental process called branching morphogenesis (BM) (Horowitz and Simons 2008). Dynamic propagation of epithelial BM involves in multiple rounds of cleft formation, elongation, and basement membrane remodeling. BM also spatiotemporally orchestrates complex interactions among various types of cells or tissues to complete structures and functions of an organ. During the salivary gland BM, epithelial-mesenchymal cross-talks continuously occurs, and microscopically, dynamic interactions among progenitor cells, extracellular matrix components (ECM), soluble growth factors,

nerves, and vascular structures take place to regulate the entire process (Lombaert et al. 2017; Pradhan-Bhatt et al. 2013; Pringle et al. 2016). Therefore, once the detail mechanisms of BM are unveiled, it may be possible to artificially reproduce developmental BM in induced pluripotent stem cells or salivary gland stem cells for the *in vitro* generation of fully structured artificial salivary glands. Moreover, interactions and regulatory mechanisms during salivary gland development recapitulate those in regeneration process of damaged glandular organs. For examples, parasympathetic nerve innervation and vascular endothelial cell proliferation are crucial for both salivary gland development and regeneration of radiation-damaged salivary glands (Knox et al. 2013; Kwon et al. 2017). Therefore, developmental salivary gland BM has been considered as an excellent model for understanding the regeneration mechanisms and screening regenerative biomaterials for salivary glands (Patel and Hoffman 2014).

To do so, researchers have used *ex-vivo* organotypic culture model of developing mouse embryonic submandibular glands (eSMG). Although air-media interface culture system using Polycarbonate (PC), a non-biodegradable material, has been considered as a golden standard for *ex-vivo* organotypic culture of eSMGs, *ex-vivo* cultured eSMGs show retarded branching compared to *in vivo* eSMGs at the same embryonic day. Since enhancing *ex-vivo* BM up to *in vivo* level is crucial for the efficient generation of artificial salivary glands, extensive studies on positive regulators of BM such as growth factors (eg. FGF7, FGF10, and EGF) and ECMs (eg. fibronectin, heparin sulfate, collagen, and laminin) have been conducted.

4. Limitations of salivary gland tissue engineering biomaterials

However, since the aforementioned enhancement factors for BM are usually very expensive and easily degradable, simply supplementing such factors to the culture system is neither practical nor efficient for salivary gland tissue engineering from industrial perspectives. To overcome these limitations, numerous approaches to efficiently mimic developmental microenvironment have been studied. Artificially produced materials such as decellularized amniotic membrane (Hsiao et al. 2011), chitosan membrane (Yang et al. 2012b; Yang and Young 2009), RGD-coated alginate hydrogel (Taketa et al. 2015), and electro-spun nano-sized PLGA fibers (Sequeira et al. 2012) have been used to enhance BM of developing eSMGs. However, *ex-vivo* BM of eSMGs is largely depending on the physicochemical and topologic properties of such materials, and each previously developed biomaterial has its own positive and negative factors for *ex-vivo* BM of eSMG. Therefore, I speculated that it is necessary to develop a versatile platform that can enhance advantageous properties of any conventional biomaterials while reducing or compensating their negative properties for salivary gland BM.

5. Hyaluronic acid in development of epithelial organs

Hyaluronic acid (HA), a fourth class of glycosaminoglycan, is one of the most abundant endogenous ECM in our body. Biologically, HA is a ligand for various receptors such as CD44, RHAMM, and ICAM-1, and it has been known that HAs in different molecular weight exert different biological effects (Fraser et al. 1997). Biological functions of HA are further diversified since HA can associate with other protein ligands. For examples, high molecular HA is known as inhibitor for

angiogenesis but when it was co-treated with SDF-1 they enhanced angiogenesis (Fuchs et al. 2013). Biological effects of HA also can be changed by its physical state; immobilized form of HA and solubilized form of HA exert different biological effects (Sapudom et al. 2017). Since HA has many physical and biological functions, they ubiquitously exist as milieu for various kinds of cells to maintain their own functions and characteristics (Fraser et al. 1997). For examples, large portion of extracellular matrix in bone marrow is composed of HA, and its presence is critical for regulating hematopoietic stem cells' pluripotency and proliferation (Avigdor et al. 2004). Likewise, HA regulates pluripotency and differentiation of various stem cell populations during developmental morphogenesis of organs (Toole 2001). HA provides milieu for the migration and proliferation of epithelial, endothelial, and smooth muscle cells during the process of prostate (Gakunga et al. 1997) and kidney (Pohl et al. 2000) development. In salivary glands, roles and distribution of glycosaminoglycans within a developing salivary gland itself have been well-characterized (Patel et al. 2006). However, HA-specific roles and distribution of HA during salivary gland organogenesis has not been studied yet.

The aim of this thesis is to elucidate developmental roles of HA during organogenesis of eSMGs and apply such findings on salivary gland tissue engineering and regeneration. To achieve these goals, the followings are addressed in the two subsequent chapters.

- To identify localization and quantity of HA in developing eSMGs.
- To identify biological effects of HA of different molecular weights and presentation forms on developing eSMGs and dissociated eSMGs.

- To develop and establish efficient methods to immobilize HA on various biomaterial surfaces.
- To elucidate biological mechanisms of eSMG BM enhancement by surface-immobilized HA.

CHAPTER I

Developmental Roles of Hyaluronic Acid During Organogenesis of Salivary Glands and Its Application in Salivary Gland Organ Germ Formation

This chapter is a slightly modified version of “**Developmental role of hyaluronic acid and its application in salivary gland tissue engineering**” published in *Acta Biomaterialia* and has been reproduced here with the permission of the copyright holder and co-authors.

Introduction

Saliva, one of the most important bodily fluids, is produced by the salivary glands. It provides anti-fungal and anti-bacterial activity, lubricates the oral cavity, digests food, and transports taste molecules to the taste buds (Mandel 1989). Therefore, salivary gland dysfunction leads to hyposalivation or xerostomia, which causes the deterioration of both oral and systemic health (Humphrey and Williamson 2001). The major causes of hyposalivation or xerostomia are senescence of salivary glands (Ghezzi and Ship 2003), drug complications (Guggenheimer and Moore 2003), radiation damage to salivary glands from head and neck cancer therapy (Chambers et al. 2007; Dirix et al. 2006), loss of salivary glands after cancer resection surgery (Jacob et al. 1996), and autoimmune diseases (e.g., Sjögren's syndrome) (Nederfors 2000; Talal 1987). To enhance salivation and treat hyposalivation, muscarinic agonists (e.g., pilocarpine) are used to stimulate saliva-producing acinar cells. However, these are ineffective due to the insufficient number of functional acinar cells left after damage to the salivary glands (Gornitsky et al. 2004). Another problem of pilocarpine is its off-target side-effects including excessive sweating, rhinitis, tearing, nausea, and stomach cramps, which makes patients difficult to continue the medication (Gornitsky et al. 2004). Therefore, it is highly desirable to develop therapeutics to regenerate or replace damaged salivary gland tissues.

Since salivary glands contain complex glandular structures with multiple cell types, including acinar, ductal, vascular endothelial, nerve, and myoepithelial cells, they are difficult to develop *in vitro*. However, all these complexities and heterogeneity

of salivary gland naturally arise during *in vivo* organogenesis via process called branching morphogenesis (Harunaga et al. 2011; Lu and Werb 2008). Therefore, mimicking developmental processes and/or developmental niches has been considered as one of the most feasible strategies for the *in vitro* generation of artificial salivary gland (Harunaga et al. 2011). During fetal development, most organs originate from a heterogeneous tissue structure called the “embryonic organ germ”, which is enriched with epithelial stem/progenitor cells (Nakao et al. 2007; Ogawa et al. 2013). Among them are the c-Kit⁺ cells, one of the most potent stem/progenitor cell populations in salivary gland organogenesis (Lombaert et al. 2013; Nelson et al. 2013). c-Kit⁺ cells, making up 10 to 20% of total cells in an intact embryonic submandibular glands (eSMGs), are mainly located at the epithelial end buds to differentiate into proacinar cells at the late stage of branching morphogenesis (Lombaert et al. 2013). Generally, c-Kit⁺ cells in eSMGs are highly mitotic, thus contributing to the aggressive expansion of epithelial buds. Therefore, understanding the reciprocal interactions between surrounding mesenchymal niche and epithelial c-Kit⁺ stem/progenitor cells is highly desirable when artificial salivary glands are generated from embryonic or induced-pluripotent stem cells. In fact, numerous proof-of-concept studies on the orthotopic transplantation of bioengineered organ germs generated from embryonic teeth, hair follicles, and salivary glands have shown promising results (Ikeda et al. 2009; Nakao et al. 2007; Ogawa et al. 2013; Toyoshima et al. 2012). In addition, it has been reported that dissociation of intact embryonic salivary glands into single cells leads to their self-organization and the formation of new organ germs that continue organogenesis (Okumura et al. 2012; Wei et al. 2007). However, it is still necessary to optimize the *in vitro* organ germ

generation process by maximizing the stem/progenitor cell repopulation and minimizing the cell seeding density and manipulation steps. I hypothesized that a method for efficient repopulation of c-Kit⁺ progenitor cells *in vitro* could be found by comparing the spatiotemporal dynamics of surrounding niche and c-Kit⁺ stem/progenitor cell population.

I found that spatiotemporal expression patterns of hyaluronic acid synthase-2 and 3 (Has-2, -3) gene (Musselmann et al. 2011) is similar to that of Kit gene; both genes were highly expressed at the periphery of epithelial end buds, and the expression levels of both genes were simultaneously increased up to embryonic day 14~15 and then gradually decreased to postnatal 1 (Musselmann et al. 2011). Has-2 mainly produces high-molecular-weight (HMW) hyaluronic acid (HA) above 2,000 kDa while Has-3 produces low-molecular-weight (LMW) HA ranging from 100 to 200 kDa (Itano et al. 1999). Historically, HA has been the favored extracellular matrix component for salivary gland tissue engineering (Ozdemir et al. 2016b; Pradhan-Bhatt et al. 2013; Pradhan et al. 2010; Srinivasan et al. 2017). However, although it has been reported that the primary human salivary gland stem/progenitor cells can be repopulated and differentiated into acinar cells in HA hydrogel and HA derivatives (e.g., thiolated HA/acrylate HA hydrogel (Ozdemir et al. 2016b), thiolated HA/polyethylene glycol hydrogel (Pradhan-Bhatt et al. 2013), and HA/bioactive peptide hydrogel (Pradhan et al. 2010)), the application of HA-derived biomaterials on embryonic salivary gland cell has not been reported yet. In this study, I revealed the role of HA in embryonic c-Kit⁺ stem/progenitor cell self-organization, proliferation, and eSMG branching morphogenesis. After that, I first confirmed the biological effects of HA with differing molecular weights (MW; 5 to 1,000 kDa) on

c-Kit⁺ progenitor cells during organogenesis and self-organization in an eSMG organotypic culture model. In addition, it was unexpectedly found that the biological activity of HA was enhanced when it was immobilized on a material surface via catecholamine chemistry (Kang et al. 2012). Based on these findings, it is expected that HA-based biomaterials can be widely applied for salivary gland tissue engineering and regenerative medicine.

Materials and Methods

Materials

HAs with molecular weight of 5, 200, and 1,000 kDa were purchased from Lifecore (USA). Dopamine hydrochloride, collagenase IV, 4-Methylumbelliferone ($\geq 98\%$), hyaluronidase from *Streptomyces hyalurolyticus*, Alcian Blue solution, transferrin, L-ascorbic acid, and Whatman® Nuclepore™ track-etched membranes were purchased from Sigma-Aldrich (USA). Dulbecco's Modified Eagle Medium with F12 supplement (DMEM/F12 1:1) and Penicillin/Streptomycin were purchased from Gibco (USA).

In vitro eSMG culture

eSMGs were isolated from embryonic day 13.5 mouse fetus as previously described methods (Borghese 1950). Isolated eSMGs were placed on the bright side of porous polycarbonate (PC) filter membrane (Watman, 110405) floating on the DMEM/F12 1:1 (Gibco, Grand Island, NY) supplemented with 150 $\mu\text{g}/\text{mL}$ ascorbic acid (Sigma-Aldrich, A5960), 50 $\mu\text{g}/\text{mL}$ transferrin (Sigma-Aldrich, T8158), and 1% v/v penicillin-streptomycin (Gibco, 15140122). The eSMGs were cultured in an incubator for 48 hr (37 °C, 5% CO₂, controlled humidity). The animal experiment protocol used in this study has been approved by Seoul National University Institutional Animal Care and Use Committee (approval number: SNU-160322-2). For CD44 blocking experiment, anti-CD44 monoclonal antibody (BioXCell, BE0039) was used.

Mesenchyme/Epithelium separation

Mesenchyme/epithelium separation procedures were referred to previous methods (Larsen et al. 2006; Rebutini and Hoffman 2009). Briefly, 10~15 e13 eSMGs were incubated with 0.5 U/mL dispase I (Life Technologies, 17105-041) dissolved in calcium/magnesium-free Hank's Balanced Salt solution for 20 min, and washed twice with 3% bovine serum albumin (Sigma-Aldrich, A2934-25G) dissolved in DMEM/F12 1:1 (Gibco, 14175-095). Mesenchyme and epithelium of eSMGs were then separated by ultrafine forceps (Dumont #5 forceps dumostar alloy 0.05 mm x 0.01 mm, Fine Science Tools, 11295-20) under stereomicroscope.

eSMG dissociation and organ germ formation

Eighty to one hundred eSMGs were isolated from e13.5~14.5 mouse fetus and immersed in RPMI media containing 1 mg/mL collagenase 4 (Sigma-Aldrich, C5138-100MG). eSMGs were incubated at 37 °C for 20 mins in a continuously rotating tube held by MACSmix Tube Rotator (Miltenyi Biotec, 130-090-753). Enzymatically digested eSMGs were then mechanically dissociated by gentleMACS Dissociator (Miltenyi Biotec, 130-093-235) with pre-programmed "hTumor 3" mode. Dissociated eSMG cells were washed three times with DMEM/F12 1:1 (Gibco, Grand Island, NY). After the cell counting, 5 µL of dissociated eSMG cells (10,000 cells) were placed on the floating PC membrane. The dissociated eSMG cells were cultured in an incubator for 48 hr (37 °C, 5% CO₂, controlled humidity). For CD44 blocking experiment, anti-CD44 monoclonal antibody (BioXCell, BE0039) was used.

Immunohistochemistry

Developing mandibles of mouse fetus at embryonic day 13.5 and submandibular glands of adult mouse were harvested and immediately fixed with 4% formaldehyde-PBS for three days at 4 °C. For HABP staining, fixed mouse fetus mandible and SMGs in paraffin block sections were deparaffinized and rehydrated. For antigen retrieval step, the sections were immersed into Tris-EDTA buffer with pH 9.0 for 20 min at 100 °C. To inactivate endogenous peroxidase, sections were immersed in 3% hydrogen peroxide for 6 min. The sections were blocked with 5% (v/v) normal horse serum (ThermoFisher Scientific, 31874) for 30 min. After that, sections were incubated with biotinylated HABP (1:1000, Amsbio, AMS.HKD-BC41) for 30 min at room temperature. HABP specifically binds to versican G1 domain of HA. Sections were then reacted with DAB substrate kit (Vector) for 2 min and counterstained with Mayer's hematoxylin solution for 1 min. The sections were dehydrated and cleared by ethanol and xylene, respectively. Finally, the sections were mounted on slides with Permount mounting medium (Fisher chemical, SP15-100). The slides were imaged via Lionheart FX equipped with 4X and 10X magnification lens (BioTek Instruments).

Quantitative analysis of mesenchymal and epithelial hyaluronic acid

After the mesenchyme/epithelium separation of e13 eSMGs, each mesenchymal /epithelial part was immersed in distilled water-containing bead-homogenizer tube (weighted at the beginning) and thoroughly homogenized by Superfast Prep-2 (MP Biomedical). The homogenized sample was immediately frozen at -80 °C. Frozen sample was then freeze-dried overnight (Labconco, Freezone12). After that, tubes

were weighted again so that the weight of epithelium and mesenchyme was measured correctly. Dried epithelial/mesenchymal tissues were then immersed in 1 mL PBS for quantification of HA amount. Amount of HA was quantified by using Hyaluronic Acid ELISA Kit (Bio Vision, E4626-100) according to the manufacturer's protocol.

Immunofluorescence staining

Cultured eSMGs or organ germs were fixed with 4% paraformaldehyde for 18 min at room temperature. Fixed eSMGs or organ germs were washed twice with PBS and permeabilized with PBS containing 0.5% v/v Triton-X100 (PBSX) for another 20 min at room temperature. Permeabilized eSMGs or organ germs were then immersed in PBSX containing 10% Normal Donkey Serum (NDS, Sigma-Aldrich) and 1% mouse on mouse blocking reagent (M.O.M® Blocking Reagent, Vector Laboratories, MKB-2213) for three hours at room temperature. After the blocking step, eSMGs or organ germs were incubated with PBSX containing primary antibodies (1:100) and 3% NDS for 12 hr at 4 °C. The primary antibodies used in the procedure are as follows: rabbit polyclonal anti-Ki67 antibody (ThermoFisher Scientific, 14-5698-82), goat polyclonal anti-c-kit antibody (R&D System, AF1356), rat monoclonal anti-CD44 antibody (Abcam, ab157107), rabbit polyclonal anti-Aquaporin 5 antibody (Alomone, AQP-005), mouse monoclonal anti-Cytokeratin 14 (CK14) antibody (Abcam, ab7800), mouse monoclonal anti-Cytokeratin 18 (CK18) antibody (Abcam, ab668), rabbit polyclonal anti-Cytokeratin 5 (CK5) antibody (Abcam, ab52635). The unbound primary antibodies were washed by PBSX for four times (10 min per wash) at room temperature. After the washing, eSMGs or organ germs

were incubated with PBSX+3%NDS solution containing secondary antibodies (1:250) and DAPI (1:1000) at 4 °C for 12 hr. The secondary antibodies used in this step are as follows: Donkey anti-goat IgG (H + L) Alexa Fluor® 488 conjugate (Abcam, ab150129), Donkey anti-rabbit IgG (H + L) Alexa Fluor® 488 conjugate (Abcam, ab150073), Donkey anti-rabbit IgG (H + L) Alexa Fluor® 594 conjugate (Abcam, ab150080), and Donkey anti-rat IgG (H + L) Alexa Fluor® 647 conjugate (Abcam, ab150167). The unbound secondary antibodies were washed by PBSX for four times (10 min per wash). Finally, eSMGs or organ germ attached on the filter paper were mounted on slide for Confocal Laser Scanning Microscope (CLSM) imaging.

Immunofluorescence staining of epithelial rudiments

After the mesenchyme/epithelium separation of e13 eSMGs, epithelial rudiments were immediately immersed in 20 µL of cold growth factor-reduced Matrigel (BD Bioscience, 356231) dropped on a cell culture slide dish (SPL, 30104). The Matrigel drops were then solidified at 37 °C for 20 min. After that, epithelial rudiment-containing Matrigel drops were fixed with cold 4% paraformaldehyde for 20 min and washed four times with PBS. Fixed epithelial rudiments were permeabilized and blocked with PBSX containing 10% NDS for three hours at room temperature. The permeabilized/blocked epithelial rudiments were overnight incubated with goat polyclonal anti-c-Kit antibody (1:100, R&D System, AF1356), rat monoclonal anti-CD44 antibody (1:100, Abcam, ab157107), and biotinylated HABP (1:200, Amsbio, AMS.HKD-BC41) diluted in PBS containing 3% NDS and 0.5% Tween-20 (PBST) at 4°C. After the primary antibody incubation, epithelial rudiments were washed

three times with PBST. The epithelial rudiments were then incubated with PBST+3%NDS solution containing secondary antibodies (1:250) and DAPI (1:1000) at 4 °C for 12 hr. The secondary antibodies used in this step are as follows: Donkey anti-goat IgG (H + L) Alexa Fluor® 488 conjugate (Abcam, ab150129), Donkey anti-rat IgG (H + L) Alexa Fluor® 647 conjugate (Abcam, ab150167), Streptavidin-Alexa Fluor® conjugate (ThermoFisher Scientific, S11227). The unbound secondary antibodies were washed by PBST for three times and PBS for three time (10 min per wash). Finally, the walls on the cell culture side dish was removed and epithelial rudiments were mounted for Confocal Laser Scanning Microscope (CLSM) imaging.

eSMG or organ germ imaging

All bright field images were obtained by Nikon digital inverted fluorescence microscope (Nikon, Ti). Immunofluorescence staining images were obtained by CLSM (Carl Zeiss, LSM700) equipped with 10X, 20X, and 40X Plan-Apochromat lens (Carl Zeiss). For multi-color imaging, 405, 488, 555, and 647 nm excitation lasers were used. For each image, 3~4 Z-sections were obtained and merged to one image via Maximum intensity projection tool in Zen 2010 Blue software (Carl Zeiss).

Quantitative Reverse Transcription-Polymerase Chain Reaction (qRT-PCR)

Approximately 10 eSMGs were collected per group and immersed in TRIzol reagent (ThermoFisher Scientific, 15596018) to get homogenized by using Superfast Prep-2 (MP Biomedical). Total RNA was isolated by using Direct-Zol RNA

MicroPrep kit (ZYMO RESEARCH, R2060) according to the manufacturer's instruction. The purity and concentration of the total RNA were measured using a NanoDrop 1000 (ThermoFisher Scientific). cDNA was synthesized from 1 µg of total RNA with reverse transcriptase. Primer sequences for CD44 and GAPDH were as follows: For mouse CD44, forward 5'-TGAAACATGCAGGTATGGGT-3' and reverse 5'-GCTGAGGCATTGAAGCAATA-3'. For mouse GAPDH, forward 5'-GAAGGTGAAGGTCGGAGTC-3' and reverse 5'-GAAGATGGTGTGGGATTTTC-3'. qRT-PCR was conducted with following conditions: 35 cycles of denaturation at 94 °C for 40 sec, annealing at 55 °C for 40 sec, and extension at 72 °C for 40 sec, with a final extension at 72 °C for 10 min. cDNA from samples were amplified using PCR amplification machine (Bio-Rad Laboratories Inc, PTC-1148C).

Co-immobilization of polydopamine/HA (PD/HA) on PC filter membranes

The PD/HA-coated PC filter membranes were prepared according to the previous research with slight modifications (Kang et al. 2012). Briefly, the dopamine (2 mg/mL) and HA (2 mg/mL) were dissolved in Tris-HCl buffer at pH 8.5. The PC filter membranes were immersed in mixture solution of HA and dopamine for 24 hr at 37 °C. After the incubation, the PC filter membranes were gently washed with PBS for three times and dried in drying oven at 37 °C. The filter membranes were sterilized under UV light for 30 min for further use. The HA-immersed PC membranes without dopamine were used as a control.

Characterization of PD/HA-immobilized PC filter membrane

For alcian blue staining, PD/HA-coated PC filter membranes were immersed in premade alcian blue solution (Sigma-Aldrich, B8438) for 10 min and gently washed with PBS three times. The alcian blue-treated PD/HA-coated PC filter papers were dried and imaged via a stereomicroscope (Leica, S6D). Scanning electron microscopy (SEM) images of PD/HA-coated PC filter membrane were obtained by Phenom ProX (ThermoFisher Scientific) at 15 kV acceleration voltage. The HA-immersed PC membranes without dopamine were used as a control.

Data collection and statistical analysis

Number of epithelial buds was manually counted on the bright field images. The word “organ germ” is defined as an epithelial/mesenchymal heterogenous cell cluster that can be observed in bright field images.

c-Kit⁺ or AQP5⁺ area per bud was measured by Colocalization module in Zen 2010 Desk 3.0 (Carl Zeiss). Briefly, an epithelial bud was manually selected as a region of interest (ROI) based on DAPI image. After that, Colocalization module was activated, and intensity threshold value of each channel (DAPI and c-Kit/AQP5) was subjectively but accurately defined to exclude artifacts and non-specific staining. All intensity threshold values were set to equal in one set of experiment (eSMG samples or groups sharing same harvesting, fixation, staining, and imaging time points). Proportion of c-Kit/AQP5⁺ area out of DAPI⁺ area above the intensity thresholds were automatically calculated by the Colocalization module in Zen 2010 Desk 3.0 (Carl Zeiss).

Sizes of organ germ were measured by Image J. Relative intensity heat map was produced by Image J plug-in named “Interactive 3D Surface Plot” downloaded from “<https://imagej.nih.gov/ij/plugins/surface-plot-3d.html>”. Water contact angle was measured by Image J. Statistical analysis and statistical significance were calculated by One-way ANOVA with Tukey’s multiple comparison tests in Prism 8.1.0 software (GraphPad Software, Inc.). Significance is set to *: $p < 0.05$, **: $p < 0.01$, ***: $p < 0.005$, ****: $p < 0.001$.

Results

Distribution of hyaluronic acid (HA) and its receptor, CD44, in developing eSMG

To verify the role of HA during eSMG branching morphogenesis, I first confirmed the distribution of HA in the surrounding branching eSMGs. eSMGs are bilaterally located at the anterior mandible of the mouse fetus (**Figure 1a**, left) and contain mesenchymal compartments including mesenchymal cells, vascular endothelial cells, and parasympathetic ganglion cells. eSMGs also contain epithelial compartments, including c-Kit⁺ progenitor cells (**Figure 1a**, right). First, HA distribution was visualized by immunohistochemically staining hyaluronic-acid-binding protein (HABP) on developing mandibles at embryonic day 13.5 (e13) and 8-week old male adult mouse. HA was primarily localized at the mesenchymal area of developing eSMGs and embryonic sublingual glands (eSLGs). Quantitative analysis of HA contents in e13.5 eSMG mesenchyme and epithelium by dispase digestion revealed that mesenchyme contained 9.7 times more HA than epithelium (3.766 ug HA/g mesenchyme and 0.387 μ g HA/g epithelium). Interestingly, a significantly higher HA density was observed in e13.5 embryonic salivary glands than adult salivary glands, indicating that HA is spatiotemporally regulated during salivary gland organogenesis (**Figure 1b**).

Alcian blue staining, which selectively stains uronic acids (Scott and Dorling 1965; Scott et al. 1964), indicated a significant increase of the HA density at the border between the mesenchyme and epithelial bud ends (**Figure 1c**). Fluorescence staining

for Ki-67+ (a mitosis marker) and c-Kit, a progenitor marker of salivary glands, indicated that peripheral areas (or bud-ends) of actively branching buds were abundant with highly mitotic cells that robustly expressed c-Kit, while the inner area of buds showed decreased expression of c-Kit and mitotic activity (**Figure 1d**). Based on these results, I hypothesized that the presence of progenitor cells at the periphery of buds and the presence of dense HA stratum at the mesenchymal area close to the bud ends are functionally linked with a ligand-receptor relationship. As expected, an HA receptor, CD44 was expressed at the mesenchyme and periphery of both eSMG and eSLG bud ends from e13 to e15 (**Figure 1e, Figure 2a and 2b**). In summary, HA is mainly localized at the mesenchyme, and its density increases with proximity to the epithelial bud ends, which are composed of highly mitotic c-Kit+/CD44+ epithelial progenitor cells (**Figure 3**).

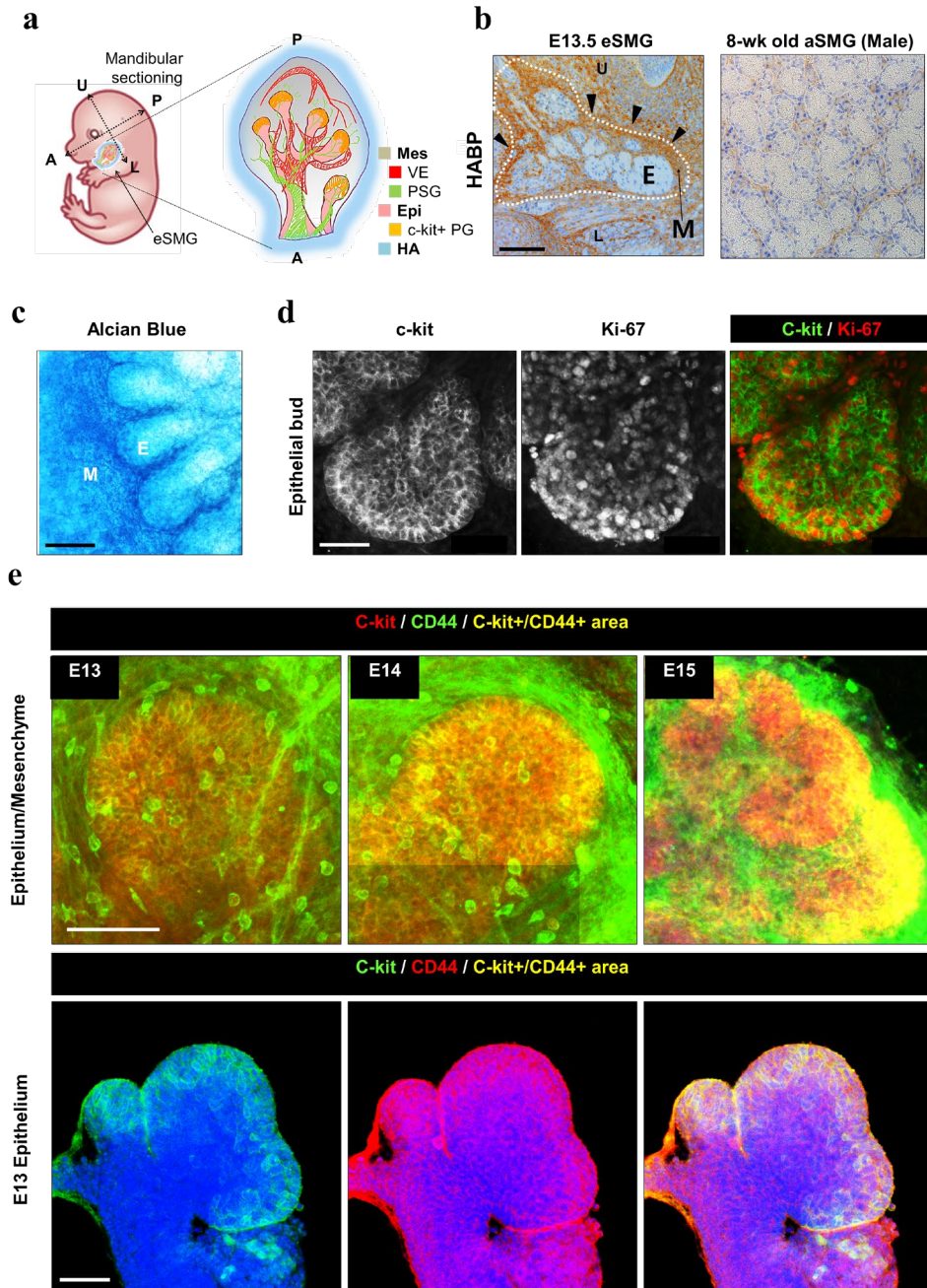


Figure 1. Spatiotemporal distribution of HA and CD44 in eSMG

(a) Schematic illustration of anatomic location and structure of eSMG. U: upper side, L: lower side, A: anterior, P: posterior, Mes: Mesenchyme, VE: Vascular endothelia, PSG: Parasympathetic ganglion, Epi: Epithelium, PG: Progenitor cell, HA:

Hyaluronic acid. **(b)** Distribution and amount of HA within developing e13.5 eSMG (left) and adult SMG from 8-week old male mouse (right) are depicted by Hyaluronic acid binding protein (HABP) staining (brown). White dotted line marks eSMG. M: mesenchyme, E: epithelium. (Scale bar = 100 μm). **(c)** Alcian blue staining image of eSMG's end-bud area (Scale bar = 150 μm). **(d)** Expression of c-Kit (green) and identification of mitotic cells (Ki-67⁺ cells, red) within a single end bud of e14 eSMG (scale bar = 50 μm). **(e)** Spatiotemporal expression patterns of CD44 (green) and c-Kit (red) within an intact eSMG. Co-localized regions are in yellow color (Upper panel, scale bar = 50 μm). Epithelial expression of c-Kit (green) and CD44 (red) in e13 eSMG without mesenchyme (lower panel, scale bar = 50 μm).

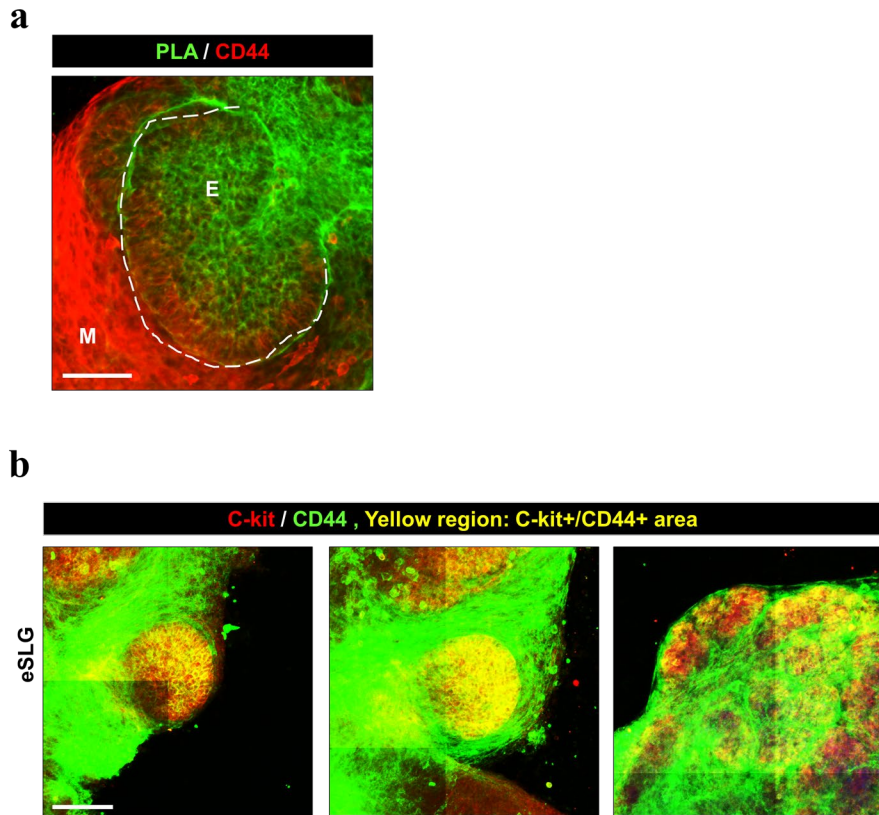


Figure 2. Spatiotemporal expression of CD44 in eSMG and eSLGs.

a) Immunofluorescence staining of epithelial bud (stained with peanut lectin agglutinin; PLA, green) and CD44 (red) in e13.5 eSMGs. Scale bar = 50 μ m. **b)** Immunofluorescence staining of epithelial c-Kit⁺ and CD44 in eSLGs.

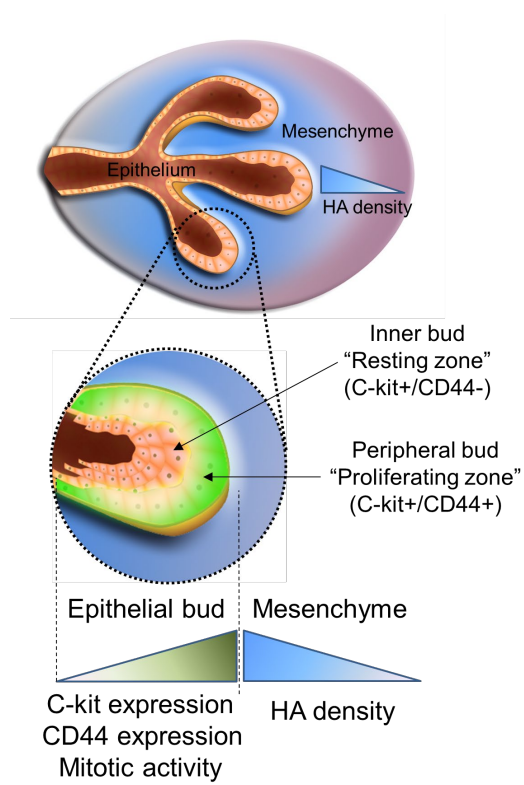


Figure 3. Schematic illustration of distribution of HA, c-Kit⁺ proliferative cells, and CD44 expression within an eSMG.

Role of HA during branching morphogenesis of developing eSMG

To further scrutinize the role of HA in salivary gland organogenesis and maintenance of the progenitor cell population, I used *ex-vivo* eSMG culturing. Briefly, eSMGs were laid on solution-permeable porous filter paper that was floating on serum-free medium (**Figure 4a**). At this air-medium interface, e13 eSMG underwent extensive branching morphogenesis up to 120 hr, the equivalent of P1 SMG (**Figure 4b**). As branching morphogenesis progressed, the mesenchyme/epithelium ratio decreased, while the progenitor cell population increased up to 48 hr and then gradually decreased after differentiation into acinar cells (**Figure 4b**) (Lombaert et al. 2013). Based on these results, the experiments were conducted between e13 (0 hr) and e15 (48 hr).

To study the importance of HA in eSMG branching morphogenesis and the c-Kit⁺ stem/progenitor cell population, loss-of-function experiments were conducted. Due to the embryonic lethality of hyaluronic acid synthase-2 gene (*has-2*) knock-out mice (Camenisch et al. 2000; Spicer et al. 2002; Toole et al. 2005), endogenous HA production was pharmacologically perturbed with 4-Methylumbelliferone (4-MU) treatment, which inhibits hyaluronic acid synthase-2/3 and depletes UDP-glucuronic acid (Kakizaki et al. 2004; Kultti et al. 2009). Indeed, treatment of 0.1 and 1.0 mM 4-MU significantly reduced total amount of HA in eSMGs (**Figure 5a** and **5b**). In a concentration-dependent manner, the degree of branching morphogenesis and c-Kit⁺ stem/progenitor cell population were significantly reduced by 4-MU treatment (**Figure 5c**, **5d**, and **5e**). At 1.0 mM 4-MU, branching morphogenesis was completely abolished (bud fold change < 1), and no viable c-Kit⁺ stem/progenitor cells were

observed (**Figure 5c, 5d, and 5e**). This result suggests that HA is required to maintain the c-Kit⁺ stem/progenitor cell population and branching morphogenesis of eSMG.

To confirm whether the structural integrity of HA (polymeric HA or degraded disaccharide HA) could affect branching morphogenesis and the c-Kit⁺ stem/progenitor cell population in eSMG. Hyaluronidase (HAD) extracted from *Streptomyces hyalurolyticus* was used to enzymatically degrade HA into disaccharide fractions without degrading the chondroitin sulfate groups (Ohya and Kaneko 1970). HAD-treated eSMGs showed significantly inhibited branching morphogenesis and a decreased c-Kit⁺ stem/progenitor cell population, though not as much as eSMGs treated with 4-MU (**Figure 6a – 6d**). In addition, HAD-treated eSMG had significantly enlarged buds (average bud size = 26,842 μm^2) compared to the control group (average bud size = 6,492 μm^2), indicating that the epithelial buds had not been gone through proper clefting process for further branching (**Figure 6a and 6e**). These results indicate that the presence of intact HA is crucial for maintaining the c-Kit⁺ stem/progenitor cell population and proper branching morphogenesis of eSMG.

Finally, role of CD44 receptors in intact eSMGs was examined by blocking them with anti-CD44 monoclonal antibodies (aCD44). e13.5 eSMGs were incubated with 100 $\mu\text{g}/\text{mL}$ aCD44 for 48 hrs. It is note that aCD44 can only block the mesenchymal CD44s since eSMG epithelium is encapsulated by mesenchyme. Blocking of mesenchymal CD44s did not exert any significant change in bud number or c-Kit expression (**Figure7a and 7b**).

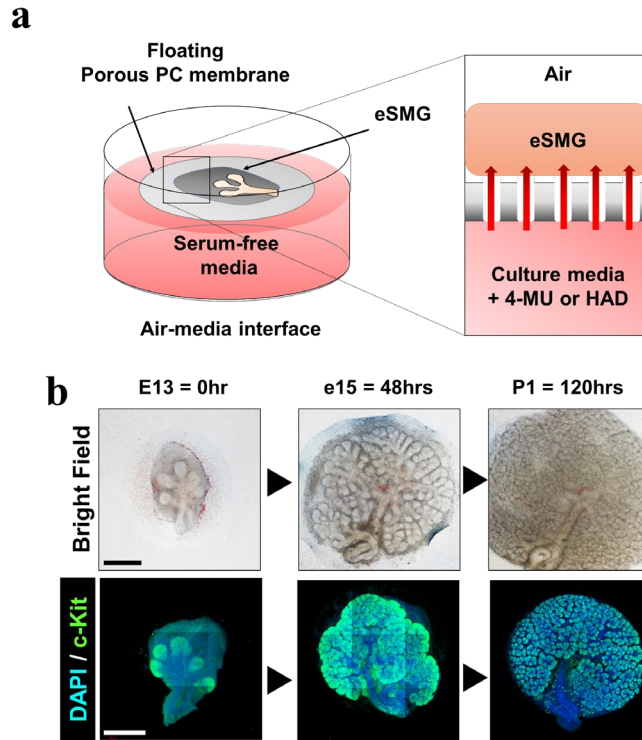


Figure 4. Schematic diagram of *ex-vivo* organotypic culture model for eSMG and time-lapse images of *ex-vivo*-cultured eSMGs

(a) Schematic illustration of *ex-vivo* eSMG culture. **(b)** Time-dependent live imaging of developing eSMG (from e13 to postnatal 1 or P1) under branching morphogenesis (upper panel, black and white scale bar = 500 μm). Time dependent epithelial c-Kit expression in eSMG (Lower panel).

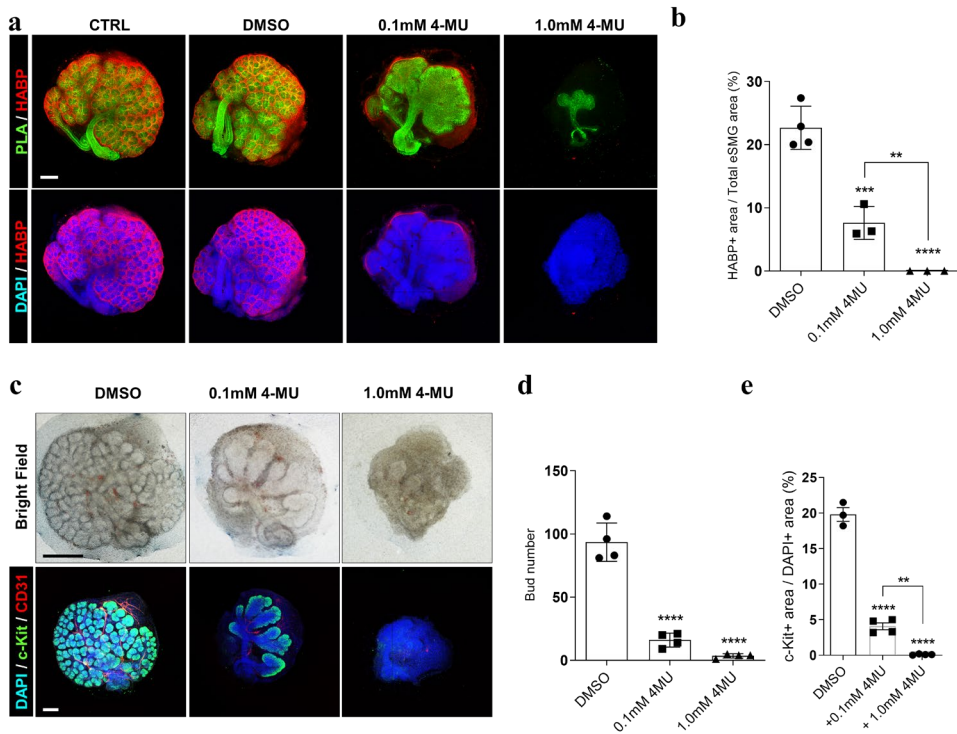


Figure 5. Effect of 4-MU on developing eSMGs

(a) HA molecules in eSMGs were visualized by HABP (red) 48 hr after the treatment of DMSO, 0.1 mM 4-MU, or 1.0 mM 4-MU. Epithelium is stained with PLA (green) and nucleus is stained with DAPI (blue). Scale bar = 200 μ m. (b) Quantification of HABP+ area per total eSMG area (DAPI+ area) (n = 4). (c) Bright field and immunofluorescence images of e13.5 eSMG treated with DMSO, 0.1 mM 4-MU, or 1.0 mM 4-MU (48 hr after the treatment; blue: DAPI, green: c-Kit, red: CD31; Black scale bar = 500 μ m, white scale bar = 200 μ m). (d) Quantification of bud number of eSMGs from **Figure 5c** (n = 4). (e) Quantification of c-Kit+ area within a total eSMG area (DAPI+) based on the immunofluorescence images in **Figure 5c** (n = 4). Data are expressed as average \pm s.e.m. One-way ANOVA is performed with Tukey's multiple comparison tests. Significance is set to **: p < 0.01, ***: p < 0.005, ****: p < 0.001.

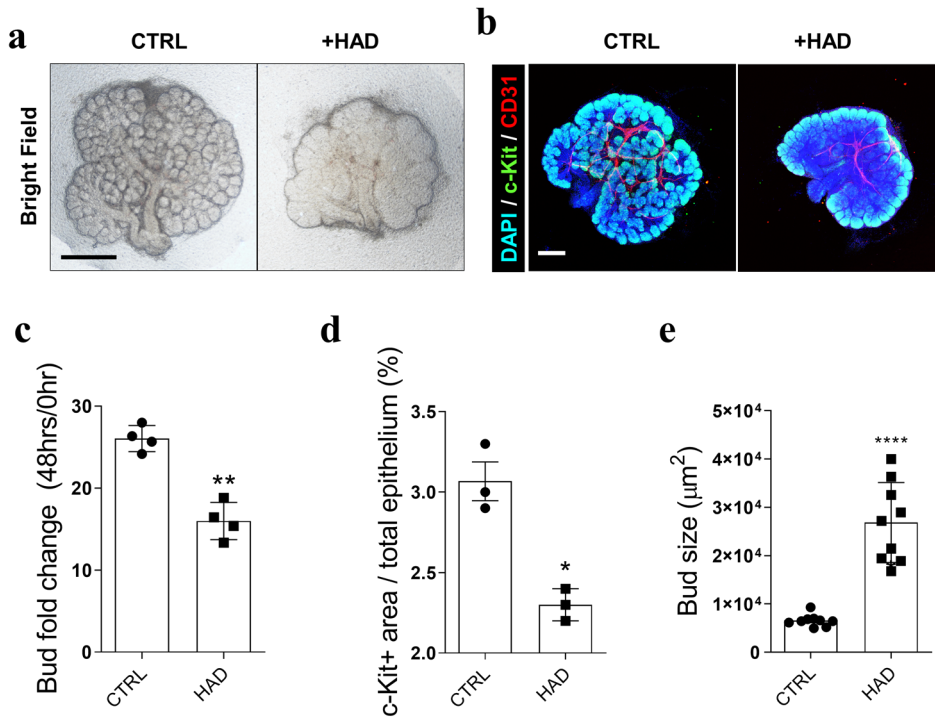


Figure 6. Effect of HAD on developing eSMGs

(a) Bright field and (b) immunofluorescence images of eSMG treated with hyaluronidase (HAD) (48 hr after the treatment; blue: DAPI, green: c-Kit, red: CD31; black scale bar = 500 μm , white scale bar = 250 μm). (c) Quantification of bud fold change (number of buds at 48 hrs / number of buds at 0 hr) on bright field images in **Figure 6a** ($n = 4$). (d) Quantification of c-Kit⁺ area within an eSMG epithelium based on the immunofluorescence images in **Figure 6b** ($n = 4$). (e) Quantification of bud sizes in each eSMG ($n=8$). Data are expressed as average \pm s.e.m. Unpaired t-test with Welch's correction is used. Significance is set to *: $p < 0.05$, **: $p < 0.01$, ****: $p < 0.001$. Each image is representative of 3~4 experimental replicates.

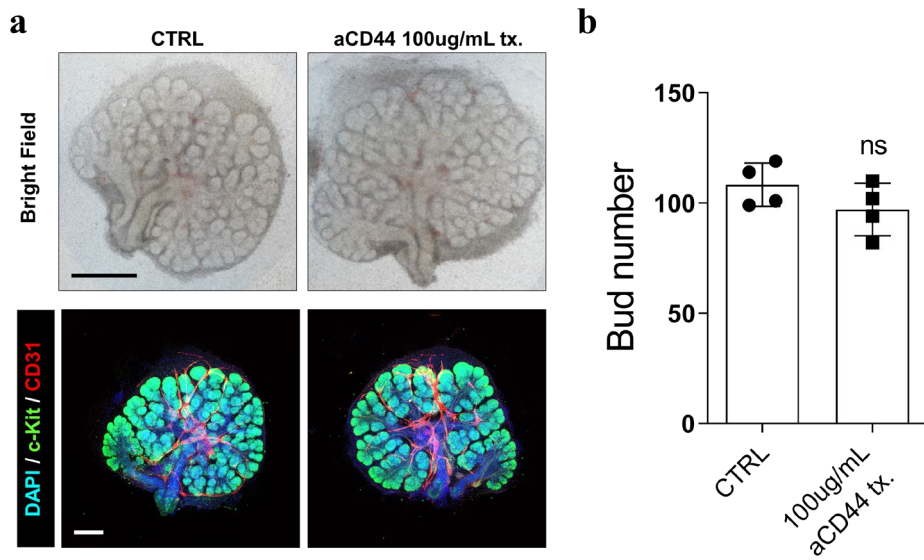


Figure 7. Effect of aCD44 on developing eSMGs

(a) Bright field and immunofluorescence images of eSMGs treated with/without 100 $\mu\text{g}/\text{mL}$ aCD44. (48 hr after the treatment; blue: DAPI, green: c-Kit, red: CD31; Scale bar = 500 μm). Each image is representative of 3~4 experimental replicates. (b) Quantification of bud number based on the bright field images from **Figure 7a** ($n = 4$). Data are expressed as average \pm s.e.m. Unpaired t-test with Welch's correction is used. ns = non-significant ($p > 0.05$).

Molecular weight-dependent role of HA on eSMG branching morphogenesis and progenitor cell proliferation

HA is essential for successful branching morphogenesis and self-organization of eSMG. To examine the molecular-weight-dependent role of HA on eSMG branching, exogenous HAs with different molecular weights (5, 40, 200, and 1,000 kDa) were supplemented to *ex-vivo*-cultured eSMGs. Since both the inhibition of endogenous HA production and disruption of the structural integrity of HA decreased branching morphogenesis and the c-Kit stem/progenitor cell population, I hypothesized that the addition of exogenous HA would enhance them. However, when HAs of various molecular weights were supplemented to *ex-vivo*-cultured eSMGs, no significant change was observed (**Figure 8a** and **8b**). Due to the abundance of HA surrounding epithelial buds, it was possible that supplemented exogenous HA could not induce significant changes. Therefore, endogenous HA production was completely ablated with 4-MU prior to adding exogenous HA of different molecular weights. The full inhibition of branching morphogenesis and the c-Kit⁺ stem/progenitor cell population by 4-MU was partially, but significantly, rescued by the addition of 1,000 kDa HA, indicating their requirement for HMW HA (**Figure 9a – 9c**). Next, eSMGs were treated with HAD for 24 hr prior to supplementation with exogenous HAs of different MWs. Similar to previous results, the decreased branching and progenitor cell population due to HAD treatment was significantly recovered in 200 and 1,000 kDa HA-treated groups (**Figure 10a** and **10b**). mRNA and protein expression level of CD44 at the periphery of epithelial buds and the mesenchyme was significantly decreased by HAD treatment, but partially rescued when treated with 200 kDa HA, and fully recovered with 1,000 kDa HA treatments (**Figure 10a** and **10c**).

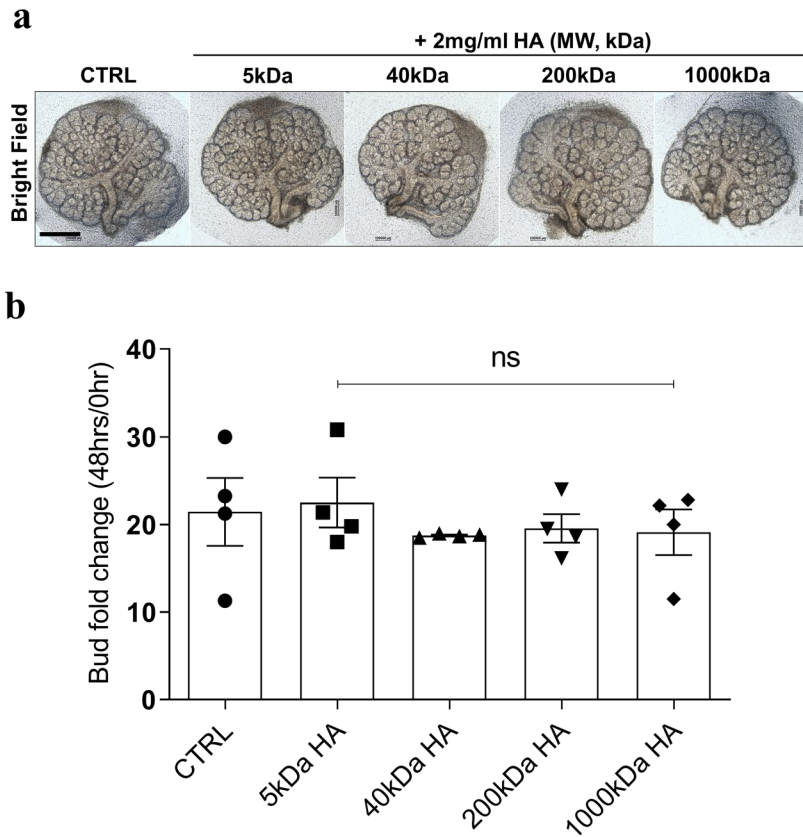


Figure 8. Effect of exogenous HA of various molecular weight on developing eSMGs.

(a) Bright field images of eSMGs treated with 2 mg/mL exogenous HA of various MW (5, 40, 200, and 1,000 kDa; 48 hr after the treatment on e13.5 eSMGs; scale bar = 500 μ m). **(b)** Quantification of bud fold change (number of buds at 48 hrs / number of buds at 0 hr) on bright field images ($n = 4$). Each image is representative of 3~4 experimental replicates. Data are expressed as average \pm s.e.m. One-way ANOVA is performed with Tukey's multiple comparison tests. ns = non-significant ($p > 0.05$).

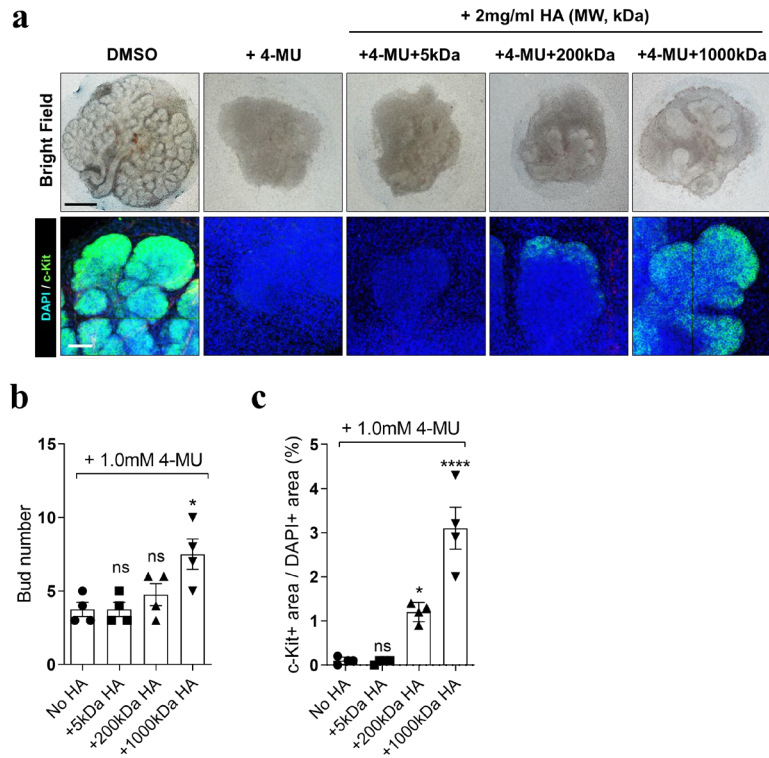


Figure 9. Rescue effects of exogenous HA of various molecular weight on HA-depleted eSMGs.

(a) Bright field (upper row) and immunofluorescence images (lower row) of eSMG treated with either DMSO, 1.0 mM 4-MU, 4-MU + 2 mg/mL 5 kDa HA, 4-MU + 2 mg/mL 200 kDa HA, 4-MU + 2 mg/mL 1,000 kDa HA (48 hr after the treatment on e13.5 eSMGs; blue: DAPI, green: c-Kit; black scale bar = 500 μ m, white scale bar = 50 μ m). **(b)** Bud number was counted based on the bright field images (n = 4). **(c)** Quantification of c-Kit⁺ area within a total eSMG area (DAPI⁺) based on the immunofluorescence images (n = 4). Each image is representative of 4 experimental replicates. Data are expressed as average \pm s.e.m. One-way ANOVA is performed with Tukey's multiple comparison tests. Significance is set to *: p < 0.05, ****: p < 0.001, ns = non-significant (p > 0.05).

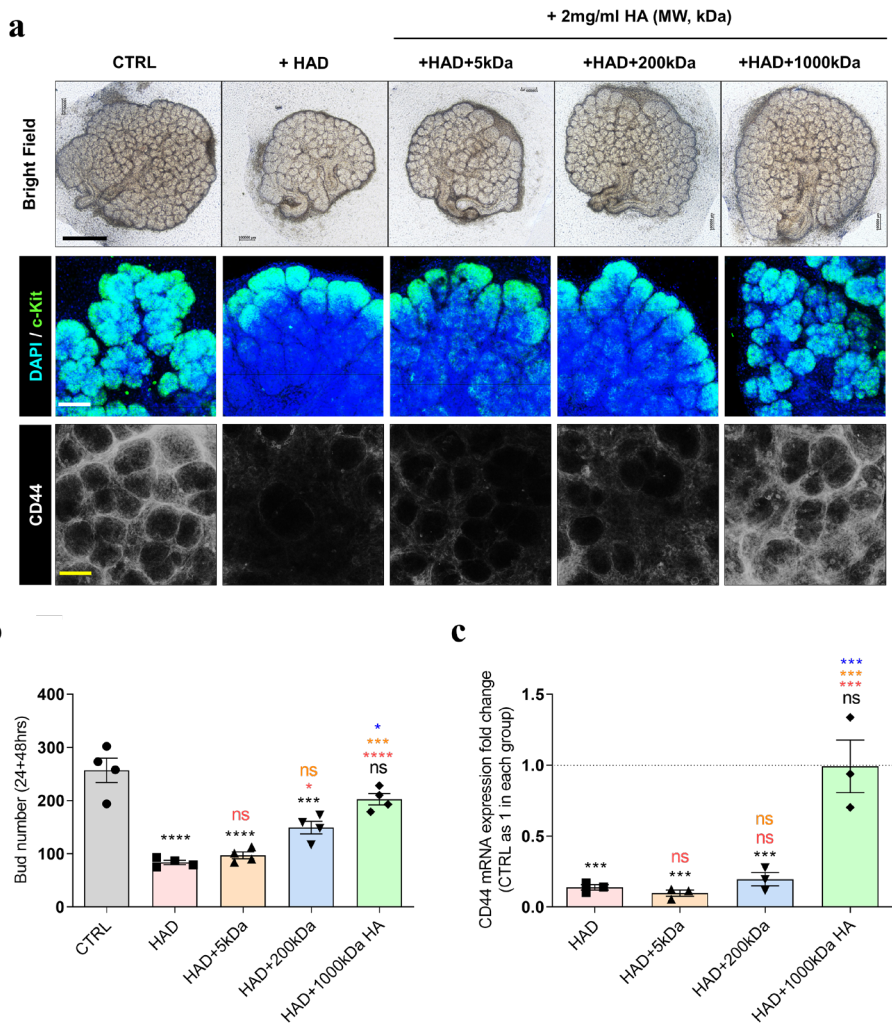


Figure 10. Rescue effects of exogenous HA of various molecular weight on HA-degraded eSMGs.

(a) Bright field (first row) and immunofluorescence images (second and third row) of eSMG treated with either HAD, HAD + 5 kDa HA, HAD + 200 kDa HA, HAD + 1,000 kDa HA (HAD treatment for 24 hrs on e13.5 eSMG, then media was replaced with normal culture media supplemented with or without HA to culture for additional 48 hrs; blue: DAPI, green: c-Kit, gray: CD44; black scale bar = 500 μ m, white scale bar = 100 μ m). Each image is representative of 4 experimental replicates.

(b) Quantification of bud number of eSMGs based on the bright field images (n = 4).

(c) mRNA expression levels of CD44 in each group (eSMG treated with either HAD, HAD + 5 kDa HA, HAD + 200 kDa HA, HAD + 1,000 kDa HA; HAD treatment for 24 hrs on e13.5 eSMG, then media was replaced with normal culture media supplemented with or without HA to culture for additional 48 hrs) were quantified by qPCR. Data are expressed as average \pm s.e.m. One-way ANOVA is performed with Tukey's multiple comparison tests. Significance is set to *: $p < 0.05$, ***: $p < 0.005$, ****: $p < 0.001$.

Role of HA in the self-organization of dissociated eSMG during organ germ formation

Next, I assessed the importance of HA in the self-organization of dissociated eSMGs. eSMGs were enzymatically digested by collagenase IV, as mentioned in previous studies (Wei et al. 2007), and then mechanically dissociated with a GentleMACS dissociator (**Figure 11, left panel**). Dissociated eSMGs were placed on a floating polycarbonate membrane and allowed to self-organize for 48 hr to form organ germs (**Figure 11, right panel**). Dissociated eSMGs were either treated with 4-MU or HAD, similar to the intact eSMGs in Figure 3. After 48 hr, bright field images were taken to evaluate the size and bud number of self-organized organ germ. A self-organized organ germ from 10,000 dissociated eSMG cells showed an average size of $1,526,305 \mu\text{m}^2$ with an average of 12 epithelial buds (**Figure 12a and 12b**). However, in a concentration-dependent manner, 4-MU-treated dissociated eSMGs could only form significantly smaller aggregates ($518,084 \mu\text{m}^2$ for 0.1 mM 4-MU-treated groups and $10,174.4 \mu\text{m}^2$ for 1.0 mM 4-MU-treated groups) and a significantly decreased number of bud (1.14 for 0.1 mM 4-MU-treated groups and 1.42 clusters for 1.0 mM 4-MU-treated groups) (**Figure 12a and 12b**). In addition, no viable c-Kit⁺ stem/progenitor cells were observed in the 4-MU-treated group, while the DMSO-treated control group showed approximately 15% of c-Kit⁺ area within an organ germ (**Figure 12a and 12c**). Similarly, when dissociated eSMG was treated with HAD, the bud number within an organ germ was significantly decreased (from 15 to 4) (**Figure 13a and 13b**). As observed in **Figure 6**, HAD-treated organ germs showed fewer but larger epithelial buds, indicating that these buds were unable to undergo branching morphogenesis (**Figure 13a and 13b**). The c-Kit⁺

progenitor cell population was also significantly decreased in the HAD-treated group, by 90% (**Figure 13a** and **13c**). These results indicate that the presence of intact polymeric form of HA is crucial for the self-organization and formation of organ germs.

Lastly, role of CD44 receptors in dissociated eSMGs was explored by treating 100 $\mu\text{g/mL}$ aCD44 on freshly dissociated e13 eSMG cells for 48 hrs. Different from the results of aCD44 treatment on intact eSMGs, blocking of both mesenchymal and epithelial CD44s significantly inhibited the organ germ formation with decreased bud number and c-Kit expression (**Figure 14a – c**). These results suggest that interaction between epithelial CD44 and mesenchymal HA might be a crucial factor for the reorganization of dissociated eSMG cells and maintenance of c-Kit⁺ stem/progenitor cell population within an organ germ.

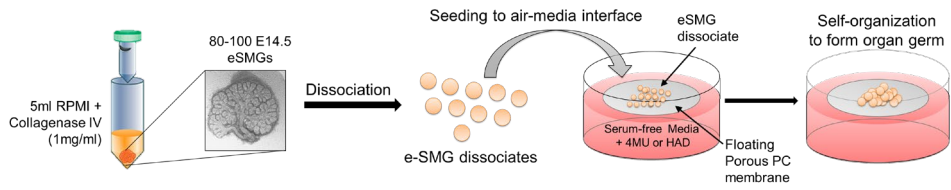


Figure 11. Schematic diagram of embryonic organ germ formation

Schematic illustration of enzymatic/mechanical dissociation of e14.5 eSMGs and subsequent seeding on the floating PC filter membrane to form organ germ.

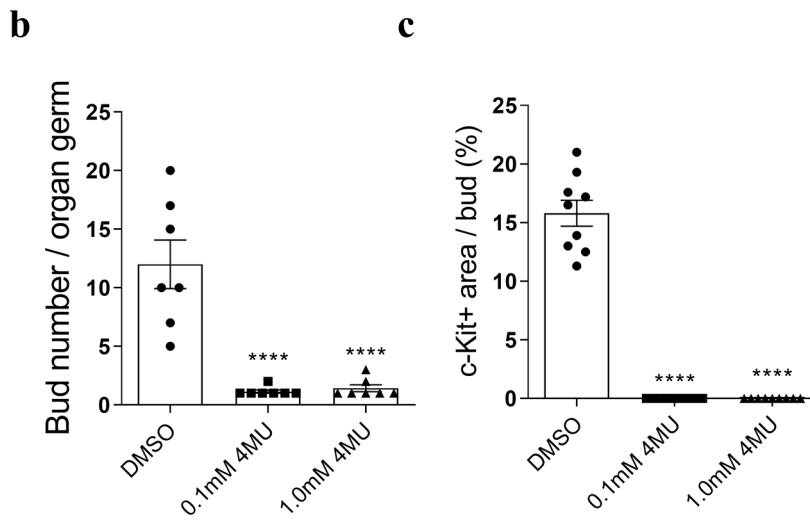
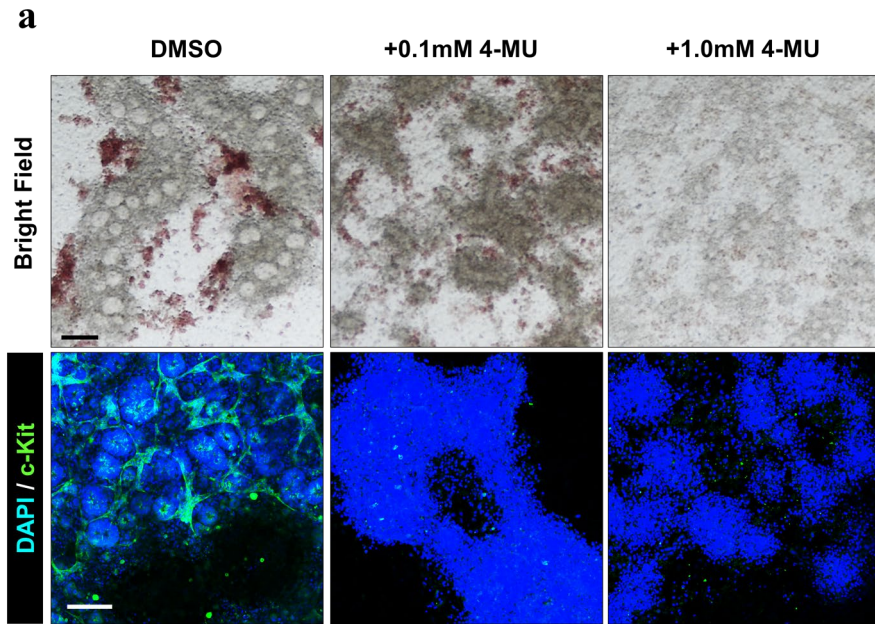


Figure 12. Effect of 4-MU on embryonic organ germ formation

(a) Bright field and immunofluorescence images of eSMG dissociates 48 hr after seeding with treatment of DMSO, 0.1 mM 4-MU, or 1.0 mM 4-MU (blue: DAPI, green: c-Kit; black scale bar = 200 μ m, white scale bar = 100 μ m). The red-colored area in the bright field images are red blood cells. **(b)** Quantification of bud number within an organ germ based on the bright field images (n = 7). **(c)** Quantification of

c-Kit⁺ area per bud within an organ germ based on the immunofluorescence images (n = 9). Data are expressed as average \pm s.e.m. One-way ANOVA is performed with Tukey's multiple comparison tests. Significance is set to ****: $p < 0.001$.

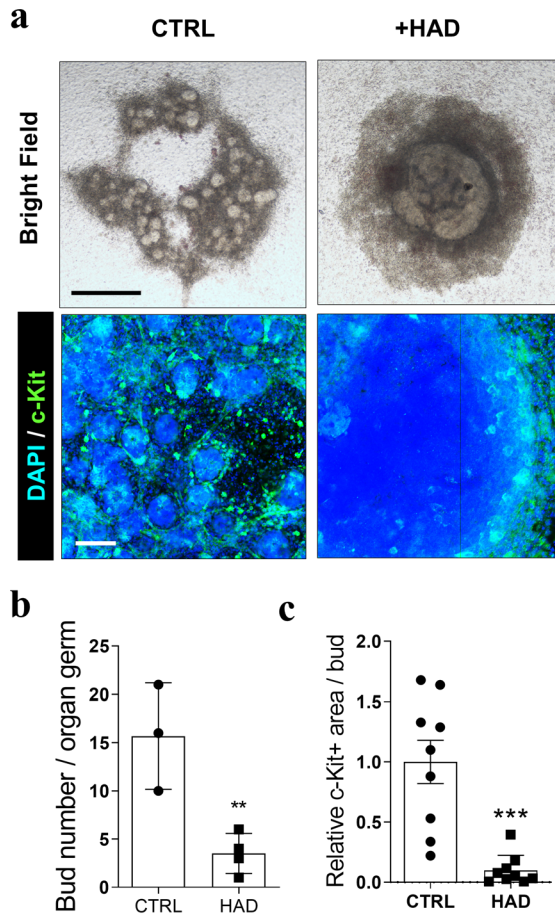


Figure 13. Effect of HAD on embryonic organ germ formation

(a) Bright field and immunofluorescence images of eSMG dissociates 48 hr after seeding with or without HAD treatment (blue: DAPI, green: c-Kit; black scale bar = 500 μ m, white scale bar = 100 μ m). (b) Quantification of epithelial bud number per organ germ with/without treatment of HAD for 48 hrs based on the bright field images from **Figure 13a** (n for CTRL group = 3, n for HAD-treated group = 4). (c) Quantification of relative c-Kit⁺ area per epithelial bud based on the immunofluorescence images from **Figure 13a** (n = 9). Data are expressed as average \pm s.e.m. Unpaired t-test with Welch's correction is used. Significance is set to **: p < 0.01, ***: p < 0.005.

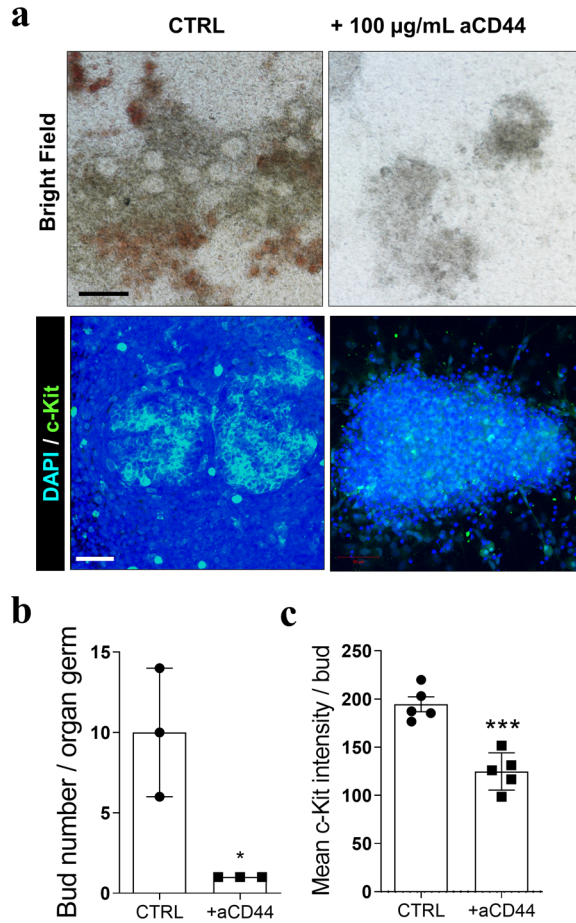


Figure 14. Effect of aCD44 on embryonic organ germ formation

(a) Bright field and immunofluorescence images of eSMG dissociates 48 hr after the treatment with/without 100 $\mu\text{g/mL}$ anti-CD44 blocking antibodies (aCD44) (blue: DAPI, green: c-Kit; black scale bar = 200 μm , white scale bar = 50 μm). (b) Quantification of epithelial bud number per organ germ with/without treatment of 100 $\mu\text{g/mL}$ aCD44 for 48 hrs based on the bright field images ($n = 3$). (c) Quantification of relative c-Kit⁺ area per epithelial bud based on the immunofluorescence images ($n = 5$). Data are expressed as average \pm s.e.m.

Unpaired t-test with Welch's correction is used. Significance is set to *: $p < 0.05$,
***: $p < 0.005$.

Molecular weight-dependent enhancement of HA on organ germ formation

To observe whether the supplementation of exogenous HA could improve the self-organization process of organ germ formation, culture medium was conditioned with 2 mg/mL of 5, 40, 200, or 1,000 kDa HA. Unlike the results with intact eSMGs, the addition of exogenous HA in solution significantly increased the bud number of organ germs in a molecular weight-dependent manner (**Figure 15a** and **15b**). No significant increase in bud number of an organ germ was observed when 5 or 40 kDa HA were added, but 200 and 1,000 kDa HA supplementation significantly enhanced the bud number of organ germs (**Figure 15a** and **15b**). Compared to 200 kDa HA-treated groups, 1,000 kDa HA-treated groups were further increased in bud number, indicating that the enhancement of organ germ formation had a positive relationship with the molecular weight of HA (**Figure 15a** and **15b**). The c-Kit⁺ cell population of organ germs was also significantly elevated by adding either 200 or 1,000 kDa HA, but there was no change in c-Kit expression when treated with LMW HAs (**Figure 15c** and **15d**).

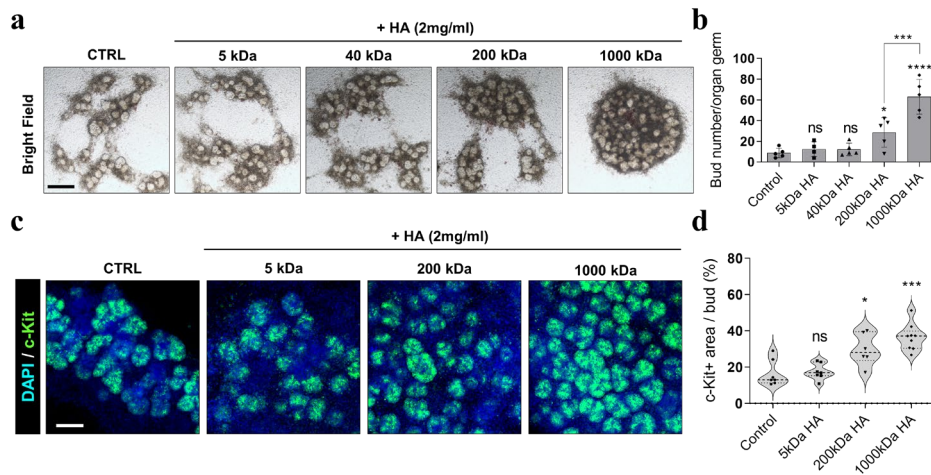


Figure 15. Molecular weight-dependent enhancement effect of HA on embryonic organ germ formation

(a) Bright field images of eSMG dissociates treated with exogenous HA of various MW for 48 hr (5, 40, 200, and 1,000 kDa; scale bar = 250 μ m). **(b)** quantification of bud number per organ germ based on the images in **Figure 15a** ($n = 5$). **(c)** Immunofluorescence images of eSMG dissociates treated with exogenous HA of various MW for 48 hr (5, 200, and 1,000 kDa; blue: DAPI, green: c-Kit, scale bar = 100 μ m). **(d)** Quantification of c-Kit⁺ area per epithelial bud ($n = 7\sim 9$). Data are expressed as average \pm s.e.m. One-way ANOVA is performed with Tukey's multiple comparison tests. Significance is set to *: $p < 0.05$, ***: $p < 0.005$, ****: $p < 0.001$. ns = non-significant ($p > 0.05$).

Presentation form-dependent enhancement of HA on organ germ formation

Next, I examined the effect of the presentation form of HA on organ germ formation. Solubilized and surface-immobilized forms of 1,000 kDa HA were introduced to dissociated eSMG cells. To immobilize chemically unmodified HA molecules on the PC membranes, one-pot co-immobilization of HA and polydopamine (PD) was performed. Briefly, the PC membranes were immersed in a solution of 2 mg/mL dopamine and 2 mg/mL HA (1,000 kDa) for 24 hr in pH 8.0 Tris buffer, as described in a previous study (Kang et al. 2012) (**Figure 16**).

To confirm the HA coating on the PC membranes, Alcian blue staining, water contact angle measurement, and SEM imaging were employed. The PD/HA-co-immobilized PC membrane stained a strong blue color after the Alcian blue staining, while no color was detected in the control, HA, or PD-immobilized PC membranes (**Figure 17**, first row). The water contact angle analysis also confirmed the presence of PD or PD/HA coating on the surfaces (**Figure 17**, second row). The water contact angle of bare PC membrane was 67.2° , and that of PC membranes incubated with HA alone showed no difference (66.9°), showing there had been no HA adsorption in the absence of PD. However, PD and PD/HA-immobilized PC membranes had significantly decreased water contact angles (9.7° and 16.9° , respectively), indicating the immobilization hydrophilic PD or PD/HA molecules on the surfaces (**Figure 17**, second row). Scanning electron microscopy (SEM) images of PD/HA-co-immobilized PC membrane showed distinctive topological patterns on PD-coated and bare PC membranes (**Figure 17**, third row). Heavily packed spherical PD nanoparticles were observed on PD-immobilized surfaces, but approximately $1\text{-}\mu\text{m}$ -

sized HA islets were uniformly distributed on the PD/HA-co-immobilized surface (**Figure 17**, third row).

To test whether the surface-immobilized HA could also enhance self-organization, the organ germ formation test was performed on the PD/HA-co-immobilized surfaces. Compared with CTRL groups, there was a significant increase in the bud number and c-Kit expression for both solubilized HA (HA(Sol)) and PD/HA-co-immobilized (PD/HA(Im)) groups (**Figure 18a – 18c**). However, no such enhancement effect was observed in either the PD-immobilized (PD(Im)) or HAD pre-treated PD/HA(Im) (PD/HA(Im)+HAD) groups, suggesting that HMW HA was responsible for the enhancement of organ germ formation (**Figure 18a – 18c**). Further culturing up to 120 hr allowed the c-Kit⁺ progenitor cells in the HA(Sol) and PD/HA(Im) groups to successfully differentiate into acinar cells expressing aquaporin-5 (AQP5) (**Figure 18a** third row and **18d**). Only a few AQP5⁺ acinar cells were detected in CTRL, PD(Im), and PD/HA(Im)+HAD groups after 120 hr (**Figure 6c** and **6f**). PD(Im) group showed apical localization of AQP5, similar to the matured salivary glands, but irregular and random localization of AQP5 was detected in CTRL, HA(Sol), PD(Im), and PD/HA(Im)+HAD groups (**Figure 18a**, third row). I also tested whether the organ germs formed in different conditions express salivary gland-specific markers including CK18, CK5, and CK14. Organ germs in CTRL group expressed CK18 and CK14, but no CK5 expression was detected (**Figure 19**). However, all CK18, CK14, and CK5 were detected in HA(Sol) and PD/HA(Im) groups (**Figure 19**). Expression levels of these markers were highest in PD/HA(Im) group, indicating that the organ germs generated on PD/HA(Im) surface are the most similar to the mature salivary glands (**Figure 19**).

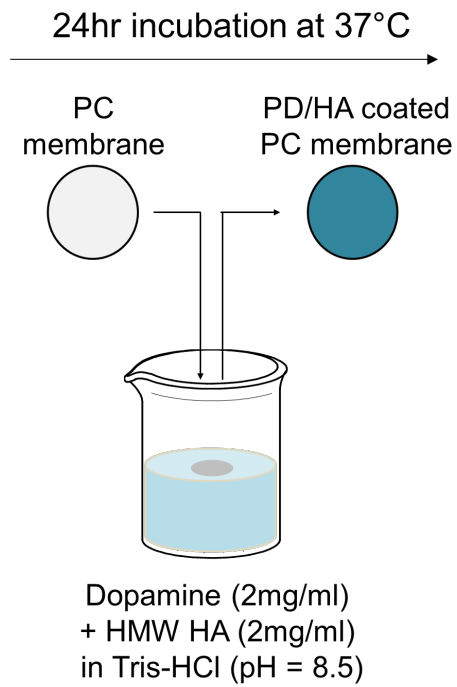


Figure 16. Schematic diagram of polydopamine (PD)/HA co-immobilization on the PC membrane.

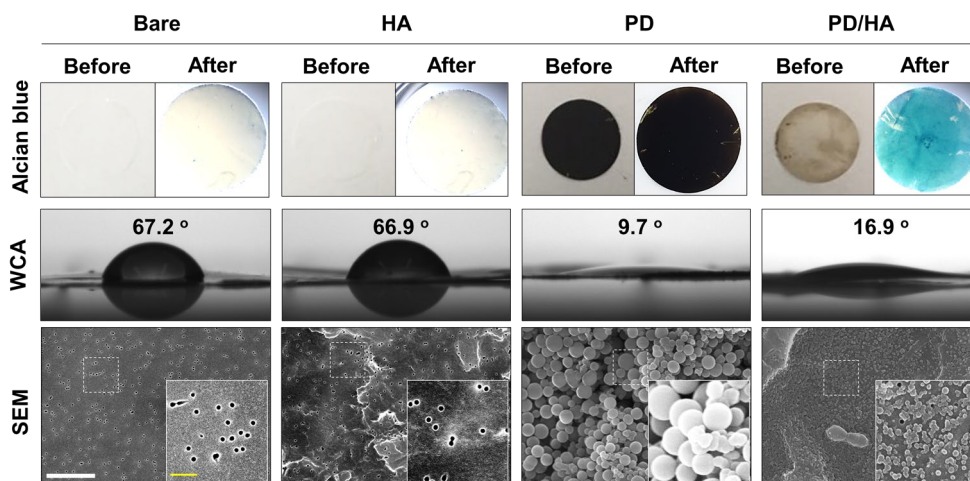


Figure 17. Physicochemical characterization of bare, HA, PD, and PD/HA – coated PC membrane surfaces

Bright field images of Alcian blue-stained PC membranes immersed in Tris-HCl (Bare), Tris-HCl containing HA (HA), Tris-HCl containing PD (PD), and Tris-HCl containing PD and HA (PD/HA) for 24 hr (first row). Water contact angle of each PC membrane (second row). SEM images of the surface of each PC membrane. Further magnification view is in a square with white border line (third row; white scale bar = 2.5 μm , yellow scale bar = 0.5 μm).

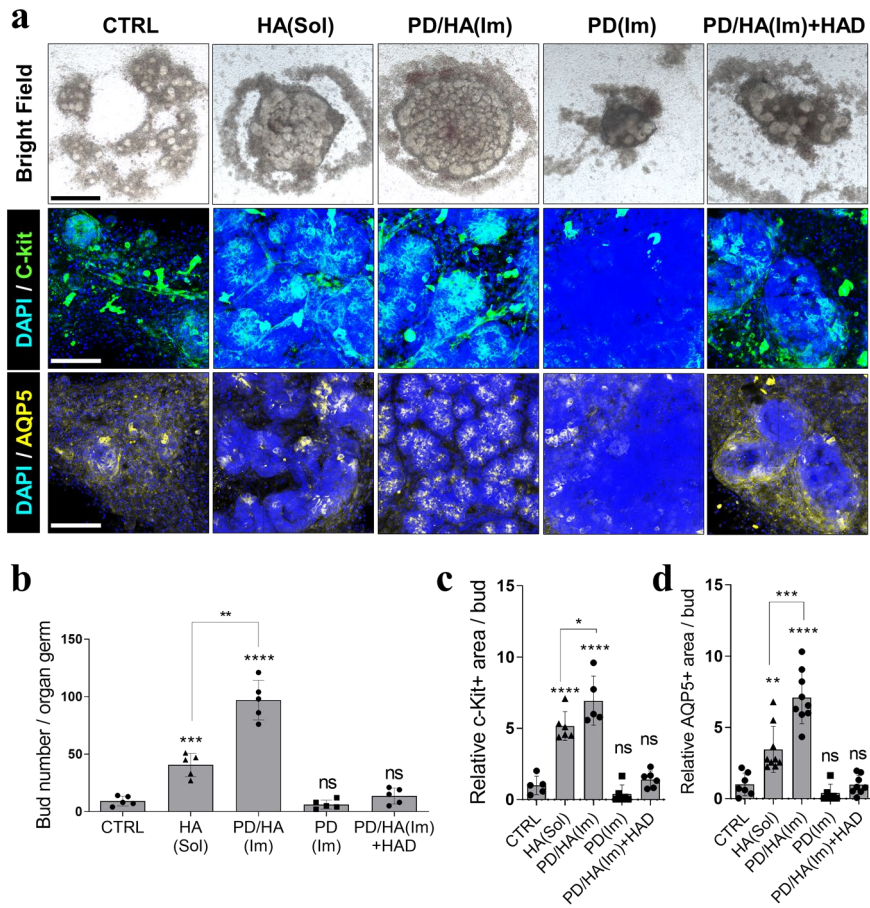


Figure 18. Effect of HA's presentation forms on embryonic organ germ formation

(a) Bright field (first row) and immunofluorescence images (second and third row) of self-organized eSMG organ germs on each condition; control (CTRL), exogenous HA supplementation in solubilized form (HA(Sol)), co-immobilized PD/HA on PC membrane (PD/HA(Im)), immobilized PD on PC membrane, and HAD-treated PD/HA-immobilized PC membrane (PD/HA(Im)+HAD) (For second row, DAPI in blue and c-Kit in green. For third row, DAPI in blue and AQP5 in green; black scale bar = 500 μ m, white scale bar = 100 μ m). (b) Bud number of self-organized organ germs in each condition quantified based on the bright field images (n = 5). (c)

Relative c-Kit⁺ area of an epithelial bud is quantified. CTRL as 1. (n = 5). **(d)**
Relative AQP5⁺ area of an epithelial bud is quantified. CTRL as 1. (n = 5). Each image is representative of four experimental replicates. Data are expressed as average \pm s.e.m. One-way ANOVA is performed with Tukey's multiple comparison tests. Significance is set to **: $p < 0.01$, ***: $p < 0.005$, ****: $p < 0.001$. ns = non-significant ($p > 0.05$).

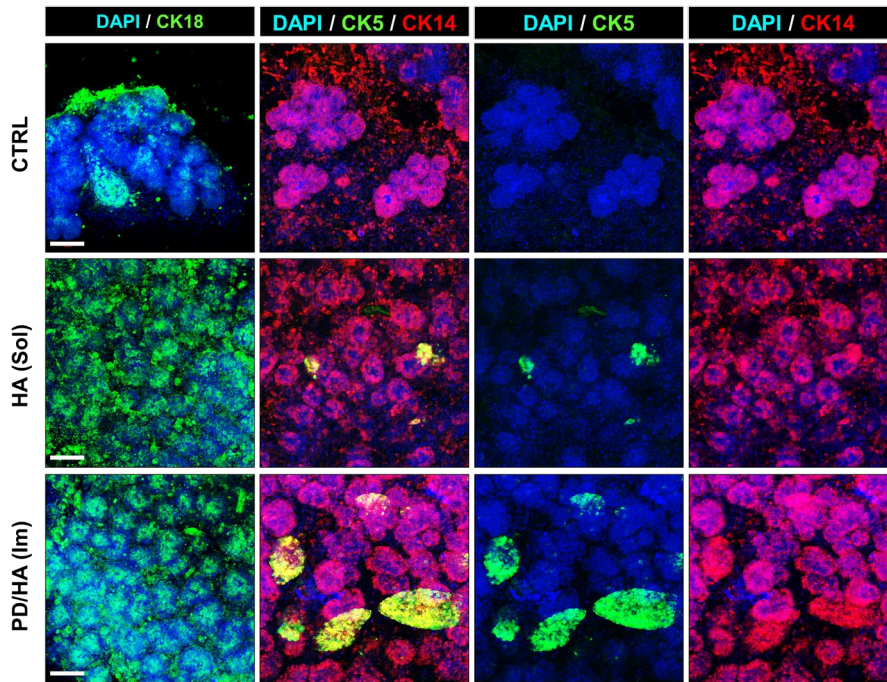


Figure 19. Confirmation of salivary gland-specific markers in embryonic salivary gland organ germs.

CK18, CK14, and CK5 immunostaining results of organ germs cultured with different conditions for 120 hrs. Scale bar = 100 μ m.

Discussion

During the past decade, various salivary gland tissue engineering techniques have been developed for salivary gland regeneration (Lee et al. 2020b; Ogawa et al. 2013; Pradhan-Bhatt et al. 2013; Pradhan et al. 2010; Srinivasan et al. 2017). However, it has been difficult to replace the existing salivary glands, primarily because the epithelial cells encapsulated in conventional scaffolds could only form independent acinar structures with limited sizes. To replicate the organized structures of native salivary glands with a high degree of complexity, the recapitulation of their developmental process has been proposed (Ogawa et al. 2013; Tanaka et al. 2018). One study completely replaced of entire salivary glands with fully functional bioengineered salivary gland organ germs that were generated from fetal salivary gland tissues (Ogawa et al. 2013). However, the technique remains challenging because 1) early embryonic salivary gland-like cells should be generated from patient-derived induced pluripotent stem cells, 2) proper chemical and physical developmental cues should be applied, and 3) the cells should form salivary gland organ germs of transplantable size. The developmental roles of chemical cues such as EGF (Kashimata et al. 2000; Morita and Nogawa 1999; Umeda et al. 2001), FGF7 (Morita and Nogawa 1999), and FGF10 (Jaskoll et al. 2005; Lombaert et al. 2013; Patel et al. 2007) and physical cues such as ECM components (Cutler 1990; Kleinman et al. 2003) have been well-characterized by previous studies. However, no study has been done determining the role of HA on salivary gland organogenesis and organ germ formation. Herein, I elucidated the role of HA during salivary gland

organogenesis and applied the findings to the efficient *in vitro* generation of salivary gland organ germs.

My results showed that HA was continuously involved in organogenesis with spatiotemporal dynamicity. According to the database from Salivary Gland Molecular Anatomy Project (<https://sgmap.nidcr.nih.gov/sgmap/sgexp.html>) (Musselmann et al. 2011), The isoform of Has dominantly expressed in developing salivary glands was Has-2, rather than Has-1 or Has-3. Has-2 gene expression is highest at e14 then gradually decreases to a minimum at the adult state (Musselmann et al. 2011). Similar to the Has-2 expression pattern, data in this study also show that the density of tissue-resident HA gradually decreases as salivary glands mature. On the contrary, CD44 expression level is highest in the fully matured salivary glands (Musselmann et al. 2011), suggesting that local HA concentrations might be a limiting factor for CD44-mediated cellular events. In fact, elevated levels of HA, HA synthesis activity, and CD44 expression are observed in various salivary gland tumors, showing that the spatiotemporal regulation of HA in salivary glands is critical for maintaining tissue homeostasis (Fujita and Ikeda 2012; Takeuchi et al. 1981). As shown in the results, either inhibition of HA synthesis or degradation of HA significantly interrupting development, suggesting that both the presence and structural integrity of HA is crucial for proper salivary gland organogenesis and organ germ formation. Developmental perturbation by HAD can be explained by the fact that the minimal binding size of HA to CD44 is six monosaccharide units (Misra et al. 2015) while the final product of the enzymatic degradation of HA by HAD from *S. hyalurolyticus* is a disaccharide (Hynes and Walton 2000).

I also found that HA molecules with different MWs can exert different biological activities on salivary gland organogenesis and self-organization. In my results, only HMW HA was able to restore the branching of eSMGs treated with 4-MU or HAD. In addition, only HMW HA enhanced the self-organization and proliferation of c-Kit⁺ progenitor cells within an organ germ. These results support previous studies where HMW HA promotes proliferation of corneal epithelial cells (Inoue and Katakami 1993), neural stem cells (NSCs) (Khaing and Seidlits 2015), mouse adipose-derived stem cells (Chen et al. 2007), and embryonic epicardial cells during cardiogenesis (Craig et al. 2010). In cancer, however, the pattern of HA MW-dependent biological effects is reversed. For example, in cancer cells, LMW HA has a stronger interaction with CD44 than HMW HA, consequently promoting cell survival, proliferation, and invasion, all of which were inhibited by HMW HA (Maharjan et al. 2011; Morrison et al. 2001; Naor et al. 2002; Sapudom et al. 2017). As mentioned above, since the consequences of interactions between HA and its receptor are cell-type-dependent, elucidation of exact mechanism of HMW HA-mediated effects in eSMG composed of heterogenous cell population, is quite challenging. However, it was at least confirmed that blocking of mesenchymal CD44 did not exert any significant change in branching or c-Kit⁺ stem/progenitor cell population in intact eSMGs, while blocking of both mesenchymal and epithelial CD44 in dissociated condition inhibited branching and c-Kit⁺ stem/progenitor cell population. Although there are significant physiological and structural differences in intact and dissociated eSMGs, my results implicate that the HA-mediated effects in eSMG branching morphogenesis are largely mediated by epithelial CD44. However,

experimental techniques enabling more precise and selective blocking of either mesenchymal or epithelial CD44 in intact eSMGs is required to prove the hypothesis.

For the detail mechanism involved in the MW-dependent effects of HA, I suspect that it is closely related to the expression level of CD44 and/or CD44's degree of interaction with HA. According to my observation, treatment of HAD, which increased amount of extremely low-molecular-weight (ELMW) HA (ranged from 0.8 ~ 8 x 10⁵ Da) by breaking HMW HA, significantly decreased both CD44 expression and branching of intact eSMGs. However, addition of HMW HA following HAD treatment significantly recovered both CD44 expression and branching of intact eSMG. These results suggest that ELMW HA may decrease CD44 expression, while HMW HA increase CD44 expression. Similar results are observed in peripheral blood mononuclear cells, showing that LMW HA decreases CD44 expression (Maharjan et al. 2011). Further study using purified HA of MW less than 5 kDa, which was used as LMW HA in this study, will be required to prove the aforementioned hypothesis. Another explanation is that the interaction between CD44 and HA is multivalent, and thus that HA with higher MWs possess stronger binding affinities to CD44 (Wolny et al. 2010). Stronger interaction of CD44 with HA also can be achieved by CD44 clustering. HMW HA induces CD44 clustering, which sends a different cellular signal than monomeric CD44 stimulated by LMW HA (Khaing and Seidlits 2015; Sapudom et al. 2017; Yang et al. 2012a). In NSCs, HMW HA-mediated CD44 clustering promotes NSC proliferation by inhibiting TLR2/4 activity and clustering the tyrosine kinase receptor (Khaing and Seidlits 2015).

Another important factor for the assessment of HA's effect on cells and tissues is the presentation form. Many studies on the interaction between HA and cells were done in solution, whereas most of the HA molecules *in vivo* are partially immobilized on other ECM components (Naor et al. 2002). In the present work, I compared the effect of HMW HA in solution and immobilized on PC membrane surface. Since HA are naturally non-adhesive molecules, simple adsorption of HA on substrates is highly unstable (Joo et al. 2016), making it difficult to immobilize the HA on the surfaces without modifications to HA backbones. To circumvent these issues, the one-pot coating or co-immobilization method of PD and HA was used with a slight modification (Kang et al. 2012). It was noted that the PC membrane coated with pure PD was a dark black color, whereas the PC membrane coated with PD and HA was a pale brown color, suggesting that most of the HA molecules were presented towards the interface with a little PD-mediated anchorage at the membrane surfaces (Lih et al. 2016). Compared with freely moving HA molecules in solution, these spatially restricted HA molecules more physico-dynamically resemble those anchored to the surrounding ECM components *in vivo* (Sapudom et al. 2017). The surface topology of PD/HA-coated surfaces showed that HA clumps were distributed throughout the surfaces like islets. Similar patterns have been observed on surfaces coated with catechol-conjugated HA, supporting the successful immobilization of HA (Lee et al. 2020b; Lih et al. 2016). Compared to the HMW HA in solubilized form, the immobilized HMW HA exerted improved enhancement of salivary gland organ germ formation, indicating that the presentation form of HA was crucial for its biological activity. Several previous studies have also reported that immobilized HA possesses a different biological activity compared to the solubilized form in

cancer cells (Sapudom et al. 2017). This study revealed the presentation form-dependent biological effects of HMW HA on primary embryonic cells, which might provide a clue for roles of soluble HA in embryonic circulatory system and HA bound to embryonic tissues. The physical strains from an interaction between motile cells and immobile HA might be transduced throughout cell cytoskeletons of cells to induce intracellular signaling. Salivary gland organogenesis is especially sensitive to the physical properties of contacting substrates. For example, embryonic salivary glands cannot properly branch on stiff substrates (Lee et al. 2020b; Sathi et al. 2017), but these stiffness-induced negative effects can be reduced by introducing RGD peptides on the substrates (Miyajima et al. 2011), supplementing with macrophage colony stimulating factor (Sathi et al. 2017), or coating the substrate with catechol-conjugated hyaluronic acids (Lee et al. 2020b). This suggests that the proper amount of force transduced throughout cells is crucial for the salivary gland organogenesis.

Although I mainly reported the enhancement effects of immobilized HMW HA on c-Kit⁺ cells in embryonic salivary glands, it seems that immobilized HMW HA can also enhance other stem/progenitor cell populations such as K14⁺ and K5⁺ cells. K14⁺ cells are considered as adult salivary gland stem cells which have ability to regenerate ductal compartments and to form spheroid structure called “salisphere” (Kwak et al. 2018; May et al. 2018). In contrast, c-Kit⁺ cells in adult salivary glands do not function as regenerative stem cell thus they only possess multipotent stem/progenitor cell properties during organogenesis (Kwak et al. 2018; May et al. 2018). If PD-based HA immobilization system used in this study also support repopulation of other adult salivary gland stem cell populations, it can be more practically applied to salivary gland tissue engineering. However, further studies will

be required to prove such hypothesis and mechanisms behind it. The promotion of salivary gland stem/progenitor cell repopulation is a challenging but worthy subject. Based on my findings, various biomaterials with immobilized HMW HA can be utilized as an *in vitro* salivary gland progenitor cell culture platform.

CHAPTER II

Development of NiCHE Platform: Nature-inspired Catechol-conjugated Hyaluronic Acid Environment Platform for Salivary Gland Tissue Engineering

This chapter is a slightly modified version of “**NiCHE platform: nature-inspired catechol-conjugated hyaluronic acid environment platform for salivary gland tissue engineering**” published in *ACS Applied Materials & Interfaces* and has been reproduced here with the permission of the copyright holder and co-authors.

Introduction

The most critical procedure for successful tissue engineering is the development of culture methods for cells or functional units of an organ. The functional units in various organs include nephrons in the kidney, beta-islets in the pancreas, endothelial cell layers in blood vessels, and hepatic lobules in the liver. In general, it is necessary to construct microenvironments resembling *in vivo* physiological characters to maximize functions in the process of organotypic culture. For example, for culturing fully functional endothelial cell layers *in vitro*, it is important to apply shear force to the cells by generating continuous media flow (Imberti et al. 2002). In addition, there are structurally complex organs consisting of multi-cellular subunits in which their functions are highly reliant on organ-specific structures and balances between heterogeneous cell populations. Most of the epithelial organs such as lungs, kidneys, pancreases, mammary glands, and salivary glands are representative examples. A common yet distinctive character of such organs is to show a unique developmental process called “branching morphogenesis” (**Figure 4**) (Costantini and Kopan 2010; Lu and Werb 2008; Patel et al. 2006; Warburton et al. 2005). However, culturing of such complex epithelial organs *in vitro* exhibits significantly retarded branching morphogenesis compared to that observed *in vivo* (Horowitz and Simons 2008; Patel et al. 2006; Yang and Young 2008). Thus, developing a culture method for epithelial organs with fully branched structure remains a great challenge.

Salivary glands, complex multi-cellular epithelial organs found in the orofacial area, show highly-branched glandular morphology. Salivary glands continuously produce

vast amount of saliva to maintain both oral and systemic health. There are three kinds of major salivary glands including parotid, submandibular, and sublingual glands (**Figure 20a**, i - iii). Salivary glands have sympathetic/ parasympathetic nerves, vasculatures, saliva-producing acini, and excretory duct structures (**Figure 20a**, the first circle). Water in saliva is drained from highly vascularized blood capillaries, and the flow direction of the produced water is from basal to apical side in acinar cells (Scheme 1a, the second circle). Aquaporin 5 (AQP5) located on the apical side of acinar cells play a role as a water channel from which the produced saliva is squeezed by physical contraction of myoepithelial cells (**Figure 20a**, the second circle). This physiological function is observed in what is called a salivary gland functional unit (SGFU), which consists of vascular endothelial, acinar, myoepithelial, and progenitor cells (Scheme 1a, the second circle).

SGFUs often become non-functional because of radiotherapy-induced tissue damage in patients related with head and neck cancers (**Figure 20b**). The damage results in severe vascular/acinar atrophy and finally Xerostomia, a significant reduction of salivary flow (**Figure 20b**) (Chambers et al. 2004; Chambers et al. 2007; Dirix et al. 2006; Pinna et al. 2015). Xerostomia leads to failures in lubrication of oral cavities, protection against infections, and production of digestive enzymes, resulting in significant adverse effects on patients' survival rates and their quality of life (Vissink et al. 2003). An implantation of SGFU prepared by a tissue engineering approach is considered the most fundamental solution to cure radiation-induced Xerostomia (**Figure 20b**). The complex structures of salivary glands may lead to the difficulties of organotypic culture *in vitro*. Thus, it is highly desirable to develop the culture method to obtain fully functional SGFUs.

A challenging question to address is that of how to develop an organotypic culture method for salivary glands exhibiting *in vivo* levels of branching morphogenesis. Observation of a progressive propagation of branching morphogenesis during the gland's organotypic culture is decisive to whether the culture method was successful. Thus, I hypothesized that if I could mimic microenvironments or interfaces contacting the site of branching morphogenesis *in vivo*, then it would be possible to enhance or accelerate branching morphogenesis *in vitro* up to a comparable level to that *in vivo*. Previous studies have revealed that hyaluronic acid (HA) is rich in embryonic primary mesenchyme (Girard et al. 1986; Singley and Solursh 1981; Solursh and Morriss 1977) and mesenchyme of various developing organs including limb buds (Singley and Solursh 1981), salivary glands (Bernfield 1977; Bernfield and Banerjee 1972; Lee et al. 2020a), liver, stomach, intestine, and kidney (Grossfeld 1957). I also preliminarily confirmed that mesenchyme of embryonic salivary glands consists of high concentrations of HA as previously reported (**Figure 1b** and **21**). Additionally, CD44-expressing vascular endothelial cells at the outermost area of eSMG mesenchyme were directly in contact with the HA, which implicated that it might have a role in neovascularization during branching morphogenesis (**Figure 22a** and **22b**). In this paper, I have developed adhesive HACA to mimic the HA-rich microenvironments of developing eSMGs. Mimicking of mesenchymal HA *in vitro* was achieved by coating HA on various substrates through catechol moieties conjugated with HA (**Figure 20c**). Since this coating platform is inspired by embryonic mesenchymal HA and mussel adhesion, I named it the “NiCHE (Nature-inspired Catechol-conjugated Hyaluronic acid Environment)” coating platform. By culturing eSMGs on NiCHE-coated substrates, their branching morphogenesis was

significantly enhanced. With this enhanced branching morphogenesis, eSMGs cultured organotypically on NiCHE interface consist of highly complex glandular structures and multiple cell populations including acinar, myoepithelial, vascular endothelial, and progenitor cells, resembling fully developed submandibular glands *in vivo*.

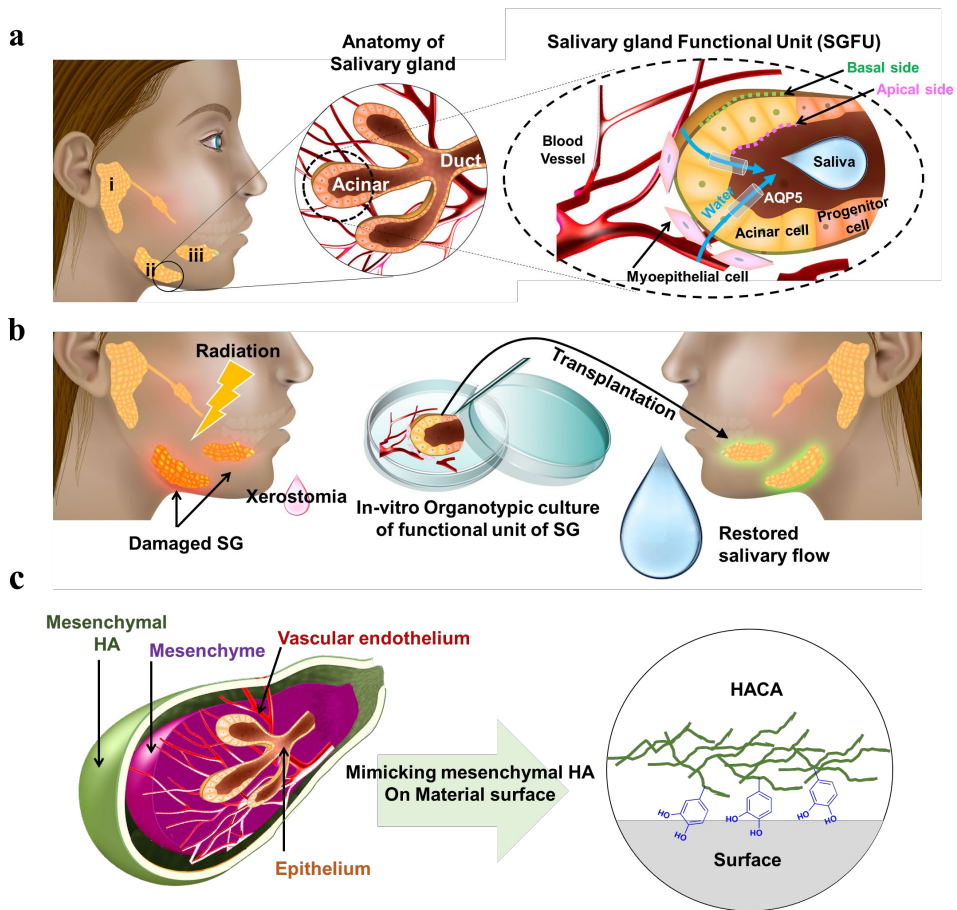


Figure 20. Schematic illustrations of salivary gland anatomy and function.

(a) Schematic illustrations of salivary gland anatomy and function. Parotid gland (i), submandibular gland (ii), and sublingual gland (iii). Branched structure of salivary gland composed of acini and duct (First circle, solid line). Salivary gland functional unit (SGFU) is composed of blood vessel, myoepithelial cells, Aquaporin 5 (AQP5)-expressing acinar cells, and progenitor cells (Second circle, long-dash). Saliva is produced by transcellular water movement from blood vessel at the basal side to apical side of acinar cell (Second circle, long-dash). (b) Schematic diagram of salivary gland damage and tissue engineering-based therapeutic approach. (c)

Schematic diagram of mimicking mesenchymal HA of developing eSMG on material surfaces by using adhesive HACA.

E14.5 (HABP staining)

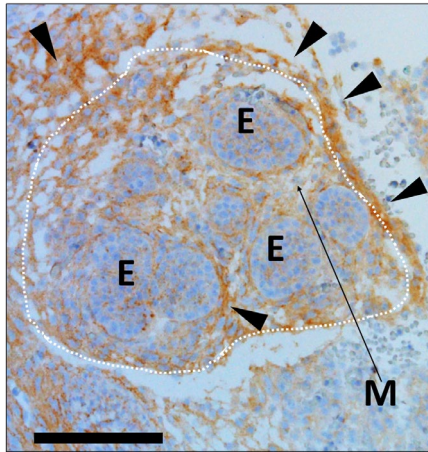


Figure 21. Presence of HA in mesenchyme of developing eSMG within e14.5 mandible

Abundant HA in mesenchyme of developing eSMG (white dotted line) is revealed by HABP staining (representative of three replicates, scale bar = 500 μ m).

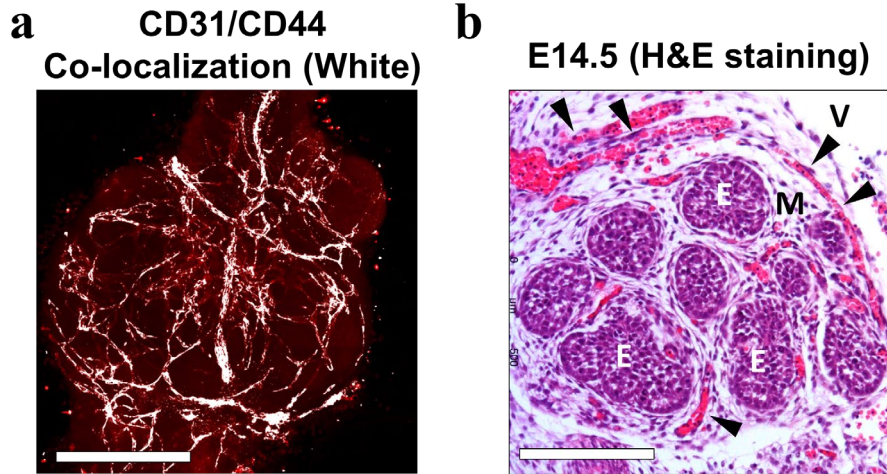


Figure 22. Distribution of CD44+ vascular endothelial structure in developing eSMGs

(a) Mesenchymal vascular endothelial cells expressing CD31 (Red) and CD44 are co-immunostained, and co-localized area is expressed as white (representative of three replicates, scale bar = 200 μ m). (b) H&E stained section of developing e14.5 mouse eSMG. Vasculature (V, black arrow), Mesenchyme (M), and Epithelium (E) are labeled (representative of three replicates, scale bar = 500 μ m).

Materials and Methods

Materials

HA was purchased from Lifecore (MW = 1.6 MDa, USA) and 1-ethyl-3-(3-dimethylaminopropyl)-carbodiimide hydrochloride (EDC) was purchased from TCI (Japan). Dopamine hydrochloride, N-hydroxysuccinimide, 3-Phenylphenol, Sodium Tetraborate, Sulfuric acid, collagenase 4, Hyaluronidase from Streptomyces hyalurolyticus, Alcian Blue solution, Agarose LE powder, polycaprolactone, and Whatman® Nuclepore™ track-etched membranes were purchased from Sigma-Aldrich (USA). All other chemicals were of analytical grade. Dulbecco's Modified Eagle Medium with F12 supplement (DMEM/F12 1:1) and Penicillin/Streptomycin were purchased from Gibco (USA).

Synthesis of HACA

HACA was synthesized using EDC coupling agents. Briefly, HA (1 g) was dissolved in 100 mL of pH 5.0 2-(N-morpholino)ethanesulfonic acid-buffered solution (MES buffer). Then, EDC (474 mg) and N-hydroxysuccinimide (285 mg) were subsequently added to the HA solution. After 30 mins activations, dopamine hydrochloride (388 mg) was added to HA solution and reacted for 12 h. During the reaction, pH of the reaction solution was adjusted to 5.5 using 1M HCl to prevent oxidation of catechol groups. The product was purified by membrane dialysis (MWCO: 3,500, SpectraPor, USA) against pH 3.0 HCl solution for 2 days and deionized water for 4 hrs and lyophilized. The degree of dopamine substitution was

calculated to be ca. 6.2 % by UV-Vis spectroscopy comparing the maximum absorbance at 280 nm wavelength of HACA and the standard curve of dopamine hydrochloride. The standard solutions of dopamine as a function of concentration were used to generate a standard curve.

HACA coating on the materials and its characterization

HA or HACA (5 mg/mL) was dissolved in DMEM/F12 1:1 1X without phenol red (Gibco, 21041-025). For HACA coating, PC membrane (Whatman Nuclepore Track-Etch Membrane, 110405) was facing HACA was floating on HACA solution with bright side facing down to HACA solution for 12 hrs under room temperature (RT). For HACA coating of stiff 4% agarose hydrogel and PCL scaffolds, materials were dipped in the HACA solutions for 12 hrs under RT. After coating, materials were gently washed with PBS twice and dried in oven. The alcian blue staining, Energy dispersive X-ray spectroscopy analysis, and water contact angle measurement were performed. For alcian blue staining, HACA-coated PC membranes were dipped in Alcian Blue solution (Sigma-Aldrich, B8438) for 10 mins and gently washed with PBS three times. Images of cross-sectioned HACA-coated PC membranes were obtained by scanning electron microscopy (SEM; Phenom ProX, ThermoFisher Scientific) at 15 kV acceleration voltage. Based on the SEM images, thickness of HACA coating was measured at 13 different points and averaged. Atomic compositions of surfaces of PC membrane, dried agarose gel, and PCL scaffold were analyzed by Energy dispersive X-ray spectroscopy attached to SEM at 15kV acceleration voltage. Density of HA coating is measured by using uronic acid quantification method developed by Filisetti-Cozzi and Carpita (Filisetti-

Cozzi and Carpita 1991). Briefly, HA or HACA-coated PC membranes were completely immersed in solution of 120 mM sodium tetraborate (221732-5G) dissolved in analytical grade sulfuric acid (339741-100ML) and incubated for 5 min at 100 °C. After that, the samples were cooled in ice for 5 min. 20 µL of 0.15 % (w/v) 3-phenylphenol (262250-5G) was added to each sample and incubated for 10 min at RT. After that, absorbance of the colored solution from each sample was measured at 540 nm by using Synergy2 Multimode Microplate Reader (Biotek, SLFPTAD). Concentration of uronic acid was calculated according to the standard curve created from 0.01, 0.05, 0.5, and 1 mg/mL HA. To obtain HA density of HACA-coated PC membrane, calculated amount of HA was divided by total area of PC membrane.

eSMG dissociation and cell attachment test

Approximately 30~50 e13.5 eSMGs were harvested from ICR mice fetus, and they were incubated in RPMI containing 1 mg/mL collagenase 4 (Sigma-Aldrich, C5138-100MG) and 0.5 mg/mL Hyaluronidase from *Streptomyces hyalurolyticus* (Sigma-Aldrich, H1136) at 37 °C for 20 mins with continuous rotation by using MACSmix Tube Rotator (Miltenyi Biotec, 130-090-753). After that, eSMGs were dissociated by gentleMACS Dissociator (Miltenyi Biotec, 130-093-235) with sequential application of hTumor1, 2, and 3 programs. Dissociated eSMGs were filtered through 70 µm MACS SmartStrainer (Miltenyi Biotec, 130-098-462). Dissociated eSMGs were washed twice with DMEM/F12 1:1(Gibco, 21041-025) media containing 1% BSA. For CD44-blocked groups, dissociated eSMG cells were mixed with 100 µg/mL *in vivo* monoclonal anti-CD44 antibody (BioXCell, BE0039). 5 µL drop containing 100000 cells was placed on bare, HA-coated, or HACA-coated PC

membrane floating on eSMG culture media. After incubating the dissociated eSMG cells for 12 hrs in cell incubator (37°C, 5% CO₂), PC membranes were gently submerged in DMEM/F12 1:1 media twice. After the washing, the PC membranes were placed on fresh 200 µL DMEM/F12 1:1 media containing 10 µL Cell Counting Kit 8 solution (Dojindo, CK04-11) and then incubated in cell incubator for 2 hrs. Media under PC membrane were collected, and absorbance at 450nm was read in Synergy2 Multimode Microplate Reader (Biotek, SLFPTAD).

Culture of *in vitro* eSMGs

eSMGs were isolated and cultured as previously reported protocols. Briefly, eSMGs were isolated from ICR mice at embryonic day 13. Harvested eSMGs were plated on bare or HACA-coated porous polycarbonate (PC) membrane (Watman, 110405), 3D printed PCL scaffolds, or agarose gel. eSMGs were cultured on the substrates with air-media interface. DMEM/F12 1:1 media (Gibco, 21041-025) supplemented with 1% Penicillin-Streptomycin (Gibco, 15140122) was used as culture media. The animal experiment protocol used in this study has been approved by Seoul National University Institutional Animal Care and Use Committee (approval number: SNU-160322-2).

Rheological studies of agarose gel

To monitor the viscoelastic properties of agarose gels, I performed the rheological analysis as a function of concentration. I used the parallel plate with a 20 mm diameter for the measurements. The frequency was varied from 0.1 Hz to 10 Hz for

the frequency sweep measurements. The elastic modulus values (solid-like property, G') of agarose gels are collected at 1 Hz frequency.

eSMG culture on stiff agarose hydrogel

Agarose LE powder (4 wt%, Sigma-Aldrich, AR1095-500G) was dissolved in PBS and heated by microwave oven and then poured into cold molds to get solidified. Solidified agarose gels were stored in PBS for the further use. Agarose hydrogels were sterilized under UV light for overnight before use.

eSMG culture on 3D-printed PCL scaffold

10 mm x 10 mm x 2 mm PCL scaffolds with porosity of 70% were 3D-printed by Bio3D Printer *In vivo* (Rokit, Korea). 40~50 kDa PCL pellets (Sigma-Aldrich, 704105) were melted at 90°C and squeezed through 200 μ m hot melting dispenser nozzle with air pressure of 500 kPa. Melted PCL extruded through dispenser was line-patterned with 90° in-fill angle. Finally produced mesh-like PCL scaffold had 20 layers with 0.1mm gap between the layers. eSMGs were placed on either bare or HACA-coated PCL scaffolds. Since the PCL scaffold had square-shaped pores (approximately 0.1 mm x 0.1 mm), media was osmotically drained up to eSMGs, thus creating air-media culture interface. PCL scaffolds were sterilized under UV light for overnight before use.

Whole mount Immunohistochemical staining of mouse fetus

Embryonic day 14.5 mouse fetus were harvested and immediately decapitated. Heads of fetus were fixed with 4% formaldehyde-PBS for two days in 4 °C, and

H&E stained or immunohistochemically stained with biotinylated hyaluronic acid binding protein (b-HABP, amsbio, AMS.HKD-BC41), which specifically binds to versican G1 domain of HA. For HABP staining, fixed e14.5 mouse fetus mandible sections in paraffin block sections were deparaffinized and rehydrated. For the deparaffinization step, the sections were incubated in dry oven at 60 °C for 1 hour and dewaxed in xylene for 4 min 5 times. The mouse mandible sections were rehydrated in 100%, 95%, and 75% ethanol for 3 min each and immersed in tap water for 5 min. For antigen retrieval step, the sections were immersed into Tris-EDTA buffer (pH 9.0) and heated up to 100 °C for 20 min. To block endogenous peroxidase activity, sections were exposed to 3% hydrogen peroxide for 6 min. After that, the sections were blocked with 5% (v/v) normal horse serum (ThermoFisher Scientific, 31874) for 30 min. Next, the sections were incubated with b-HABP-containing PBS (1:1000) for 30 min at room temperature. After that, the sections were incubated with avidin-biotin complex reagent (Vector) for 30 min. The sections were then incubated with DAB substrate kit (Vector) for 2 min. Finally, the sections were counterstained with Mayer's hematoxylin solution for 1 min. After the dehydration step (immersing in 75%, 80%, 95%, and 100% ethanol for 1 min each), the slide sections were cleared in xylene four times for 5 min each. Finally, the slide sections were mounted with Permount Mounting Medium (Fisher chemical, SP15-100) for the further analysis.

Immunofluorescence (IF) staining of eSMG

After 12 hrs, 24 hrs, 48 hrs, 72 hrs, or 120 hrs of culture, eSMGs were fixed with 4% formaldehyde-PBS for 20 mins in room temperature (RT). After the fixation eSMGs were washed and permeabilized with 0.1% Triton X100-PBS (PBSX) for 20

mins in RT. After that eSMGs were blocked by PBSX containing 10% Normal donkey serum (NDS, Sigma-Aldrich, D9663) and 1% Mouse on Mouse blocking reagent (MOM, Vecta-Sheild Laboratory, BMK-2202) for 3 hrs in RT. eSMGs were then overnight incubated with primary antibodies (1:100~1:200) diluted in 0.5% Tween 20-PBS (PBST) containing 3% Bovine serum albumin (BSA) and 3% NDS at 4 °C. The primary antibody solutions were washed out with PBST for four times, 10 mins per wash. eSMGs were then overnight incubated with secondary antibodies (1:250) or Peanut Lectin Agglutinin conjugated with FITC (1:20) diluted in 0.5% PBST containing DAPI (1:1000), 3% BSA and 3% NDS at 4 °C. The secondary antibody solutions were washed out with PBST for four times, 10 mins per wash. The primary antibodies used in IF staining are as follows: rat monoclonal anti-CD44 (Abcam, ab157107, 1:100), mouse monoclonal anti-TUJ1 (R&D System, MAB1195, 1:200), rat monoclonal anti-CD31 (BD Biosciences, 557355, 1:100), rabbit polyclonal anti-CD31 (ThermoFisher Scientific 1:100), goat polyclonal anti-c-kit (R&D System, AF1356, 1:100), rabbit polyclonal anti-E-cadherin (Cell Signaling Technology, 3195S, 1:100), rabbit polyclonal anti-AQP5 (Alomone, AQP-005, 1:200), rabbit polyclonal anti-cleaved caspase 3 (Cell Signaling Technology, 9664S, 1:200), rabbit polyclonal anti-Phospho-p44/42 MAPK (Cell Signaling Technology, 9101S, 1:100), and rabbit polyclonal anti-ki67 (ThermoFisher Scientific, 14-5698-82, 1:100) antibodies.

Imaging procedures for eSMGs Morphological analysis of eSMGs was performed by Nikon digital inverted fluorescence microscope (Nikon, Ti). Immunofluorescence staining images were obtained by Confocal Laser Scanning Microscope (Carl Zeiss, LSM700) equipped with 10X, 20X, and 40X Plan-Apochromat lens (Carl Zeiss), and

405, 488, 555, and 647 nm excitation lasers were used. For each image, 3~4 z-sections were taken by the CLSM, and then merged together by Maximum intensity projection tool in Zen 2010 Blue software (Carl Zeiss).

Data analysis

Water contact angle was calculated by using ImageJ. Bud number was manually counted based on the images taken by the inverted microscope. Co-localization or fluorescence intensity and area were measured by Zen 2010 Blue software (Carl Zeiss). Total epithelium area of eSMGs were determined by their morphology and each area was measured by SABIA software. Fractal dimension (FD) values of vasculature were calculated by FracLac plugin of ImageJ. For the statistical analysis, student t-test was used, and the significances were calculated by Prism 8.1.0 software (GraphPad Software, Inc.).

Results and Discussion

Synthesis, preparation, and characterization of HACA coating to establish NiCHE platform

The presence of HA-rich microenvironment in the developing embryonic SMG suggests that HA might play a critical role in successful *ex-vivo* culture for fully functional SGFUs. Hyaluronic acid-catechol conjugates (HACA) were synthesized by forming amide bonds between carboxylic acid groups in HA backbones and amine groups in dopamine via standard carbodiimide chemistry (**Figure 23**, left side). Conjugation of catechol found in foot pads of a marine mussel to HA provide water-resistant adhesion and coating onto a wide variety of substrates (Shin et al. 2017). A degree of catechol conjugation was 6.2% calculated by UV-Vis spectroscopy using a dopamine standard curve, indicating that approximately 6 catechol moieties were conjugated to the 100 HA monomer units (i.e., D-glucuronic acid and N-acetyl-D-glucosamine) (**Figure 23**, right side).

For the NiCHE coating applications, HACA was coated on the various surfaces including Polycarbonate (PC) filter membranes, polycaprolactone (PCL) scaffolds, and agarose hydrogels (**Figure 24**). The HA coating time is set to 12 hrs, and the HA solution after 12 hrs is shown in **Figure 25** exhibiting a slight degree of catechol oxidation. I employed PC membranes, 4 % stiff agarose hydrogel, and PCL scaffolds to test effects of HACA coating on various types of biomaterials with different physicochemical properties. Characteristics and biological responses of materials subjected to this study are briefly described in **Table 1**.

To compare the coating efficiency of HA and HACA, we performed alcian blue staining, EDAX analysis, and goniometric analysis. First, alcian blue assay was performed to stain the uronic acid molecules of HA (Scott and Dorling 1965; Scott et al. 1964). Figure 1c exhibits a significant difference in blue color intensity between HACA-coated and HA-coated substrates including PC membrane, agarose gel (dried), and PCL scaffold. HA in the absence of catechol conjugation shows marginal coating with light blue, but HACA reveals deep blue indicating a significant amount of HA coating on each surface (**Figure 26**). Energy dispersive X-ray spectroscopy analysis clearly supports the enhancement of HA coating with catechol conjugation on all three substrates. The average atomic percentage of Nitrogen is 3.17% for HA-coated PC membranes, which is not statistically different from that of bare ones (0.71%, $p=0.1692$), but significantly increased to 9.37% for HACA-coated ones ($p < 0.0001$). Similarly, Nitrogen content of HACA-coated agarose gel (4.57%) or PCL scaffolds (9.29%) are enhanced compared to that of HA-coated agarose gel (1.54%) or PCL scaffolds (1.13%) (**Table 2**). The nitrogen contents (10.45 %) of HACA alone supported the HACA coating on various substrates. Similarly, the static contact angle measurements show that the both PC membrane and PCL scaffold surfaces coated by HACA exhibits hydrophilic properties (25° for PC membrane, 14.3° for PCL scaffold) compared to bare (64.3° for PC membrane, 88° for PCL scaffold) and HA-coated (48.6° for PC membrane, 83.6° for PCL scaffold) ones (**Figure 27a and 27b**). It is noteworthy that HA is a naturally water-soluble hydrophilic polymer due to its multiple hydroxyl and carboxyl groups. The HACA coatings on the various substrates provided the hydrophilicity of surfaces by exposure of hydrophilic HA on the substrates (Kim et

al. 2017; Lih et al. 2016). To further characterize HACA coating, coating density and thickness were also measured. HACA's average coating density is found to be $782 \pm 18.6 \text{ ng/mm}^2$, significantly higher than average coating density of HA ($18 \pm 15.4 \text{ ng/mm}^2$, $p=0.0021$). A SEM image of cross-sectioned HACA-coated PC membrane shows that HA layer is uniformly deposited on a desired side of membrane (**Figure 28a**, white arrow). Average thickness of HACA coating is $848.7 \pm 96.4 \text{ nm}$ (**Figure 28b**) by interfacial adhesions of HACA with intermolecular interactions among the HACA molecules. These surface-immobilized HACA thick film formations were observed in **Figure 28c**. The catechol moiety of polymer backbones interacts with another catechol moiety via covalent bonds and noncovalent pi-pi stacking resulting thick films (Lih et al. 2016).

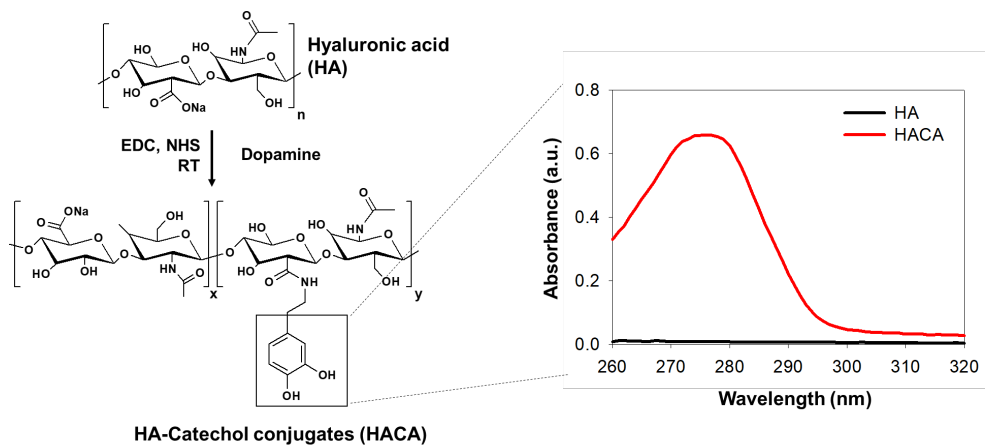


Figure 23. Synthesis of HACA

Schematic diagram of HACA synthesis (left). UV-vis spectra of HACA and HA from 260 to 320 nm (right).

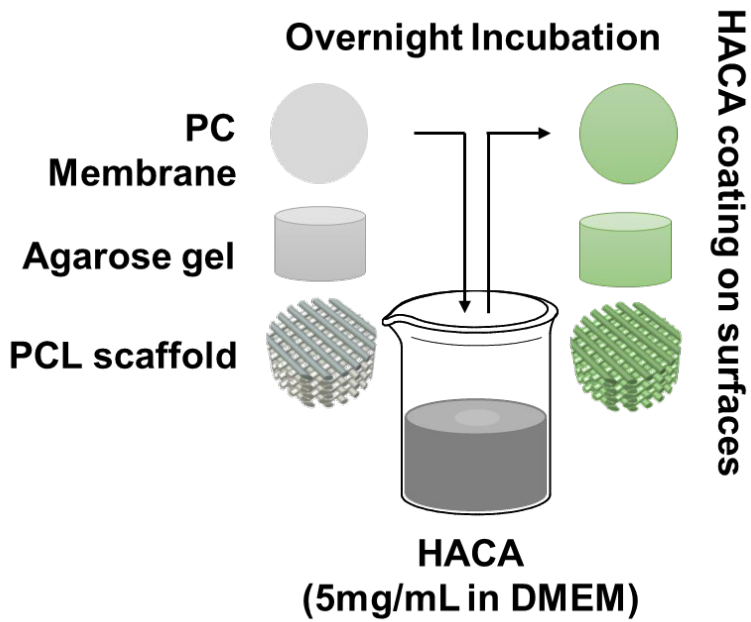


Figure 24. Schematic illustrations of adhesive HACA coating on the various substrates

Schematic illustrations of adhesive HACA coating on the various substrates (i.e. PC membrane, agarose hydrogel, 3D-printed PCL scaffold).

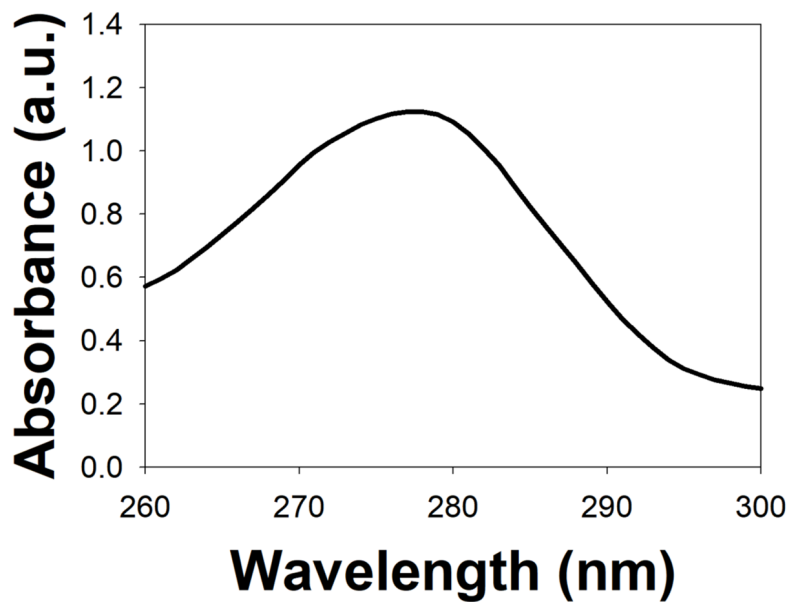


Figure 25. UV-Vis spectrum of HACA after 12 hr incubations.

	PC membrane	4% Agarose gel	PCL scaffold
Biodegradability	No	Yes	Yes
Surface stiffness for <i>in vitro</i> eSMG culture	Adequate under floating culture system	Too stiff	Too stiff
Hydrophobicity	High	Low	High
Mechanical Durability	Low	High	High
Used in this study to represent..	Classic culture model	Implantable hydrogel system with durability	Implantable polymeric scaffold with durability

Table 1. Properties and biocompatibility of Biomaterials tested in this study for *in vitro* eSMG culture

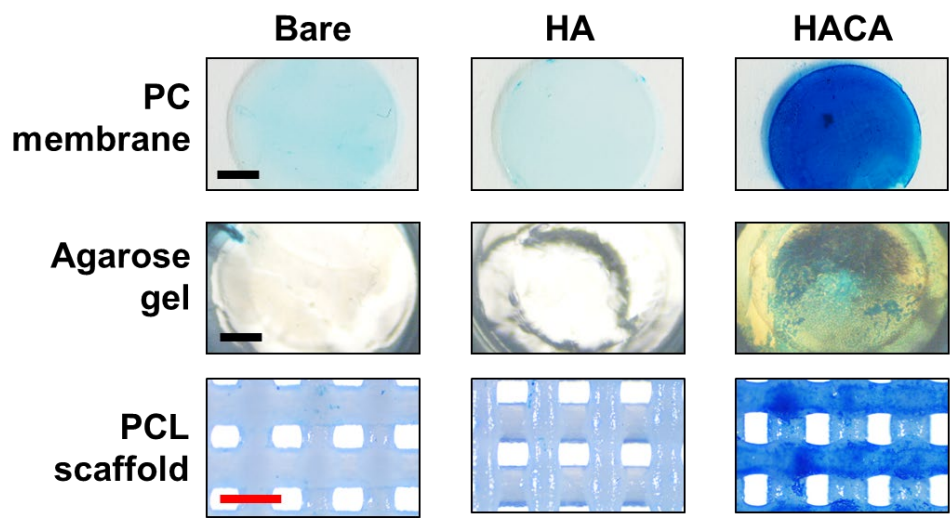


Figure 26. Alcian blue staining results from bare, HA, and HACA-coated materials

Photographic images of alcian blue-stained bare, HA or HACA-coated PC membranes, agarose gels, and PCL scaffolds. Black scale bar = 2.5 mm, red scale bar = 0.5 mm.

Average percentage (%)	PC membrane			4% Agarose gel			PCL scaffold		
	Bare	HA	HACA	Bare	HA	HACA	Bare	HA	HACA
Nitrogen	0.717 ±0.275	3.170 ±2.528	9.377 ±0.476	1.710 ±0.147	1.540 ±0.182	4.570 ±0.415	0.590 ±0.511	1.130 ±0.200	9.290 ±0.144
Oxygen	17.520 ±0.108	13.887 ±3.081	39.600 ±3.817	45.897 ±0.198	45.557 ±0.355	44.320 ±0.209	28.567 ±1.759	29.187 ±0.162	37.853 ±6.810
Carbon	81.767 ±0.381	82.936 ±0.553	51.023 ±4.227	52.396 ±0.150	52.903 ±0.185	51.103 ±0.245	70.843 ±2.091	69.676 ±0.111	52.856 ±6.870

Table 2. Atomic compositions of material surfaces

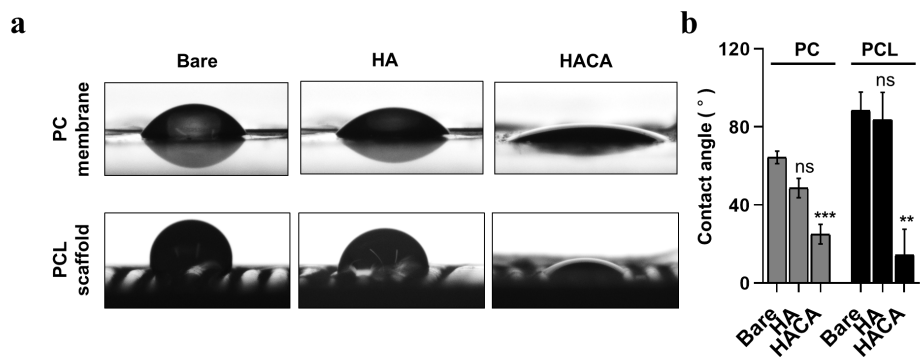


Figure 27. Water contact angle results from bare, HA, and HACA-coated materials

(a) Water contact angles of bare, HA, or HACA-coated PC membranes and PCL scaffolds (representative of three replicates). (b) Goniometric quantification of bare, HA, or HACA-coated PC membranes and PCL scaffolds (n=3). *: $p < 0.05$, **: $p < 0.01$, ***: $p < 0.005$.

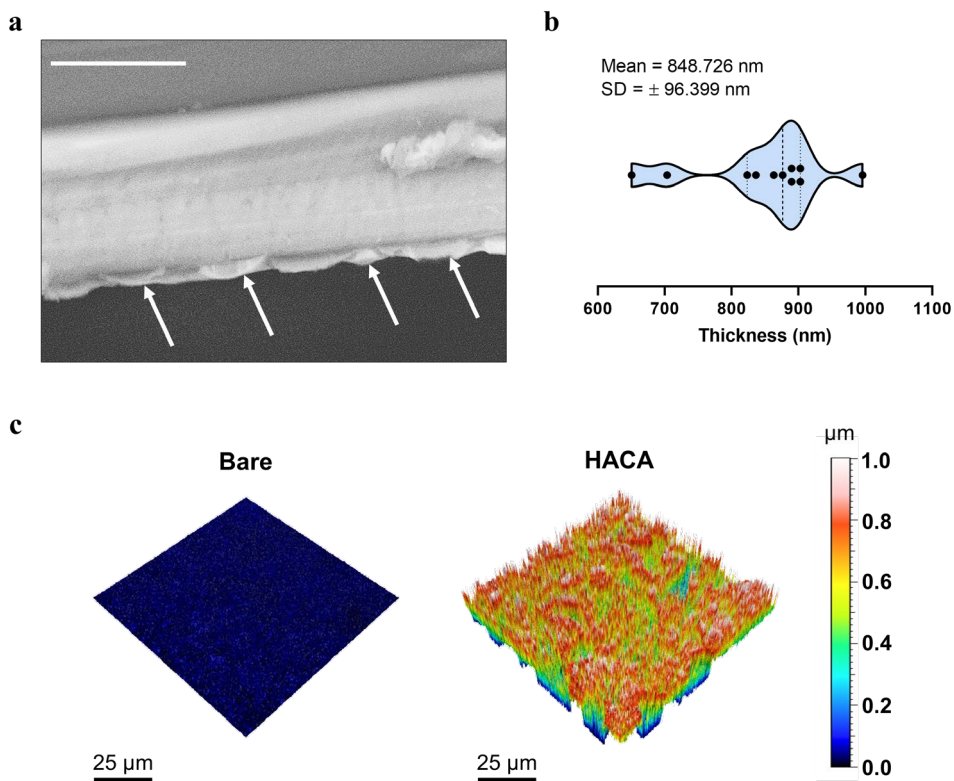


Figure 28. Thickness and surface topology of HACA-coated surfaces

(a) Cross-section of HACA-coated PC membrane is imaged by SEM. HACA coating layer is indicated with white arrow. Scale bar = 10 μm (b) Thickness of HACA coating layer are measured at 11 different points. (c) Surface topology of bare and HACA-coated PC membrane is quantified by confocal laser scanning microscope (Carl Zeiss, LSM800 for Materials) with 50 Z-stacks and visualized by 3D heat mapping.

Interaction between eSMG cells and HACA-coated surfaces

The aforementioned hypothesis is that ‘mimicking mesenchymal HA by HACA coating on a material surface will reproduce the interaction between HA and CD44+ eSMG cells. To test the hypothesis, I performed cell adhesion tests on HA and HACA-coated membrane surfaces with or without treatment with CD44-blocking anti-CD44 antibody (aCD44). I dissociated e13.5 eSMGs into single cells and incubated them on bare and HA, HACA-coated PC membranes for 12 hours. After a gentle washing, the remaining cells were imaged and quantified by CCK8 assay (**Figure 29a**). The results show an approximately 5.2 folds higher number of eSMG cells showing highly re-organized glandular morphology (**Figure 29b**, HACA) robustly bound on HACA-coated membrane compared to bare or HA-coated membranes (**Figure 29b** and **29c**). However, adhesion level of eSMG cells pre-incubated with aCD44s is significantly decreased to 2.4 folds, indicating a possibility that adhesion of eSMG cells on HACA-coated surfaces is mediated by HA-CD44 interaction (**Figure 29b** and **29c**).

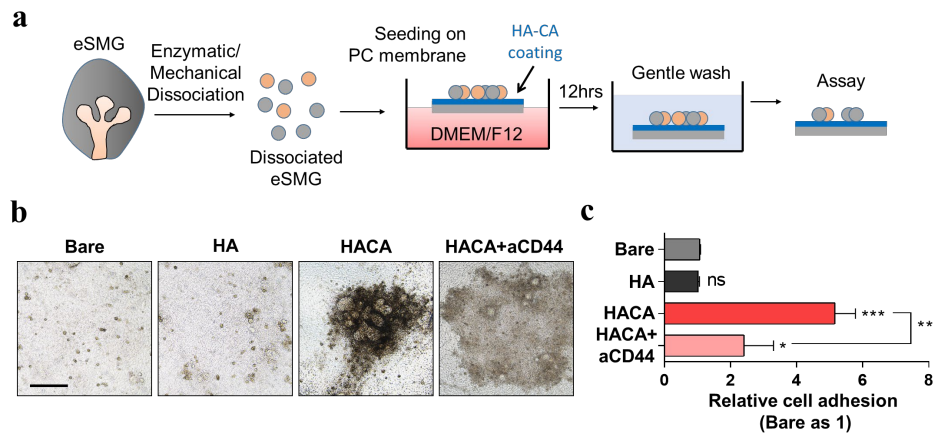


Figure 29. Interaction between eSMG cells and HACA-coated surfaces

(a) Schematic diagram of cell adhesion test using dissociated eSMGs. (b) Bright field image of adhered cells with or without treatment of anti-CD44 antibody on bare and HACA-coated PC membrane surfaces (representative of three replicates, scale bar = 200 μ m) (c) Relative degree of adhered cells is estimated by CCK8 assay (n=3).

*: $p < 0.05$, **: $p < 0.01$, ***: $p < 0.005$.

HA-rich mesenchyme-mimicking HACA coating improves surface property of various substrates for organotypic culture of eSMG

Figure 29 shows that the adhesive HACA coating which mimics the HA-rich mesenchyme enhanced cellular adhesion. However, to evaluate tissue engineering efficacy for culture of fully structured SGFUs, it is crucial to examine degree of the branching morphogenesis, a unique developmental process of eSMGs. To observe such branching morphogenesis on various substrates, I isolated eSMGs from e13 mouse fetus and then placed them on the HACA-coated substrates with air-media interface. This air-media interface culture on several types of substrates has been reported by previous studies (Miyajima et al. 2011; Ozdemir et al. 2016a; Yang and Young 2008), but none of those showed successful eSMG cultures showing degree of branching morphogenesis comparable to that *in vivo*. This is because the physicochemical and biological properties of such substrates are different from the *in vivo* microenvironment of eSMGs. For example, stiffness of substrate significantly affects branching morphogenesis of eSMGs (Miyajima et al. 2011; Peters et al. 2014; Sathi et al. 2017). eSMGs cannot grow and branch properly on stiff surfaces, but this negative effect is mitigated by fabricating surfaces with RGD sequence (Miyajima et al. 2011), supplementing transforming growth factor-beta 1 (Peters et al. 2014), or macrophage colony stimulating factor (Sathi et al. 2017). These results from the previous studies indicate that the physicochemical discrepancy between substrates used *in vitro* and those existing *in vivo* microenvironments can be overcome by introducing biologically active molecules originated from *in vivo* microenvironments. Thus, I hypothesized that a HACA

coating that mimics the HA-rich mesenchyme *in vivo* would achieve a similar or superior result.

To prove my hypothesis, I tested three types of substrate subjected to HACA coating: PC membrane, stiff agarose hydrogel, and PCL scaffold. Bare PC membrane is used in this study as a control, because an air-media interface culture system using floating PC membrane has been considered a classic method for *in vitro* eSMG culture (Sakai and Onodera 2008). Although it is the best culture method to this date, achieving the most similar degree of eSMG branching morphogenesis to that observed *in vivo*, eSMGs cultured in this condition still show significantly retarded branching compared to *in vivo* condition (Yang and Young 2008). Stiff agarose hydrogels are used to represent stiff and hydrophilic substrate. As the gel concentration is increased from 1% to 4%, its elastic modulus is also increased from 1.53 kPa to 17.5 kPa, and branching morphogenesis of eSMGs is significantly inhibited at 4% (**Figure 30a and 30b**). Therefore, 4% stiff agarose gel is used to test whether HACA coating is able to mitigate this negative effect of stiff surfaces on eSMG branching morphogenesis. Lastly, 3D-printed PCL scaffold was used to represent an example of commercially used biomaterials having both stiff and hydrophobic properties (**Figure 31a**).

To quantitatively evaluate the degree of *in vitro* branching morphogenesis, four parameters were used: Budding level based on bright field live imaging, apoptotic activity, vascular endothelial branching, and mitotic activity of c-kit⁺ progenitor cells after 48 hrs of *in vitro* culturing e13 eSMG, which is equivalent to e15 *in vivo*. In addition, to evaluate whether the functional SGFUs are successfully formed in fully developed eSMGs, the expression of AQP5, a functional acinar marker, and a-

SMA, a myoepithelial cell marker, were examined 120 hrs after *in vitro* culturing e13 eSMG, which is equivalent to postnatal 1 (P1) *in vivo*.

The average bud number of freshly isolated e15 eSMG was set as “budding level of 100%”. After 48 hrs of culturing e13 eSMGs on each substrate, bud number was manually counted and relatively expressed as budding level. In the conventional eSMG culture model, eSMGs cultured on bare PC membrane only reaches 50% full budding level, but those cultured on HACA-coated PC membrane show significantly enhanced branching morphogenesis, 78% of full budding level (**Figure 31b**). In the stiff agarose hydrogel culture model, eSMGs cultured on bare group show significantly attenuated branching morphogenesis, exhibiting only 17% of full budding level. However, eSMGs cultured on HACA-coated stiff hydrogel show significantly enhanced budding level (51% of full budding level) compared to bare group (**Figure 31b**). In 3D PCL scaffold culture model, eSMGs cultured on the bare substrate also show significantly attenuated branching morphogenesis with abnormal morphology, but those cultured on HACA-coated substrate show significantly improved branching morphogenesis, reaching up to 87% of full budding level (**Figure 31b**).

I thought that the attenuations of branching morphogenesis observed in stiff hydrogel and 3D PCL scaffold culture model were due to abnormally increased cellular apoptosis. According to the whole mount immunofluorescence staining data, there is no significant apoptosis in eSMGs cultured in conventional culture model, barely showing cleaved caspase 3 signals (**Figure 31c**, the first row). However, in stiff hydrogel and 3D PCL scaffold culture models, significantly increased apoptosis is detected in mesenchyme. Since mesenchyme encapsulates the epithelium in

eSMGs, it is the tissue directly affected by mechanical stiffness. Premature loss of mesenchyme via apoptosis might have caused the retardation of epithelium growth since mesenchyme produces numerous soluble and ECM-based growth cues for epithelium.³⁰ However, eSMGs cultured on either HACA-coated stiff hydrogel or 3D PCL scaffold show no such abnormal apoptosis in mesenchyme (**Figure 31c**, the first row).

Enlightened by the results from **Figure 21** and **22**, showing the intimate spatial co-localization between mesenchymal vasculature and HA-concentrated mesenchymal area, I speculated that HACA coating which mimics HA-rich environment would also enhance vascular branching. As expected, on all three of the substrates, eSMGs cultured on HACA-coated substrates result in improved vascular branching, showing significantly more complex vasculatures than those cultured on bare substrates (**Figure 31c**, the second row). Finally, the c-kit⁺ progenitor cell population and their mitotic activity were examined. In conventional culture model, eSMGs cultured on bare PC membrane show limited expression of c-kit and Ki-67⁺ cells mainly concentrated at the tip of buds (**Figure 31c**, the third row). However, buds of eSMGs cultured on HACA-coated PC membrane show significantly increased expression of c-kit and nuclear Ki-67, indicating a stronger proliferation activity (**Figure 31c**, the third row). In both stiff hydrogel and 3D PCL scaffold models, significantly reduced c-kit⁺ progenitor cell number and mitotic activities are observed compared to conventional culture model (**Figure 31c**, the third row), but when cultured on HACA-coated surfaces, c-kit⁺ progenitor cell populations and their mitotic activities are significantly restored up to the level of eSMGs cultured in the conventional condition (**Figure 31c**, the third row).

Finally, I examined whether the progenitor cells in eSMGs on HACA-coated substrates were properly differentiated into mature acinar (AQP5+) and myoepithelial cells (α -SMA). In conventional culture model, both bare and HACA-coated groups show fully branched morphology (**Figure 31d**, the first row) and well-differentiated acinar and myoepithelial cells, but AQP5 expression is stronger in HACA-coated groups (**Figure 31d**, the second row). In both stiff hydrogel and 3D PCL scaffold models, significant degeneration of epithelium morphology (**Figure 31d**, the first row) with decreased expression of AQP5 and no α -SMA expression is observed in eSMGs cultured on bare substrates (**Figure 31d**, the second row). However, eSMGs cultured on HACA-coated hydrogel and PCL scaffold show well-branched morphology (**Figure 31d**, the first row) with robust expression of both AQP5 and α -SMA (**Figure 31d**, the second row), indicating that the enhanced c-kit+ progenitor cell population in HACA coating groups has been successfully differentiated into acinar and myoepithelial cells.

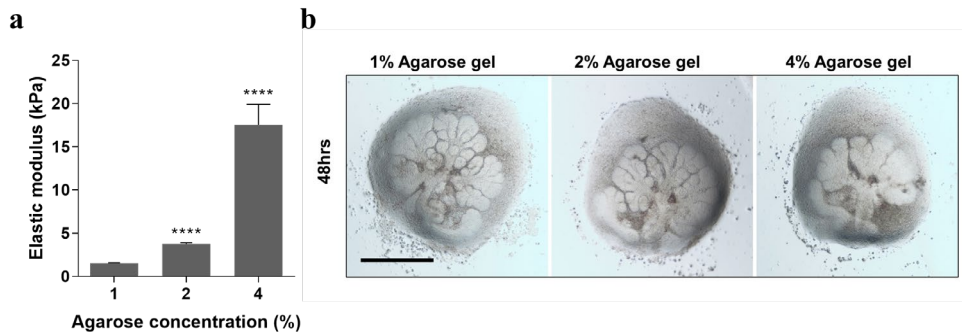


Figure 30. BM of eSMGs on alginate hydrogels of different stiffness

(a) Elastic modulus of 1%, 2%, and 4% agarose gel (n=21). **(b)** e13 eSMGs cultured on 1%, 2%, and 4% agarose gel for 48hrs (representative of four replicates, scale bar = 500 μ m). *: $p < 0.05$, **: $p < 0.01$, ***: $p < 0.005$

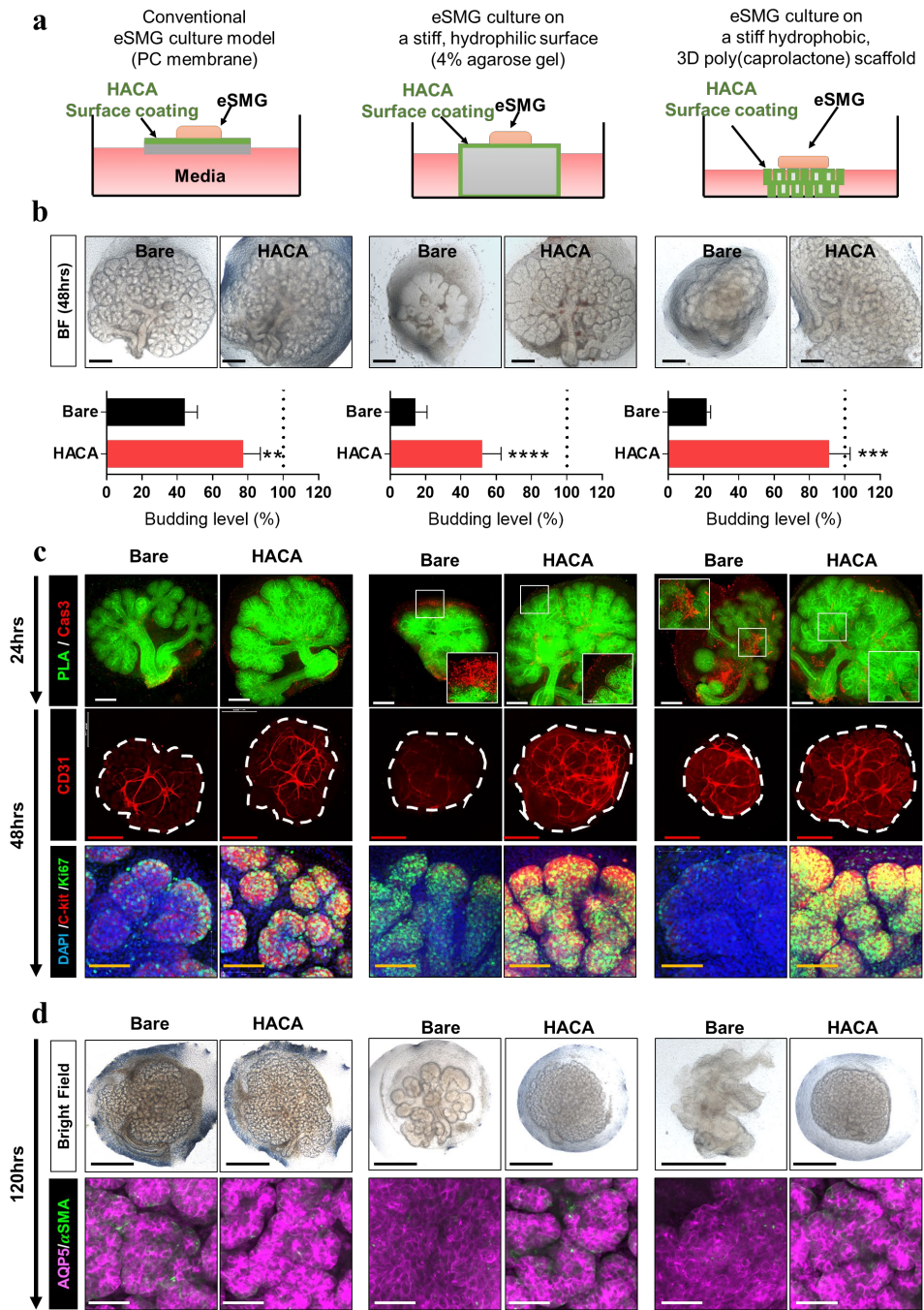


Figure 31. NiCHE coating platform enhances growth of eSMG on various substrates.

(a) Schematic illustration of culture of eSMGs on HACA-coated PC membrane, stiff 4% agarose gel, and 3D-printed PCL scaffold. **(b)** Bright field images and budding levels of eSMGs cultured either on bare or HACA-coated materials after 48 hr-culture. Average bud count of eSMGs freshly isolated from TP15 mouse fetus is considered as 100 %. Scale bar = 200 μm . **(c)** Apoptotic activity, VE structure, and mitotic activity of progenitor cell of eSMGs cultured either on bare or HACA-coated materials after 24 and 48 hr-culture respectively. White scale bar = 200 μm , Red scale bar = 500 μm , Yellow scale bar = 100 μm . **(d)** Bright field images and AQP5/a-SMA expressions of eSMGs cultured either on bare or HACA-coated materials after 120 hr-culture (black scale bar = 500 μm , white scale bar = 50 μm). Each image is representative of four replicates. *: $p < 0.05$, **: $p < 0.01$, ***: $p < 0.005$, Images in each corresponding group were equally enhanced in PowerPoint to provide better visual clarity.

Increased vascular endothelial cell proliferation by HACA coating is crucial for enhancement of branching morphogenesis

Figure 31 proved that my hypothesis, that HACA coating which mimics HA-rich area in eSMG mesenchyme would enhance branching morphogenesis of eSMG *in vitro*, was correct. Next, I questioned what biological mechanism is involved in HACA coating-mediated enhancement of branching morphogenesis. Based on the results from **Figure 22** and **Figure 31**, I hypothesized that an improved vascularization is the key explanation. In fact, vascular endothelial cells in eSMGs are crucial for branching morphogenesis since they secrete soluble growth factors such as Insulin-like growth factor binding protein-3 to stimulate proliferation of c-kit⁺ progenitor cells (Kwon et al. 2017).

To prove my hypothesis, I first quantitatively confirm that HACA coating enhances branching of vascular endothelial cells. According to the fractal dimension (FD) analysis based on binary image of CD31⁺ vascular endothelial cell staining, more complex and extensively-branched vascular structures are observed on HACA-coated PC membranes (FD = 1.637) compared to bare ones (FD = 1.188) (**Figure 32a** and **32b**). Numerous previous studies which report that immobilized HA can enhance endothelial cell attachment and proliferation via CD44s also strongly support this result (Xue et al. 2017).

Second, I examined whether this enhanced endothelial branching was due to direct interaction or indirect stimulation via soluble factors. The Z-axis of a whole mount eSMG was subdivided into four sections, from the bottom side contacting the membrane (section D in **Figure 32c**) to the top side (section A in **Figure 32c**). Within these four z-sections, CD31 immuno-fluorescence signals of bare and HACA-coated

membranes are visualized in **Figure 32d**. CD31 signals of eSMGs cultured on bare PC membrane are located at the middle of the whole eSMG, but those of eSMGs cultured on HACA-coated PC membrane are mainly concentrated at the bottom side (Section D). Quantified CD31 signal data in Figure 4e also show a similar result: eSMGs on control PC membrane show no significant difference in average intensity of CD31 within the four sections, but in HACA-coated membrane group, significantly higher CD31 signal is detected at section D, directly on the HACA-coated interface, compared to section A (**Figure 32e**). Furthermore, on section D, phosphorylated extracellular signal-regulated kinase (pERK) signal, one of the proliferation cues for endothelial cells (Joo et al. 2016; Mavria et al. 2006; Wu et al. 2016), is more extensively activated in eSMGs cultured on HACA-coated membranes (**Figure 32f**).

Lastly, the contribution of vascular endothelial cells on the HACA coating-mediated enhancement of branching morphogenesis was evaluated. eSMG were cultured on either bare or HACA-coated PC membrane with or without supplementing ZM323881, a VEGFR2 inhibitor to specifically deplete VE cells. Treatment of ZM323881 on eSMGs in bare group shows only a marginal but significant attenuation of both branching morphogenesis and c-kit⁺ progenitor cell population compared to those in ZM323881-untreated bare group, indicating a possibility of compensatory action replacing a role of vascular endothelial cells (**Figure 32g – 32i**). In HACA groups, when vascular endothelial cell proliferation is specifically blocked by ZM323881, branching morphogenesis enhancement effect with increased number of c-kit⁺ progenitor cells in HACA group is disappeared and rolled back to the level of bare group (**Figure 32g – 32i**). Since radiation-induced

microvascular damage is one of the major contributing factors for radiation-induced Xerostomia (Mizrachi et al. 2016), this angiogenic potential of HACA coating will be useful not only for *in vitro* tissue culture of salivary glands but also for directly promoting regeneration of damaged salivary glands *in vivo*. Therefore, it is expected that the HACA films or HACA composite materials without delivering *in vitro*-cultured tissues can also be applicable for salivary gland regeneration by attaching those materials to damaged tissues. In addition, establishment of NiCHE platform supported by HACA coating is easily achievable on various types of biomaterials with simple procedure, thus it can be ubiquitously applied to regeneration and tissue engineering of other epithelial organs such as intestine, lung, and kidney. Although my observations clearly demonstrate the effectiveness of NiCHE platform in eSMG cultures, it is still necessary to thoroughly examine the optimization of coating and culture methods, transplantation procedures, and biocompatibility and biodegradability *in vivo* for the further clinical applications.

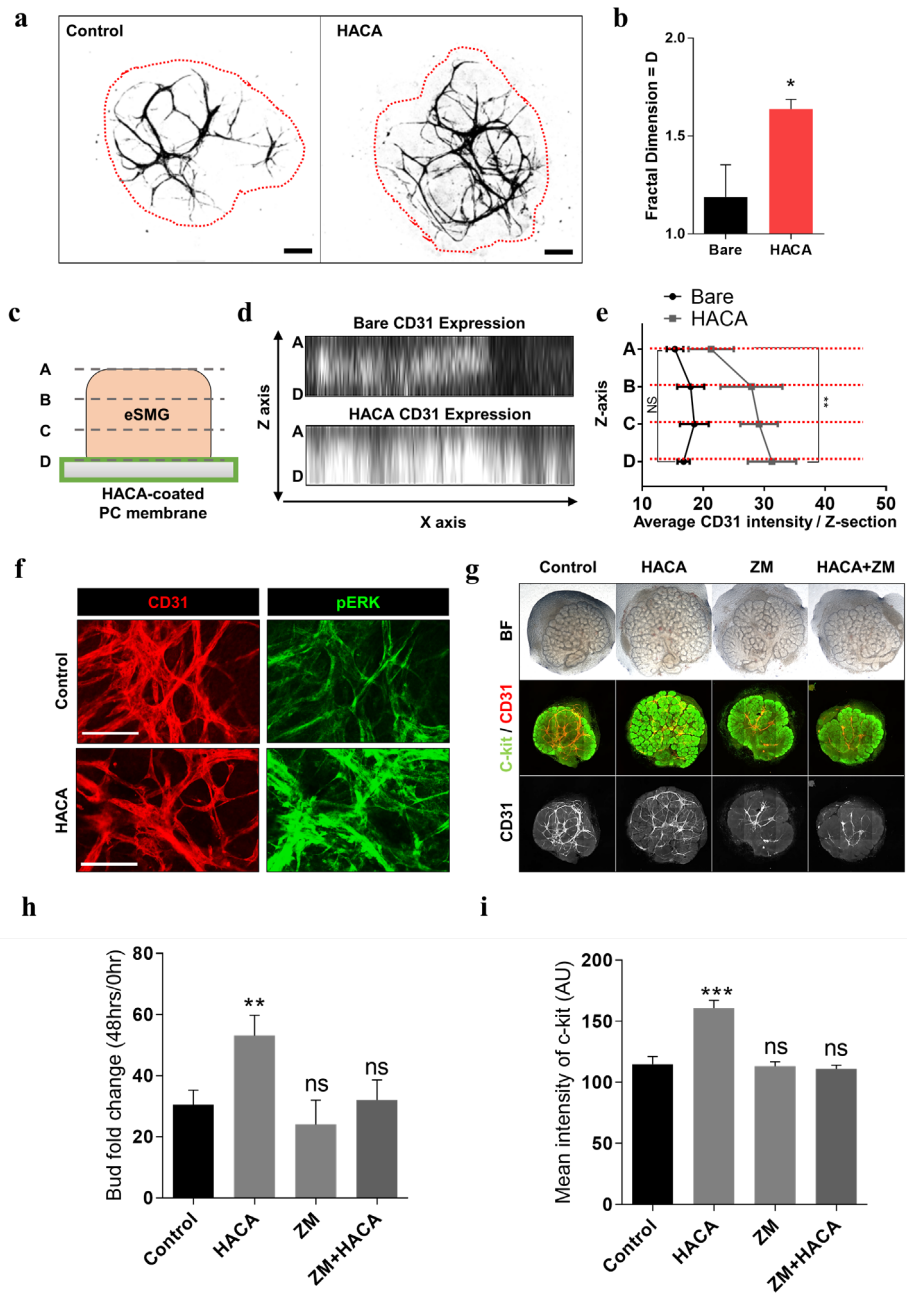


Figure 32. Local enhancement of vascular endothelial (VE) cell proliferation by NiCHE coating platform.

(a) Binary images of CD31+ VE structure within eSMGs. Scale bar = 200 μ m. Outline of each eSMG is marked with red-dotted line (Representative of four

replicates). **(b)** Fractal Dimension (FD) analysis of VE structure based on Figure 4a (n = 4). **(c)** VE cells in whole eSMGs are stained with CD31 antibody and captured at four different Z-levels. From the top of eSMG (indicated as A) to the bottom of eSMG (indicated as D), contacting either bare or HACA-coated PC membrane. **(d)** Intensity of CD31 in four different Z-levels is visualized (representative of four replicates). **(e)** Average intensity of CD31 of each Z-level is quantified. (n = 4). **(f)** pERK activity of VE cells. (representative of three replicates, scale bar = 100 μ m). **(g)** Effect of VE cell proliferation on branching morphogenesis of eSMG and c-kit⁺ progenitor cell population (representative of four replicates). **(h)** Bud fold change (number of buds at 48 hrs / number of buds at 0 hr) of Control, HACA, ZM, and ZM+HACA groups (n = 4). **(i)** Mean intensity of c-kit of whole-mount immunofluorescence images of Control, HACA, ZM, and ZM+HACA groups (n = 4). *: p < 0.05, **: p < 0.01, ***: p < 0.005. Images in each corresponding group were equally enhanced in PowerPoint to provide better visual clarity.

Conclusion

In chapter I, I revealed the role of HA in salivary gland organogenesis and organ germ formation by monitoring effects of HA in *in vitro* eSMG culture models. I found that the highly proliferative c-Kit⁺ cells of branching eSMG are located at the periphery of epithelial buds, which directly contacts the highly dense stratum of HA in the mesenchyme. In addition, I show that the highly proliferative c-Kit⁺ cells at the periphery expressed CD44, an HA receptor. The perturbation of endogenous HA production, enzymatic HA destruction, or blocking of CD44 significantly inhibited both branching morphogenesis and self-organization of eSMG. Furthermore, I found that only HMW HA was effective in the maintaining the c-Kit⁺ cell population during salivary gland organogenesis (low-molecular-weight HA was not). For the tissue engineering application, the HMW HA was added into the media or immobilized on the substrates. Both HMW HA in solution and HMW HA immobilized on substrate could enhance organ germ formation, but the enhancement was significantly stronger in the immobilized groups. It is expected that HA-based biomaterials can be usefully exploited for regeneration of damaged salivary gland tissues (**Figure 33**).

In chapter II, I have developed a simple and ubiquitous NiCHE platform using material-independent HACA surface coating chemistry for salivary tissue engineering. By using eSMG culture models, I prove that the HACA coatings on the various substrates (i.e., polycarbonate membranes, agarose gels, and polycaprolactone scaffolds) are able to overcome the current challenges of *in vitro*

SGFU culture by 1) masking negative physicochemical properties of various material surfaces and 2) enhancing direct interactions between CD44 and hyaluronic acid to improve the proliferation of progenitor cell population with enhanced vascularization (**Figure 34**). Thus, NiCHE platform has enormous potential as an effective biomaterial in salivary tissue engineering.

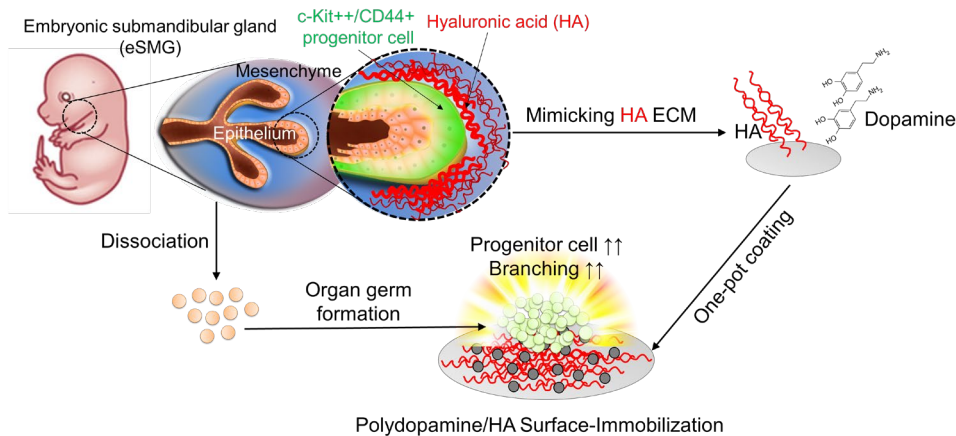


Figure 33. Schematic summary of chapter I

In chapter I, I characterized the effects of hyaluronic acid of different molecular weights and presentation forms (either solubilized or surface-immobilized form) on branching morphogenesis and organ germ formation of intact and dissociated embryonic salivary glands. Surface-immobilized high-molecular-weight hyaluronic acid by hyaluronic acid/polydopamine coating was found to be the most powerful enhancer for *in vitro* production of salivary gland organ germ by increasing the c-Kit⁺ embryonic progenitor cell population. Since these *in vitro*-generated salivary gland organ germs can be transplanted to regenerate damaged salivary glands, my findings are significant for advances in salivary gland tissue engineering.

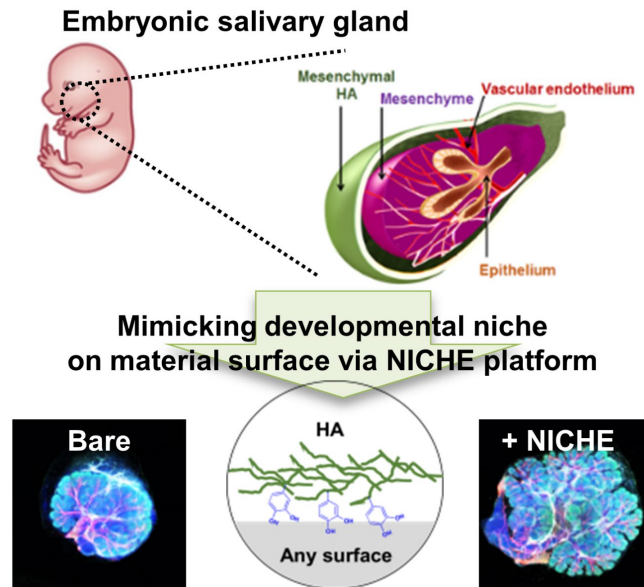


Figure 34. Schematic summary of chapter II

I synthesized hyaluronic acid–catechol (HACA) conjugates to establish a versatile hyaluronic acid coating platform named “NiCHE (nature-inspired catechol-conjugated hyaluronic acid environment)” for boosting the salivary gland tissue engineering efficacy of the previously reported biomaterials. By mimicking hyaluronic acid-rich niche in the mesenchyme of embryonic submandibular glands (eSMGs) with NiCHE coating on substrates including polycarbonate membrane, stiff agarose hydrogel, and polycaprolactone scaffold, significantly enhanced cell adhesion, vascular endothelial and progenitor cell proliferation, and branching of *in vitro*-cultured eSMGs were observed. High mechanical stiffness of the substrate is known to inhibit eSMG growth, but the NiCHE coating significantly reduced such stiffness-induced negative effects, leading to successful differentiation of progenitor cells to functional acinar and myoepithelial cells.

References

- Avigdor A, Goichberg P, Shivtiel S, Dar A, Peled A, Samira S, Kollet O, Hershkovitz R, Alon R, Hardan I. 2004. Cd44 and hyaluronic acid cooperate with sdf-1 in the trafficking of human cd34+ stem/progenitor cells to bone marrow. *Blood*. 103(8):2981-2989.
- Baker OJ, Schulz DJ, Camden JM, Liao Z, Peterson TS, Seye CI, Petris MJ, Weisman GA. 2010. Rat parotid gland cell differentiation in three-dimensional culture. *Tissue Engineering Part C: Methods*. 16(5):1135-1144.
- Bernfield M. 1977. The basal lamina in epithelial-mesenchymal morphogenetic interactions. *Upsala journal of medical sciences*. 82(2):111-112.
- Bernfield MR, Banerjee SD. 1972. Acid mucopolysaccharide (glycosaminoglycan) at the epithelial-mesenchymal interface of mouse embryo salivary glands. *The Journal of cell biology*. 52(3):664-673.
- Borghese E. 1950. The development in vitro of the submandibular and sublingual glands of mus musculus. *Journal of anatomy*. 84(Pt 3):287.
- Burlage FR, Faber H, Kampinga HH, Langendijk JA, Vissink A, Coppes RP. 2009. Enhanced proliferation of acinar and progenitor cells by prophylactic pilocarpine treatment underlies the observed amelioration of radiation injury to parotid glands. *Radiotherapy Oncology*. 90(2):253-256.
- Camenisch TD, Spicer AP, Brehm-Gibson T, Biesterfeldt J, Augustine ML, Calabro A, Kubalak S, Klewer SE, McDonald JA. 2000. Disruption of hyaluronan synthase-2 abrogates normal cardiac morphogenesis and hyaluronan-mediated transformation of epithelium to mesenchyme. *The Journal of clinical investigation*. 106(3):349-360.
- Chambers MS, Garden AS, Kies MS, Martin JW. 2004. Radiation-induced xerostomia in patients with head and neck cancer: Pathogenesis, impact on quality of life, and management. *Head & Neck: Journal for the Sciences Specialties of the Head Neck*. 26(9):796-807.
- Chambers MS, Rosenthal DI, Weber RS. 2007. Radiation-induced xerostomia. *Head & Neck: Journal for the Sciences Specialties of the Head Neck*. 29(1):58-63.
- Chen P-Y, Huang LL, Hsieh H-J. 2007. Hyaluronan preserves the proliferation and differentiation potentials of long-term cultured murine adipose-derived stromal cells. *Biochemical biophysical research communications*. 360(1):1-6.
- Costantini F, Kopan R. 2010. Patterning a complex organ: Branching morphogenesis and nephron segmentation in kidney development. *Developmental cell*. 18(5):698-712.
- Craig EA, Parker P, Austin AF, Barnett JV, Camenisch TD. 2010. Involvement of the mekk1 signaling pathway in the regulation of epicardial cell behavior by hyaluronan. *Cellular signalling*. 22(6):968-976.
- Cutler L. 1990. The role of extracellular matrix in the morphogenesis and differentiation of salivary glands. *Advances in dental research*. 4(1):27-33.

- Dirix P, Nuyts S, Van den Bogaert W. 2006. Radiation-induced xerostomia in patients with head and neck cancer: A literature review. *Cancer: Interdisciplinary International Journal of the American Cancer Society*. 107(11):2525-2534.
- Filisetti-Cozzi TM, Carpita NC. 1991. Measurement of uronic acids without interference from neutral sugars. *Analytical biochemistry*. 197(1):157-162.
- Fraser JRE, Laurent TC, Laurent U. 1997. Hyaluronan: Its nature, distribution, functions and turnover. *Journal of internal medicine*. 242(1):27-33.
- Fuchs K, Hippe A, Schmaus A, Homey B, Sleeman J, Orian-Rousseau V. 2013. Opposing effects of high-and low-molecular weight hyaluronan on cxcl12-induced cxcr4 signaling depend on cd44. *Cell death & disease*. 4(10):e819-e819.
- Fujita S, Ikeda T. 2012. Cancer stem-like cells in adenoid cystic carcinoma of salivary glands: Relationship with morphogenesis of histological variants. *Journal of oral pathology and medicine*. 41(3):207-213.
- Gakunga P, Frost G, Shuster S, Cunha G, Formby B, Stern R. 1997. Hyaluronan is a prerequisite for ductal branching morphogenesis. *Development*. 124(20):3987-3997.
- Ghezzi E, Ship J. 2003. Aging and secretory reserve capacity of major salivary glands. *Journal of dental research*. 82(10):844-848.
- Girard N, Delpech A, Delpech B. 1986. Characterization of hyaluronic acid on tissue sections with hyaluronectin. *Journal of Histochemistry Cytochemistry*. 34(4):539-541.
- Gornitsky M, Shenouda G, Sultanem K, Katz H, Hier M, Black M, Velly AM. 2004. Double-blind randomized, placebo-controlled study of pilocarpine to salvage salivary gland function during radiotherapy of patients with head and neck cancer. *Oral Surgery, Oral Medicine, Oral Pathology, and Oral Radiology*. 98(1):45-52.
- Grossfeld H. 1957. Production of hyaluronic acid in tissue culture by fibroblasts growing from intestinal, stomach, liver and kidney explants. *Proceedings of the Society for Experimental Biology Medicine*. 96(1):144-147.
- Guggenheimer J, Moore PA. 2003. Xerostomia: Etiology, recognition and treatment. *The Journal of the American Dental Association*. 134(1):61-69.
- Harunaga J, Hsu J, Yamada K. 2011. Dynamics of salivary gland morphogenesis. *Journal of dental research*. 90(9):1070-1077.
- Horowitz A, Simons M. 2008. Branching morphogenesis. *Circulation research*. 103(8):784-795.
- Hsiao Y-C, Lee H-W, Chen Y-T, Young T-H, Yang T-L. 2011. The impact of compositional topography of amniotic membrane scaffold on tissue morphogenesis of salivary gland. *Biomaterials*. 32(19):4424-4432.
- Humphrey SP, Williamson RT. 2001. A review of saliva: Normal composition, flow, and function. *The Journal of prosthetic dentistry*. 85(2):162-169.
- Hynes WL, Walton SL. 2000. Hyaluronidases of gram-positive bacteria. *FEMS microbiology letters*. 183(2):201-207.
- Ikeda E, Morita R, Nakao K, Ishida K, Nakamura T, Takano-Yamamoto T, Ogawa M, Mizuno M, Kasugai S, Tsuji T. 2009. Fully functional bioengineered tooth replacement as an organ replacement therapy. *Proceedings of the National Academy of Sciences*. 106(32):13475-13480.

- Imberti B, Seliktar D, Nerem R, Remuzzi A. 2002. The response of endothelial cells to fluid shear stress using a co-culture model of the arterial wall. *Endothelium*. 9(1):11-23.
- Inoue M, Katakami C. 1993. The effect of hyaluronic acid on corneal epithelial cell proliferation. *Investigative ophthalmology visual science*. 34(7):2313-2315.
- Itano N, Sawai T, Yoshida M, Lenas P, Yamada Y, Imagawa M, Shinomura T, Hamaguchi M, Yoshida Y, Ohnuki Y. 1999. Three isoforms of mammalian hyaluronan synthases have distinct enzymatic properties. *Journal of Biological Chemistry*. 274(35):25085-25092.
- Jacob RF, Weber RS, King GE. 1996. Whole salivary flow rates following submandibular gland resection. *Head Neck: Journal for the Sciences Specialties of the Head Neck*. 18(3):242-247.
- Jaskoll T, Abichaker G, Witcher D, Sala FG, Bellusci S, Hajihosseini MK, Melnick M. 2005. Fgf10/fgfr2b signaling plays essential roles during in vivo embryonic submandibular salivary gland morphogenesis. *BMC developmental biology*. 5(1):1-12.
- Jemal A, Siegel R, Ward E, Hao Y, Xu J, Thun MJ. 2009. Cancer statistics, 2009. *CA: a cancer journal for clinicians*. 59(4):225-249.
- Joo H, Byun E, Lee M, Hong Y, Lee H, Kim P. 2016. Biofunctionalization via flow shear stress resistant adhesive polysaccharide, hyaluronic acid-catechol, for enhanced in vitro endothelialization. *Journal of Industrial Engineering Chemistry*. 34:14-20.
- Kakizaki I, Kojima K, Takagaki K, Endo M, Kannagi R, Ito M, Maruo Y, Sato H, Yasuda T, Mita S. 2004. A novel mechanism for the inhibition of hyaluronan biosynthesis by 4-methylumbelliferone. *Journal of Biological Chemistry*. 279(32):33281-33289.
- Kang SM, Hwang NS, Yeom J, Park SY, Messersmith PB, Choi IS, Langer R, Anderson DG, Lee H. 2012. One-step multipurpose surface functionalization by adhesive catecholamine. *Advanced functional materials*. 22(14):2949-2955.
- Kashimata M, Sayeed S, Ka A, Onetti-Muda A, Sakagami H, Faraggiana T, Gresik EW. 2000. The erk-1/2 signaling pathway is involved in the stimulation of branching morphogenesis of fetal mouse submandibular glands by egf. *Developmental biology*. 220(2):183-196.
- Khaing ZZ, Seidlits SK. 2015. Hyaluronic acid and neural stem cells: Implications for biomaterial design. *Journal of Materials Chemistry B*. 3(40):7850-7866.
- Kim S, Jang Y, Jang LK, Sunwoo SH, Kim T-i, Cho S-W, Lee JY. 2017. Electrochemical deposition of dopamine-hyaluronic acid conjugates for anti-biofouling bioelectrodes. *Journal of Materials Chemistry B*. 5(23):4507-4513.
- Kleinman HK, Philp D, Hoffman MP. 2003. Role of the extracellular matrix in morphogenesis. *Current opinion in biotechnology*. 14(5):526-532.
- Knox SM, Lombaert IM, Haddox CL, Abrams SR, Cotrim A, Wilson AJ, Hoffman MP. 2013. Parasympathetic stimulation improves epithelial organ regeneration. *Nature communications*. 4(1):1-7.

- Kultti A, Pasonen-Seppänen S, Jauhiainen M, Rilla KJ, Kärnä R, Pyöriä E, Tammi RH, Tammi MI. 2009. 4-methylumbelliferone inhibits hyaluronan synthesis by depletion of cellular udp-glucuronic acid and downregulation of hyaluronan synthase 2 and 3. *Experimental cell research*. 315(11):1914-1923.
- Kwak M, Ninche N, Klein S, Saur D, Ghazizadeh S. 2018. C-kit+ cells in adult salivary glands do not function as tissue stem cells. *Scientific reports*. 8(1):1-11.
- Kwon HR, Nelson DA, DeSantis KA, Morrissey JM, Larsen M. 2017. Endothelial cell regulation of salivary gland epithelial patterning. *Development*. 144(2):211-220.
- Larsen M, Wei C, Yamada KM. 2006. Cell and fibronectin dynamics during branching morphogenesis. *Journal of cell science*. 119(16):3376-3384.
- Lee S-w, Kim J, Do M, Namkoong E, Lee H, Ryu JH, Park K. 2020a. Developmental role of hyaluronic acid and its application in salivary gland tissue engineering. *Acta Biomaterialia*. 115:275-287.
- Lee S-w, Ryu JH, Do MJ, Namkoong E, Lee H, Park K. 2020b. Niche platform: Nature-inspired catechol-conjugated hyaluronic acid environment platform for salivary gland tissue engineering. *ACS Applied Materials & Interfaces*. 12(4):4285-4294.
- Lih E, Choi SG, Ahn DJ, Joung YK, Han DK. 2016. Optimal conjugation of catechol group onto hyaluronic acid in coronary stent substrate coating for the prevention of restenosis. *Journal of tissue engineering*. 7:2041731416683745.
- Lombaert I, Movahednia MM, Adine C, Ferreira JN. 2017. Concise review: Salivary gland regeneration: Therapeutic approaches from stem cells to tissue organoids. *Stem Cells*. 35(1):97-105.
- Lombaert IM, Abrams SR, Li L, Eswarakumar VP, Sethi AJ, Witt RL, Hoffman MP. 2013. Combined kit and fgfr2b signaling regulates epithelial progenitor expansion during organogenesis. *Stem cell reports*. 1(6):604-619.
- Lu P, Werb Z. 2008. Patterning mechanisms of branched organs. *Science*. 322(5907):1506-1509.
- Maharjan AS, Pilling D, Gomer RH. 2011. High and low molecular weight hyaluronic acid differentially regulate human fibrocyte differentiation. *PloS one*. 6(10):e26078.
- Maimets M, Rocchi C, Bron R, Pringle S, Kuipers J, Giepmans BN, Vries RG, Clevers H, De Haan G, Van Os R. 2016. Long-term in vitro expansion of salivary gland stem cells driven by wnt signals. *Stem cell reports*. 6(1):150-162.
- Mandel ID. 1989. The role of saliva in maintaining oral homeostasis. *The Journal of the American Dental Association*. 119(2):298-304.
- Mavria G, Vercoulen Y, Yeo M, Paterson H, Karasarides M, Marais R, Bird D, Marshall CJ. 2006. Erk-mapk signaling opposes rho-kinase to promote endothelial cell survival and sprouting during angiogenesis. *Cancer cell*. 9(1):33-44.
- May AJ, Cruz-Pacheco N, Emmerson E, Gaylord EA, Seidel K, Nathan S, Muench MO, Klein OD, Knox SM. 2018. Diverse progenitor cells preserve salivary

- gland ductal architecture after radiation-induced damage. *Development*. 145(21).
- Misra S, Hascall VC, Markwald RR, Ghatak S. 2015. Interactions between hyaluronan and its receptors (cd44, rhamm) regulate the activities of inflammation and cancer. *Frontiers in immunology*. 6:201.
- Miyajima H, Matsumoto T, Sakai T, Yamaguchi S, An SH, Abe M, Wakisaka S, Lee KY, Egusa H, Imazato S. 2011. Hydrogel-based biomimetic environment for in vitro modulation of branching morphogenesis. *Biomaterials*. 32(28):6754-6763.
- Mizrachi A, Cotrim AP, Katabi N, Mitchell JB, Verheij M, Haimovitz-Friedman A. 2016. Radiation-induced microvascular injury as a mechanism of salivary gland hypofunction and potential target for radioprotectors. *Radiation research*. 186(2):189-195.
- Morita K, Nogawa H. 1999. Egf-dependent lobule formation and fgf7-dependent stalk elongation in branching morphogenesis of mouse salivary epithelium in vitro. *Developmental dynamics*. 215(2):148-154.
- Morrison H, Sherman LS, Legg J, Banine F, Isacke C, Haipok CA, Gutmann DH, Ponta H, Herrlich P. 2001. The nf2 tumor suppressor gene product, merlin, mediates contact inhibition of growth through interactions with cd44. *Genes development*. 15(8):968-980.
- Musselmann K, Green J, Sone K, Hsu J, Bothwell I, Johnson S, Harunaga J, Wei Z, Yamada K. 2011. Salivary gland gene expression atlas identifies a new regulator of branching morphogenesis. *Journal of dental research*. 90(9):1078-1084.
- Nakao K, Morita R, Saji Y, Ishida K, Tomita Y, Ogawa M, Saitoh M, Tomooka Y, Tsuji T. 2007. The development of a bioengineered organ germ method. *Nature methods*. 4(3):227-230.
- Naor D, Nedvetzki S, Golan I, Melnik L, Faitelson Y. 2002. Cd44 in cancer. *Critical reviews in clinical laboratory sciences*. 39(6):527-579.
- Nederfors T. 2000. Xerostomia and hyposalivation. *Advances in dental research*. 14(1):48-56.
- Nelson DA, Manhardt C, Kamath V, Sui Y, Santamaria-Pang A, Can A, Bello M, Corwin A, Dinn SR, Lazare M. 2013. Quantitative single cell analysis of cell population dynamics during submandibular salivary gland development and differentiation. *Biology open*. 2(5):439-447.
- Ogawa M, Oshima M, Imamura A, Sekine Y, Ishida K, Yamashita K, Nakajima K, Hirayama M, Tachikawa T, Tsuji T. 2013. Functional salivary gland regeneration by transplantation of a bioengineered organ germ. *Nature communications*. 4(1):1-10.
- Ohya T, Kaneko Y. 1970. Novel hyaluronidase from streptomyces. *Biochimica et Biophysica Acta -Enzymology*. 198(3):607-609.
- Okumura K, Shinohara M, Endo F. 2012. Capability of tissue stem cells to organize into salivary rudiments. *Stem cells international*. 2012.
- Ozdemir T, Fowler EW, Hao Y, Ravikrishnan A, Harrington DA, Witt RL, Farach-Carson MC, Pradhan-Bhatt S, Jia X. 2016a. Biomaterials-based strategies for salivary gland tissue regeneration. *Biomaterials science*. 4(4):592-604.
- Ozdemir T, Fowler EW, Liu S, Harrington DA, Witt RL, Farach-Carson MC, Pradhan-Bhatt S, Jia X. 2016b. Tuning hydrogel properties to promote the

- assembly of salivary gland spheroids in 3d. *ACS biomaterials science engineering*. 2(12):2217-2230.
- Patel VN, Hoffman MP. 2014. Salivary gland development: A template for regeneration. *Seminars in cell & developmental biology*. 25:52-60.
- Patel VN, Knox SM, Likar KM, Lathrop CA, Hossain R, Eftekhari S, Whitelock JM, Elkin M, Vlodaysky I, Hoffman MP. 2007. Heparanase cleavage of perlecan heparan sulfate modulates fgf10 activity during ex vivo submandibular gland branching morphogenesis. *Development*. 134(23):4177-4186.
- Patel VN, Rebutini IT, Hoffman MP. 2006. Salivary gland branching morphogenesis. *Differentiation*. 74(7):349-364.
- Peters SB, Naim N, Nelson DA, Mosier AP, Cady NC, Larsen M. 2014. Biocompatible tissue scaffold compliance promotes salivary gland morphogenesis and differentiation. *Tissue Engineering Part A*. 20(11-12):1632-1642.
- Pinna R, Campus G, Cumbo E, Mura I, Milia E. 2015. Xerostomia induced by radiotherapy: An overview of the physiopathology, clinical evidence, and management of the oral damage. *Therapeutics clinical risk management*. 11:171.
- Pohl M, Sakurai H, Stuart RO, Nigam SK. 2000. Role of hyaluronan and cd44 in in vitro branching morphogenesis of ureteric bud cells. *Developmental biology*. 224(2):312-325.
- Pradhan-Bhatt S, Harrington DA, Duncan RL, Jia X, Witt RL, Farach-Carson MC. 2013. Implantable three-dimensional salivary spheroid assemblies demonstrate fluid and protein secretory responses to neurotransmitters. *Tissue engineering Part A*. 19(13-14):1610-1620.
- Pradhan S, Liu C, Zhang C, Jia X, Farach-Carson MC, Witt RL. 2010. Lumen formation in three-dimensional cultures of salivary acinar cells. *Otolaryngology—Head Neck Surgery*. 142(2):191-195.
- Pringle S, Maimets M, van der Zwaag M, Stokman MA, van Gosliga D, Zwart E, Witjes MJ, de Haan G, van Os R, Coppes RP. 2016. Human salivary gland stem cells functionally restore radiation damaged salivary glands. *Stem cells*. 34(3):640-652.
- Rebutini IT, Hoffman MP. 2009. Ecm and fgf-dependent assay of embryonic smg epithelial morphogenesis: Investigating growth factor/matrix regulation of gene expression during submandibular gland development. *Extracellular matrix protocols*. Springer. p. 319-330.
- Sakai T, Onodera T. 2008. Embryonic organ culture. *Current protocols in cell biology*. 41(1):19.18. 11-19.18. 18.
- Sapudom J, Ullm F, Martin S, Kalbitzer L, Naab J, Möller S, Schnabelrauch M, Anderegg U, Schmidt S, Pompe T. 2017. Molecular weight specific impact of soluble and immobilized hyaluronan on cd44 expressing melanoma cells in 3d collagen matrices. *Acta biomaterialia*. 50:259-270.
- Sathi GA, Farahat M, Hara ES, Taketa H, Nagatsuka H, Kuboki T, Matsumoto T. 2017. Mscf orchestrates branching morphogenesis in developing submandibular gland tissue. *Journal of Cell Science*. 130(9):1559-1569.

- Scott J, Dorling J. 1965. Differential staining of acid glycosaminoglycans (mucopolysaccharides) by alcian blue in salt solutions. *Histochemie*. 5(3):221-233.
- Scott J, Quintarelli G, Dellovo M. 1964. The chemical and histochemical properties of alcian blue. *Histochemie*. 4(2):73-85.
- Sequeira SJ, Soscia DA, Oztan B, Mosier AP, Jean-Gilles R, Gadre A, Cady NC, Yener B, Castracane J, Larsen M. 2012. The regulation of focal adhesion complex formation and salivary gland epithelial cell organization by nanofibrous plga scaffolds. *Biomaterials*. 33(11):3175-3186.
- Shin J, Choi EJ, Cho JH, Cho A-N, Jin Y, Yang K, Song C, Cho S-W. 2017. Three-dimensional electroconductive hyaluronic acid hydrogels incorporated with carbon nanotubes and polypyrrole by catechol-mediated dispersion enhance neurogenesis of human neural stem cells. *Biomacromolecules*. 18(10):3060-3072.
- Singley CT, Solursh M. 1981. The spatial distribution of hyaluronic acid and mesenchymal condensation in the embryonic chick wing. *Developmental biology*. 84(1):102-120.
- Solursh M, Morriss GM. 1977. Glycosaminoglycan synthesis in rat embryos during the formation of the primary mesenchyme and neural folds. *Developmental biology*. 57(1):75-86.
- Spicer AP, Tien JL, Joo A, Bowling RA. 2002. Investigation of hyaluronan function in the mouse through targeted mutagenesis. *Glycoconjugate journal*. 19(4-5):341-345.
- Srinivasan PP, Patel VN, Liu S, Harrington DA, Hoffman MP, Jia X, Witt RL, Farach-Carson MC, Pradhan-Bhatt S. 2017. Primary salivary human stem/progenitor cells undergo microenvironment-driven acinar-like differentiation in hyaluronate hydrogel culture. *Stem cells translational medicine*. 6(1):110-120.
- Taketa H, Sathi GA, Farahat M, Rahman KA, Sakai T, Hirano Y, Kuboki T, Torii Y, Matsumoto T. 2015. Peptide-modified substrate for modulating gland tissue growth and morphology in vitro. *Scientific reports*. 5:11468.
- Takeuchi J, Sobue M, Yoshida M, Uchibori N, Sato E, Miura K. 1981. A high level of glycosaminoglycan-synthesis of squamous cell carcinoma of the parotid gland. *Cancer*. 47(8):2030-2035.
- Talal N. 1987. Overview of sjögren's syndrome. *Journal of Dental Research*. 66(2_suppl):672-674.
- Tanaka J, Ogawa M, Hojo H, Kawashima Y, Mabuchi Y, Hata K, Nakamura S, Yasuhara R, Takamatsu K, Irié TJNc. 2018. Generation of orthotopically functional salivary gland from embryonic stem cells. *Nature communications*. 9(1):1-13.
- Toole BP. 2001. Hyaluronan in morphogenesis. *Seminars in cell & developmental biology*. 12(2):79-87.
- Toole BP, Zoltan-Jones A, Misra S, Ghatak SJcto. 2005. Hyaluronan: A critical component of epithelial-mesenchymal and epithelial-carcinoma transitions. *Cells tissues organs*. 179(1-2):66-72.
- Toyoshima K-e, Asakawa K, Ishibashi N, Toki H, Ogawa M, Hasegawa T, Irié T, Tachikawa T, Sato A, Takeda AJNc. 2012. Fully functional hair follicle

- regeneration through the rearrangement of stem cells and their niches. *Nature communications*. 3(1):1-12.
- Umeda Y, Miyazaki Y, Shiinoki H, Higashiyama S, Nakanishi Y, Hieda Y. 2001. Involvement of heparin-binding egf-like growth factor and its processing by metalloproteinases in early epithelial morphogenesis of the submandibular gland. *Developmental biology*. 237(1):202-211.
- Vissink A, Jansma J, Spijkervet F, Burlage F, Coppes R. 2003. Oral sequelae of head and neck radiotherapy. *Critical Reviews in Oral Biology Medicine*. 14(3):199-212.
- Warburton D, Bellusci S, De Langhe S, Del Moral P-M, Fleury V, Mailleux A, Tefft D, Unbekandt M, Wang K, Shi W. 2005. Molecular mechanisms of early lung specification and branching morphogenesis. *Pediatric research*. 57(7):26-37.
- Wei C, Larsen M, Hoffman MP, Yamada KM. 2007. Self-organization and branching morphogenesis of primary salivary epithelial cells. *Tissue engineering*. 13(4):721-735.
- Wolny PM, Banerji S, Gounou C, Brisson AR, Day AJ, Jackson DG, Richter RP. 2010. Analysis of cd44-hyaluronan interactions in an artificial membrane system insights into the distinct binding properties of high and low molecular weight hyaluronan. *Journal of Biological Chemistry*. 285(39):30170-30180.
- Wu F, Li J, Zhang K, He Z, Yang P, Zou D, Huang N. 2016. Multifunctional coating based on hyaluronic acid and dopamine conjugate for potential application on surface modification of cardiovascular implanted devices. *ACS Applied Materials & Interfaces*. 8(1):109-121.
- Xue P, Li Q, Li Y, Sun L, Zhang L, Xu Z, Kang Y. 2017. Surface modification of poly (dimethylsiloxane) with polydopamine and hyaluronic acid to enhance hemocompatibility for potential applications in medical implants or devices. *ACS Applied Materials & Interfaces*. 9(39):33632-33644.
- Yang C, Cao M, Liu H, He Y, Xu J, Du Y, Liu Y, Wang W, Cui L, Hu J. 2012a. The high and low molecular weight forms of hyaluronan have distinct effects on cd44 clustering. *Journal of Biological Chemistry*. 287(51):43094-43107.
- Yang T-L, Lin L, Hsiao Y-C, Lee H-W, Young T-H. 2012b. Chitosan biomaterials induce branching morphogenesis in a model of tissue-engineered glandular organs in serum-free conditions. *Tissue Engineering Part A*. 18(21-22):2220-2230.
- Yang T-L, Young T-H. 2008. The enhancement of submandibular gland branch formation on chitosan membranes. *Biomaterials*. 29(16):2501-2508.
- Yang T-L, Young T-H. 2009. The specificity of chitosan in promoting branching morphogenesis of progenitor salivary tissue. *Biochemical biophysical research communications*. 381(4):466-470.

국문초록

타액선 발생과정에서 히알루론산의 역할과 조직공학에서의 생체모방적 응용

이 상 우

서울대학교 대학원
치의과학과 신경생물학 전공
(지도교수: 박 경 표)

구강건조증은 타액선의 기능이상으로 인해 타액량이 감소함으로써 발생한다. 정상적인 타액분비는 구강건강을 유지하는 데 필수요소로서 저작 및 연하를 돕는 윤활작용, 구강 내 pH 유지, 치아의 재광화, 향균, 및 조직재생 기능을 수행하고 있다. 따라서 구강건조증이 발생하면 구강 건강과 전신 건강까지도 위협받게 된다. 타액선의 손상은 크게 노화, 쇼그렌 증후군과 같은 자가면역질환, 그리고 두경부암의 방사선치료시 발생하는 방사선으로 인한 손상으로 나누어 볼 수 있다. 현재로서는 외부에서 배양한 타액선 조직의 이식과 타액선의 자연 재생을 도모하는 법이 가장 효과적인 해결책으로 제시되고 있다. 이에 다양한 세포지지체들이 타액선 조직공학에 활용되었으나 이 중 어떤 재료도 타액선의 복잡한 구조와 다양한 세포들의 정확한 배치를 재현해 내지 못하였다. 그러나 타액선의 발생과정에서는 이러한 세포들의 조직화와 구조화가 자연스럽게 일어나기 때문에 타액선의 재생과 조직공학적 접근에는 타액선 발생과정의 특징 중 하나인 “분지형태형성 (Branching morphogenesis)”에 관여하는 생체물질들과

그들의 물리화학적 특성을 이해하고 공학적으로 모방하는 것이 중요하다. 특히 히알루론산은 타 장기들의 발생과정에서 그 역할이 잘 알려져 있으나 타액선 발생과정에서의 히알루론산의 역할은 아직 밝혀져 있지 않았다.

제 1 장에서는 배아 타액선의 체외 배양모델을 활용하여 타액선의 발생과정에서의 히알루론산의 분포와 역할, 그리고 이를 조직공학적으로 응용하는 연구내용을 논하고 있다. 먼저, 발생하는 타액선의 중간엽에는 다량의 히알루론산이 존재함을 확인하였고 이와 접하는 상피조직의 c-Kit+ 전구세포들이 히알루론산의 수용체인 CD44 를 발현함을 확인하였다. 히알루론산의 생산을 억제하거나 분해하면 타액선의 분지형태형성이 중단되었으며 c-Kit+ 전구세포의 양 또한 급격하게 감소하였다. 또한 히알루론산 생산 저해제나 분해효소 처리를 통해 중단된 분지형태형성이 고 분자량의 히알루론산을 배양액에 첨가할 시 일부 재개됨을 확인하였다. 저 분자량의 히알루론산은 회복효과가 없었기에 타액선의 발생과정에는 고 분자량의 히알루론산이 중요함을 알게 되었다. 배아 타액선을 세포 수준으로 분해하여 이를 다시 배양환경에 심어주면 분해된 세포들이 다시 모여 타액선 구조를 재구성하는데 이렇게 재구성되어 형성된 세포 덩어리를 “organ germ” 이라 지칭한다. Organ germ 을 손상된 타액선에 이식하여 타액선 기능을 온전히 회복시킨 연구사례들이 다수 출판되었지만 organ germ 을 체외에서 다량 배양하는 방법은 아직 미지수이다. 배아 타액선의 organ germ 형성과정에서 히알루론산의 역할을 실험한 결과 히알루론산의 생성이 억제되거나 분해효소에 의해 분해되면 organ germ 의 형성이 억제되고 organ germ 내의 c-Kit+ 전구세포의 양 또한 줄어들음을 확인하였다. 반대로 고 분자량의 히알루론산을 배양액에 첨가하면 organ germ 의 형성이 촉진되고 c-Kit+ 전구세포들의 양 또한 증가하였다. 마지막으로 히알루론산의 형태, 즉 자유롭게 용액 내에 부유하는 형태와 조직 내 존재하는 히알루론산과 같이 특정 표면에 고정된 형태의 히알루론산이 배아타액선 organ germ 에 미치는 영향을 알아보았다. 폴리도파민과 히알루론산을 배합한 용액 내에 배아타액선 배양에 쓰이는 폴리카보네이트

막을 담귀 히알루론산을 표면에 고정시켰다. 그 결과 같은 분자량의 히알루론산이라도 수용액 형태 보다 표면에 고정된 히알루론산이 배아타액선 organ germ 형성을 더욱 촉진시키는 것을 관찰하였다.

제 2 장에서는 챕터 1 에서 발견한 사실들에 바탕하여 히알루론산을 더욱 효과적으로 다양한 표면에 고정시킬 수 있도록 NiCHE (Nature-inspired Catechol-conjugated Hyaluronic acid Environment) 라고 명명한 히알루론산 코팅 플랫폼을 개발하였다. 홍합접착단백질의 접착성분인 카테콜기를 히알루론산에 화학적으로 결합시켜 접착성이 있는 히알루론산-카테콜 을 만들었다. 배아타액선은 주변 환경의 물리적인 특성에 민감하기 때문에 딱딱한 표면에서는 제대로 자라지 못한다. 부드러운 표면이나 하이드로겔에서는 정상적으로 분지형태형성이 진행되지만 이러한 재료들은 강도가 약하기 때문에 생체 내에서 내구성이 떨어져 임상적인 적용이 어렵다. 따라서 나는 내구성과 생체적합성 두 가지 모두를 만족하는 재료를 찾기 보다는 기존에 존재하는 내구성이 좋은 생체재료들에 히알루론산-카테콜을 사용하여 표면을 코팅해 보았다. 폴리카보네이트, 고강도 알지네이트 하이드로겔, 그리고 폴리카프로락톤에 히알루론산을 충분히 두껍게 고정하는 데 성공하였고 히알루론산이 코팅된 표면에서는 재료의 물성과 상관없이 배아타액선의 분지형태형성이 성공적으로 진행되었다. 이러한 강화 효과는 표면 위에 고정된 히알루론산들이 배아타액선 내 혈관내피세포의 증식을 돕기 때문이었다. 히알루론산이 코팅된 표면 위에서 CD44 를 발현하는 혈관내피세포들의 ERK 의 인산화가 증가되었으며 혈관신생 또한 증가되었다. VEGF 억제제를 처리하자 히알루론산 코팅에 의한 강화효과가 사라짐을 관찰하였다.

이상의 연구결과는 타액선의 발생과정에서 히알루론산의 역할이 중요함을 밝히고 있으며 이를 조직공학적으로 응용한다면 타액선에 최적화된 히알루론산 기반의 조직재생 플랫폼을 개발할 수 있을 것으로 기대된다.

주요어: 히알루론산, 타액선, 재생, 발생, 폴리도파민, 분지형태형성,
카데콜, 조직공학

학번: 2011-22467